VILNIUS UNIVERSITY

Darius Stučinskas

Thermal lens diagnostics and mitigation in diode end pumped lasers

Doctoral dissertation

Physical sciences, Physics (02 P)

Vilnius, 2010

This research was performed in 2005-2009 at Vilnius University

Scientific supervisor:

Dr. Arūnas Varanavičius (*Vilnius University*, Physical sciences, Physics – 02P)

VILNIAUS UNIVERSITETAS

Darius Stučinskas

Šiluminio lęšio charakterizavimas bei jo įtakos mažinimas išilginio diodinio kaupinimo lazeriuose

Daktaro disertacijos santrauka

Fizikiniai mokslai, fizika (02 P)

Vilnius, 2010

Disertacija rengta 2005-2009 metais Vilniaus universitete

Mokslinis vadovas:

Dr. Arūnas Varanavičius (*Vilniaus universitetas*, fiziniai mokslai, fizika – 02P)

Contents

List of the Abbreviations

AE – active element

AR – anti-reflective

BBO - beta barium borate

CCD – charge coupled device

CW – continuous wave

DH – digital holography

DPSSL – diode pumped solid state laser

fs – femtosecond (10^{-15}s)

FWHM – full width at half maximum

GdCOB – gadolinium calcium oxyborate

He-Ne – helium-neon

HR – high reflective

KGW - potassium gadolinium tungstate

KYW - potassium yttrium tungstate

MEMS – micro electro-mechanical systems

Nd - neodymium

Nd:YAG – neodymium doped yttrium aluminum garnet

Nd:YVO$_4$ - neodymium doped yttrium orthovanadate

ns – nanosecond (10^{-9}s)

ps – picoseconds (10^{-12}s)

RMS - root mean square

TEM - Transverse Electromagnetic Mode

Yb - ytterbium

Yb:KGW – ytterbium doped potassium gadolinium tungstate

Yb:YAG – ytterbium doped yttrium aluminum garnet

YCOB – yttrium calcium oxyborate

YSO – yttrium orthosilicate

Introduction

Like any machine, lasers operate with efficiencies ultimately limited by basic thermodynamics. As a result, a significant fraction of the power injected into any laser cannot be usefully extracted and normally ends up as heat in the lasing medium. Laser brightness, coherence, polarization, and stability all suffer from the resulting thermooptic distortions. Over the last four decades, many strategies have been developed for coping with this fundamental problem. Nevertheless, the performance of most laser systems is still limited by detrimental heat generation.

With availability of high brightness diode lasers, diode-pumped solid-state laser (DPSSL) technology has become a very intense field of research in Physics. The replacement of flash-lamp pumping by direct laser-diode pumping for solid-state materials has brought a very important breakthrough in the laser technology in particular for high-power lasers [1; 2]. In fact, the better matching between absorption wavelength and material's absorption spectra brought by the use of laser diode emission—compared to the broad one of flash-lamps—has lead to a significant benefit in efficiency and subsequently in simplicity, compactness, reliability and cost [2]. This progress has substantial implications on laser applications such as fundamental and applied research, laser processing and other applications.

Diffraction limited output has been demonstrated in high average power fiber lasers [3]. However, this technology has limited applications in high peak power lasers due to limited aperture of amplifying media that is a reason for optical damage problems and appearance of nonlinear effects at relatively low laser energies [4]. One of the most significant steps in achieving high average powers was the development of thin disk laser [5]. Thin disc lasers are well suited for extremely high output powers: around 500 W of output power in a diffraction-limited continuous-wave beam have been obtained with a single disk or around 1 kW using two disks [6]. So far, thin-disk lasers have lead to the highest average output power of 80 W from a mode-locked laser [7; 8], and pulse energies of > 20 μJ combined with sub-picosecond pulse durations are possible [9]. However, such designs tend to be quite complex due to multiple passes through short active element limiting in this way the use of such lasers in industrial applications.

End-pumped schemes offer more reliable and less expensive laser designs yielding an optical to optical efficiency of more than 40% [10; 11]. Such configuration is particularly favorable at relatively low powers as it can provide a high degree of spatial overlap between pump and lasing modes. This gives the potential to realize lasers that have both a high efficiency and a high beam quality. The main problem hindering brightness scaling of diode-pumped solid-state lasers is heat generation within the laser medium, which leads to a spatial variation in temperature, and consequently internal stresses within the laser material and, in addition, deformation of the laser rod end faces due to differential expansion [12]. The net result is beam distortion due to thermal lensing, depolarization loss due to stress induced birefringence and ultimately catastrophic failure due fracture of the laser rod, if the thermally induced stress exceeds the tensile strength of the laser material.

Many different approaches on thermal effects mitigation have been developed up to date: a) based on phase conjugation [13; 14], b) employing materials with negative dn/dT [15], c) adaptive mirrors [15], d) thermally driven mirrors [16; 17], e) static compensators [18]. However, none of the mentioned methods is considered as “standard” approach for thermal effect mitigation. Thermal effects have to be treated individually during design of every high average power and/or high output beam quality laser system.

Although the effects of heat dissipation in laser materials can be calculated [19; 20; 21; 22] for a particular geometry with appropriate boundary conditions, material inhomogeneities, as well as non-uniform optical pumping, are difficult to account for by numerical modeling alone. As example, for crystals like KGW or KYW [23], which are of particular interest for Ytterbium doping, we need to know no less than 36 coefficients before to be able to draw the new refractive index ellipsoid at a given point of the crystal. Unfortunately these parameters are not known, which means that a rigorous calculation even with a finite element analysis code is just not possible. Therefore, accurate characterization of thermal lensing for each rod or slab of laser material installed in a particular laser cavity to date can be achieved only by careful measurement of the transmitted wavefront.

Thermal lens has been measured for laser materials such as Nd:YAG in many different laser configurations [24; 25; 26; 27], however, for materials of particular interest for applications in diode pumped femtosecond lasers such as Yb:KGW or Yb:KYW only few works have been reported in last two decades [28; 29]. Other works related to thermal lensing in Yb:KGW are based on indirect estimation of thermal lensing [11; 30].

The **goal** of the dissertation is a development of high precision experimental set-up for thermal lens measurement and exploration of different approaches for thermal effects mitigation in diode end pump lasers. Our main attention was paid on methods suitable for application in industrial laser systems: simplicity, compactness and reliability of long term operation.

In order to accomplish this goal, fallowing **tasks** were performed:

- Construction of Shack Hartmann wavefront sensor, and its adaption to measurement of thermal lens in end pumped lasers.
- Experimental study of thermal lens mitigation by means of static aberration corrector inside laser cavity.

- Investigation of laser employing elliptical cavity mode geometry performance.
- Study of thermal lens in lasers based on Yb:KGW active elements of different crystallographic orientation.
- Exploring possibilities for laser power scaling by using symmetric resonator with two active elements.

The **innovations** presented in this thesis are:

- Thermal lens aberration compensator manufactured using thin film deposition technology was reported for the first time. We have shown that such thermal lens compensator design improves laser output spatial characteristics in wide pump power range.
- We have reported thermal lens measurements results in Yb:YAG with elliptical mode geometry for the first time.
- Thermal lens measurement results in Yb:KGW crystals for pump powers above 10 W and up to 100W were reported for the first time. Thermal lens measurement results in $\angle z{:}N_g=44^{o}$ athermal orientation Yb:KGW active element and end bulging contribution to total thermal lens for N_g orientation Yb:KGW active element was reported for the first time.
- We have reported on operation of two slab shaped active element laser based on Yb:KGW that provides highest output power reported up to date.

The **statements to defend** in this thesis are**:**

1. Employment of static thermal lens aberration corrector manufactured using thin film deposition technology allows reduction of laser threshold up to 70% and ensures output beam quality parameter M^2 improvement up to 25% in wide pump power range.

2. Use of elliptical cavity mode geometry in ultrashort pulse lasers allows for several times scaling of the output pulse energy at the same time ensuring spatial beam quality close to diffraction limit.
3. Despite higher thermal lens focusing power, compared to athermal cut crystals, N_g orientation Yb:KGW active element possesses most attractive set of thermal and optical properties for development of ultrafast lasers with good spatial output characteristics at high average powers.
4. Output power of diode end pumped Yb:KGW laser can be nearly doubled by implementation of symmetric laser cavity with two active elements. Highest reported output power for Yb:KGW laser reaching 44W and maintaining high beam quality has been achieved using this approach.

This thesis is arranged in the fallowing way. The first chapter provides an introduction to thermal effects in laser active elements and brief overview of thermal lens measurement techniques. In chapter 2 experimental Shack Hartmann wavefront sensor setup is presented. Results on compensation of thermal lens aberrations of high average power $Nd:YVO_4$ laser by the use of aspherically shaped optical element are presented in chapter 3. The highly reflecting optical element was shaped basing on measurements of actual thermal lens aberrations in active element, and manufactured using thin film deposition technology. In chapter 4 diode end-pumped Yb:YAG laser with elliptical cavity mode configuration is investigated. Results on numerical modeling of laser cavity based on measurements of astigmatic thermal lens in active element and on laser performance in free running and Q- switched mode are presented. In chapter 5 thermal lensing and thermal beam distortions in high-power laser diode end-pumped Yb:KGW crystals cut for beam propagation along the N_g axis and along the athermal direction in the N_p- N_g plane are compared. As well, end bulging of N_g cut active element measurement results are presented. Method for average power scaling by implementation of symmetric laser cavity with two active elements is investigated in chapter 6.

Contributions:

The author of this thesis conducted the practical part of the study. His contributions and responsibilities consist of:

- development of Shack – Hartmann wavefront sensor and data processing software for small dimension thermal lens characterization;
- carrying-out of thermal lens and laser performance measurements;
- visualization, interpretation and publication of the experimental results.

The main coauthors of the work described in this thesis were Dr. *A. Varanavičius*, *R. Antipenkov*, *M. Grishin*, *J.Kodz* , *A. Melninkaitis* and *A. Vanagas*.

Dr. *Arūnas Varanavičius* is laboratory head, responsible for financial funding of most of equipment needed for research. He also participated in formulation of general tasks as well as in interpretation and presentation of obtained results.

Romanas Antipenkov helped with most of experiments and result interpretation. As well, he should be credited for assistance with graphic user interface of Shack Hartmann wavefront sensor and software used for wavefront interpretation. He has also performed experiments in q-switched and femtosecond amplification regimes described in [A1].

Mikhail Grishin has supplied most of equipment used in [A4, C7]. He should be also credited for valuable discussions and ideas related with thermal lensing in diode pumped solid state lasers.

Jaroslav Kodz assisted during initial measurements related to [A4, C7].

Andrius Melninkaitis and *Andrius Vanagas* have performed DH measurements of compensator samples presented in [A4, C7].

The List of Author's Publications

Author has published 4 papers in total [A1-A4]. He also made 7 reports [C1-C7] at the conferences.

Publications:

[A1] D. Stučinskas, R. Antipenkov, and A. Varanavičius "30 W dual active element Yb:KGW regenerative amplifier for amplification of sub - 500fs pulses", Proc. SPIE **6731**, 67312Y (2007).

[A2] R. Antipenkov, D. Stučinskas, and A. Varanavičius "~5 W output power Q-switched Yb:YAG laser with elliptical mode geometry", Proc. SPIE **6731**, 67312Z (2007).

[A3] R. Antipenkov, D. Stučinskas, and A. Varanavičius "CW and Q-switched performance of end-pumped Yb:YAG laser with elliptical mode geometry", Lithuanian Journal of Physics, Vol. **49**, No. 2, pp. 163-170 (2009).

[A4] D. Stučinskas, R. Antipenkov, A. Varanavičius M. Grishin, J.Kodz , A. Melninkaitis and A. Vanagas "Thermal lens compensation in high average power diode pumped Nd:YVO_4 laser using aspheric optical element", Lithuanian Journal of Physics, Vol. **49**, No. 4, pp. 433-438 (2009).

Publications in review:

[B1] D. Stučinskas, R. Antipenkov, A. Varanavičius "Thermal lensing in high-power diode-pumped Yb:KGW laser", Lithuanian Journal of Physics

Conference presentations:

[C1] R. Antipenkov, D. Stučinskas, A. Varanavičius, “5 W Output Power Q-Switched Yb:YAG. Laser With Elliptical Mode Geometry”, ICONO/LAT 2007 conference, Minsk, (2007).

[C2] D. Stučinskas , R. Antipenkov, and A. Varanavičius “30 W dual active element Yb:KGW regenerative amplifier for amplification of sub - 500fs pulses”, ICONO/LAT 2007 conference, Minsk, (2007).

[C3] R. Antipenkov, D. Stučinskas, L. Giniūnas, S. Jasinavičius, “Termolęšis ir jo aberacijos išilginio diodinio kaupinimo Nd:YVO_4 Lazeryje”, LNFK 36, Vilnius, (2005).

[C4] D. Stučinskas, R. Antipenkov, A. Varanavičius, “Didelės vidutinės galios Yb:KGW regeneratyvinis stiprintuvas femtosekundinių impulsų stiprinimui”, LNFK 37, Vilnius, (2007).

[C5] R. Antipenkov, D. Stučinskas, A. Varanavičius, “Išilginio diodinio kaupinamo elipsinės modos Yb:YAG lazeris”, LNFK 37, Vilnius, (2007).

[C6] D. Stučinskas, R. Antipenkov, A. Varanavičius, “Termolęšio tyrimas diodinio kaupinimo Yb:KGW lazeriuose su skirtingos optinės orientacijos aktyviaisiais elementais”, LNFK 38, Vilnius, (2009).

[C7] D. Stučinskas, A. Varanavičius, M. Grishin, J.Kodz , A. Melninkaitis, A. Vanagas, “Termolęšio kompensavimas diodinio kaupinimo didelės vidutinės galios Nd:YVO4 lazeryje”, LNFK 38, Vilnius, (2009).

1 Thermal lens in end pumped lasers and its measurement methods

The optical pumping process in a solid-state laser material is associated with the generation of heat for a number of reasons.

a) The energy difference of the photons between the pump band and the upper laser level is lost as heat to the host lattice and causes the so-called quantum defect heating;

b) the energy difference between the lower laser level and the ground state is thermalized;

c) since the quantum efficiency of the fluorescence processes involved in the laser transition is less than unity, heating due to quenching mechanisms takes place.

Efficient heat removal and the reduction of the thermal effects which are caused by the temperature gradients across the active area of the laser medium usually dominate design considerations for high-average-power systems.

1.1 Temperature distribution

The first study of thermal effects in crystals has been provided by Koehner [31; 12] in the early 1970s. He considered flash-pumped Nd:YAG rods, with fallowing assumptions: internal heat generation and cooling along the cylindrical surface of an infinitely long rod is uniform, the heat flow is strictly radial, and end effects and the small variation of coolant temperature in the axial direction can be neglected. The radial temperature distribution in a cylindrical rod with the thermal conductivity *K*, in which heat is uniformly generated at a rate *Q* per unit volume, is obtained from the one-dimensional heat conduction equation (1.1)

$$\frac{d^2T}{dr^2}+\left(\frac{1}{r}\right)\left(\frac{dT}{dr}\right)+\frac{Q}{K}=0 \tag{1.1}$$

The solution of this differential equation gives the steady-state temperature at any point along a radius of length r. With the boundary condition *T*(r_o) for *r* = r_o where *T*(r_o) is the temperature at the rod surface and r_o is the radius of the rod, it follows that

$$T(r)=T(r_0)+\left(\frac{Q}{4K}\right)(r_0{}^2-r^2) \tag{1.2}$$

The temperature profile is parabolic, with the highest temperature at the center of the rod. The temperature gradients inside the rod are not a function of the surface temperature *T*(r_o) of the rod. The heat generated per unit volume can be expressed as

$$Q=\frac{P_a}{\pi r_0^2 L} \tag{1.3}$$

where P_a is the total heat dissipated by the rod, and L is the length of the rod. The temperature difference between the rod surface and the center is

$$T(0)-T(r_o)=\frac{P_a}{4\pi KL}. \tag{1.4}$$

The transfer of heat between the rod and the flowing liquid creates a temperature difference between the rod surface and the coolant. A steady state will be reached when the internal dissipation P_a is equal to the heat removed from the surface by the coolant

$$P_a=2\pi r_0 Lh(T(r_o)-T_F) \tag{1.5}$$

where h is the surface heat transfer coefficient, and T_F is the coolant temperature. With F = $2\pi r_o L$ being the surface area of the rod, it follows that

$$T(r_0) - T_F = \frac{P_a}{Fh} \tag{1.6}$$

Combining (1.4 and 1.6), one obtains for the temperature at the center of the rod

$$T(0) = T_F + P_a\left(\frac{1}{4\pi KL} + \frac{1}{Fh}\right). \tag{1.7}$$

Thus, from the geometry, and the appropriate system and material parameters, the thermal profile of the crystal can be determined, except that h must be evaluated.

1.2 Thermal Stresses

The temperature gradients generate mechanical stresses in the laser rod, since the hotter inside area is constrained from expansion by the cooler outer zone. The stresses in a cylindrical rod, caused by a temperature distribution $T(r)$, can be calculated from the equations given by Timoshenko and Goodier [32]. Equations (1.8-10) describe the radial σ_r, tangential σ_ϕ, and axial σ_z stress in an isotropic rod with free ends and a temperature distribution according to (1.2)

$$\sigma_r(r) = QS(r^2 - r_0^2), \quad 1.8$$

$$\sigma_\phi(r) = QS(3r^2 - r_0^2), \quad 1.9$$

$$\sigma_z(r) = 2QS(2r^2 - r_0^2), \quad 1.10$$

where the factor $S = \alpha E[16K(1-v)]^{-1}$ contains the material parameters; E is Young's modulus, v is Poisson's ratio, and α is the thermal coefficient of expansion. The stress components, σ_r, σ_ϕ, σ_z represent compression of the material when they are negative and tension when they are positive. We notice that the stress distributions also have a parabolic dependence on *r*. The center of the rod is under compression. The radial component of the stress goes to zero at the rod surface, but the tangential and axial components are in tension on the rod surface by virtue of the larger bulk expansion in the rod's center compared to the circumference.

1.3 Photoelastic Effects

The stresses generate thermal strains in the rod, which, in turn, produce refractive index variations via the photo-elastic effect. The refractive index of a medium is specified by the indicatrix, which in its most general case is an ellipsoid. A change of refractive index due to strain is given by a small change in shape, size, and orientation of the indicatrix [33]. The change is specified by small changes in the coefficients B_{ij} ,

$$B_{ij} = P_{ijkl}\varepsilon_{kl} \quad \text{(i, j, k, l = 1, 2, 3)} \tag{1.12}$$

where P_{ijkl} is a fourth-rank tensor giving the photo-elastic effect. The elements of this tensor are the elasto-optical coefficients. ε_{kl} is a second-rank strain tensor.

The complete computation of thermal effects in a given material requires that we know everything about the tensors. The minimum number of independent terms of each tensor depends on the crystal symmetry, as discussed by [34]. For instance, let us consider crystals like KGW or KYW [23], GdCOB [35], YCOB [36] or YSO [37] which are of particular interest for Ytterbium doping. These crystals belong to the monoclinic crystal system: this means that the compliances can be ‘‘reduced’’ to 13 independent parameters, and the elasto-optical tensor, once the redundant coefficients have been identified, appears to have 20 independent coefficients [34]. Adding the 3 thermal expansion coefficients, this means that we need to know no less than 36 coefficients before to be able to draw the new index ellipsoid at a given point of the crystal. Obviously these parameters are not known, which means that a rigorous calculation even with a finite element analysis code is just not possible. This simple remark highlights the importance of experimental measurements of thermal effects in such crystals, and shows the interest as well as the inherent limitations of a simple analytical model.

We will confine our calculation to the case of a Nd.YAG laser rod. Since Nd: YAG is a cubic crystal, the indicatrix is a sphere. Under stress the indicatrix becomes an ellipsoid. Nd: YAG rods are grown with the cylindrical axes along the [111] direction. The light propagates in this direction, and thus the change of the refractive index along the [111] is of interest.

Since the transverse stresses are in the radial and tangential directions - relative to the coordinate system shown in - the local indicatrix also orients its axis in these directions. In a cylindrical coordinate system the photo-elastic changes in the refractive index for the *r* and ϕ polarizations are given by [38]

$$\Delta n_r = -\frac{1}{2} n_0^3 \Delta B_r \tag{1.13}$$

and

$$\Delta n_\phi = -\frac{1}{2} n_0^3 \Delta B_\phi . \tag{1.14}$$

Introducing the expression for ΔB_r and ΔB_ϕ, into (1.13-14), the refractive-index changes are given by [39; 40]

$$\Delta n_r = -\frac{1}{2} n_{0r}^3 \frac{\alpha Q}{K} C_r r^2 , \tag{1.15}$$

$$\Delta n_\phi = -\frac{1}{2} n_{0r}^3 \frac{\alpha Q}{K} C_\phi r^2 , \tag{1.16}$$

where C_r a C_ϕ are functions of the elasto-optical coefficients of Nd : YAG.

$$C_r = \frac{(17\nu - 7)P_{11} + (31\nu - 17)P_{12} + 8(\nu + 1)P_{44}}{48(\nu - 1)},$$

$$C_\phi = \frac{(10\nu - 6)P_{11} + 2(11\nu - 5)P_{12}}{32(\nu - 1)}.$$

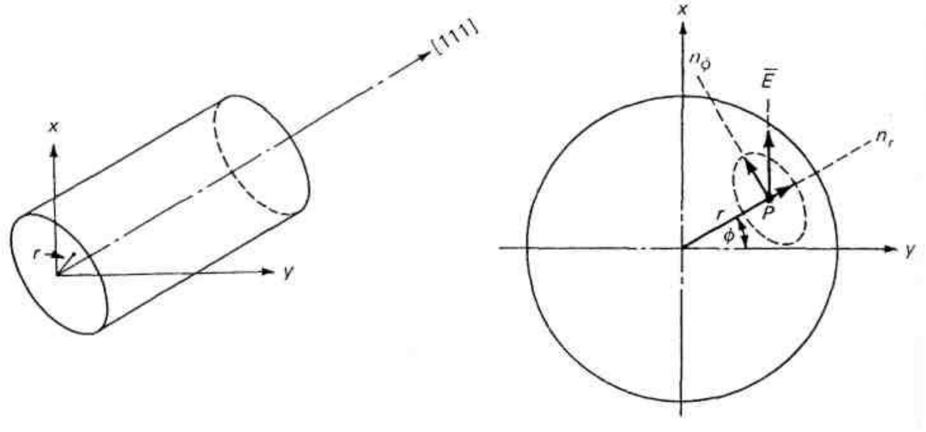

Fig. 1.1. ***Crystal orientation for a Nd:YAG rod (left) and orientation of indicatrix of the thermally stressed Nd:YAG rod in a plane perpendicular to the rod axis (right)*** **[12].**

The induced birefringence is determined from (1.15-16)

$$\Delta n_r - \Delta n_\phi = n_{0\,r}^{3} \frac{\alpha Q}{K} C_B r^2 \tag{1.17}$$

where

$$C_B = \frac{1+\nu}{48(1-\nu)}(P_{11} - P_{12} + 4P_{44}).$$

Inserting the values of the photo-elastic coefficients and the material parameters of Nd:YAG, α=7.5xW^{-6}/°C, *K*=0.14 W/cm°C, *ν* = 0.25, *n*$_0$=1.82, into (1.15-17), one obtains C_r = 0.017, C_φ = -0.0025, C_B = -0.0099, and

$$\Delta n_r = (-2.8\times 10^{-6})Qr^2,$$

$$\Delta n_{\phi} = (0.4\times10^{-6})Qr^{2},$$

$$\Delta n_{r} - \Delta n_{\phi} = (-3.2\times10^{-6})Qr^{2}.$$

where *Q* has the dimension of watts per cubic centimeter and *r* is measured in centimeters [12].

1.4 Thermal Lensing

The change of the refractive index can be separated into a temperature and a stress dependent variation. Hence

$$n(r) = n_0 + \Delta n(r)_T + \Delta n(r)_{\varepsilon}, \tag{1.18}$$

where n(r) is the radial variation of the refractive index; n_0 is the refractive index at the center of the rod; and $\Delta n(r)_T$, $\Delta n(r)_{\varepsilon}$ are the temperature and stress dependent changes of the refractive index, respectively.

The temperature dependent change of refractive index can be expressed as

$$\Delta n(r)_T = (T(r) - T(0))\left(\frac{dn}{dT}\right). \tag{1.19}$$

From (1.2-4) we obtain

$$\Delta n(r)_T = -\frac{Q}{4K}\frac{dn}{dT}r^2. \tag{1.20}$$

As can be seen from (1.15, 1.16 and 1.20), the refractive index in a laser rod shows a quadratic variation with radius *r*. An optical beam propagating along the rod axis suffers a quadratic spatial phase variation. This perturbation is equivalent to the effect of a spherical lens. The focal length of a lens-like medium where the refractive index is assumed to vary according to

$$n(r) = n_0\left(1 - \frac{2r^2}{b^2}\right) \tag{1.21}$$

Is given by [7.12]

$$f \cong n0 \frac{b^2}{4n_0 L}. \tag{1.22}$$

This expression is an approximation where it was assumed that the focal length is very long in comparison to the rod length. The distance is measured from the end of the rod to the focal point.

The total variation of the refractive index is obtained by introducing (1.15, 1.16, and 1.20) into (1.18):

$$n(r) = n_0 \left[1 - \frac{Q}{2K} \left(\frac{1}{2n_0} \frac{dn}{dT} + n_0^2 \alpha C_{r,\phi} \right) r^2 \right]. \tag{1.23}$$

As was discussed in the previously, the change of refractive index due to thermal strain is dependent on the polarization of light, therefore the photo-elastic coefficient $C_{r,\phi}$ has two values, one for the radial and one for the tangential component of the polarized light. Comparing (1.23) with (1.21) yields

$$f' = \frac{K}{QL} \left(\frac{1}{2} \frac{dn}{dT} + \alpha C_{r,\phi} n_0^3 \right)^{-1}. \tag{1. 24}$$

In final expression for the focal length of a Nd: YAG rod, contributions caused by end effects will be included. Perturbations of the principal thermal distortion pattern occur in laser rods near the ends, where the free surface alters the stress character. The so-called end effects account for the physical distortion of the flatness of the rod ends. Self-equilibrating stresses causing a distortion of flatness were found to occur within a region of approximately one diameter from the ends of Nd:glass and one radius from the end for Nd:YAG [27]. The deviation from flatness of the rod ends is obtained from

$$l(r)=\alpha_0 l_0 (T(r)-T(0)), \tag{1.25}$$

where l_0 is the length of the end section of the rod over which expansion occurs. With $l_0 = r_0$ and (1.2), we obtain

$$l(r) = -\alpha_0 r_0 \frac{Qr^2}{4K}. \tag{1.26}$$

The focal length of the rod caused by an end-face curvature is obtained from the thick-lens formula of geometric optics

$$f'' = \frac{R}{2(n_0 - 1)}, \tag{1.27}$$

where the radius of the end face curvature is $R=-(d^2l/dr^2)^{-1}$. From these expressions follows the focal length of the rod caused by a physical distortion of the flat ends:

$$f'' = K(\alpha Q r_0 (n_0 - 1))^{-1}. \tag{1.28}$$

The combined effects of the temperature and stress dependent variation of the refractive index and the distortion of the end face curvature of the rod lead to the following expression for the focal length:

$$f = \frac{KA}{P_a}\left(\frac{1}{2}\frac{dn}{dT} + \alpha C_{r,\phi} n_0^3 + \frac{\alpha r_0 (n_0 - 1)}{L}\right)^{-1}, \tag{1.29}$$

where A is the rod cross-sectional area, and P_a is the total heat dissipated in the rod. By introducing the appropriate materials parameters for Nd:YAG into (1.29), we can find that the temperature dependent variation of the refractive index constitutes the major contribution of the thermal lensing. The stress dependent variation of the refractive index modifies the focal length about 20%. The effect of end-face curvature caused by an elongation of the rod is less than 6 % [12].

Ignoring the end effects, we notice that the focal length is proportional to a material constant and the cross section *A* of the rod and is inversely proportional to the power P_a dissipated as heat in the rod.

1.5 End-Pumped Configurations

So far, we have discussed cylindrical rods which are pumped from the side. As we have seen, analytical solutions generally assume uniform heating in an infinitely long rod. End effects are treated separately as a distortion of the two-dimensional temperature distribution. With the availability of high-power diode lasers, end-pumping, or longitudinal-pumping, of laser crystals has become a very important technology. The thermal profile in an end-pumped laser is quite different from the systems discussed so far, due to very localized heat deposition. This leads to highly non-uniform and complex temperature and stress profiles. This is illustrated in Fig. 1.2 which shows the calculated temperature distribution in an end-pumped laser rod [41].

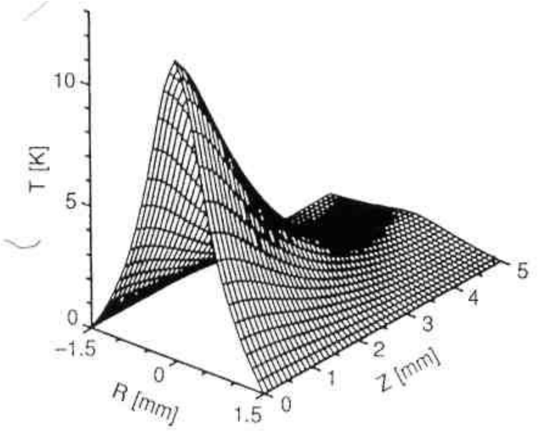

Fig. 1.2 Temperature distribution in an end-pumped laser rod [41]

An end-pumped laser rod has a temperature profile across the pumped region which is a function of the distribution of pump radiation. From the edge of the pumped region, the temperature decays logarithmically to the cooled cylindrical surface of the rod. Along the axis of the rod, the temperature profile will decay exponentially due to the exponential absorption of pump radiation. The fraction of pump power which is converted to heat inside the laser material acts as heat source. Different cooling arrangements and rod shapes lead to different boundary conditions. The major distinctions are convective or conductive cooling at the rod surface; and face-cooled thin disks or edge-cooled cylinders or slabs.

In order to maximize gain, and to match the TEM_{00} resonator mode, the pump beam is tightly focused, which leads to high-pump-power irradiance incident on the end of the laser rod. As a result, the input face is under a high thermal load. The thermal stress, which leads to strong thermal lensing, is often high enough to cause fracture of the end face of the laser rod.

The thermal management of end-pumped lasers can be greatly improved by the use of composite rods. Laser crystals, such as Nd: YAG, Nd: YVO_4 and Yb: YAG, have become available with sections of undoped host material on one or both ends. These end caps are diffusion bonded to the doped laser crystal. Composite rods are proven to provide a very effective way to reduce temperature and stresses at the face of end pumped lasers. Because the undoped region is transparent to the impinging pump radiation, there is no thermal load generated at the rod pump face [12].

The diffusion bond provides uninhibited heat flow from the doped to the undoped region. A large temperature reduction of about 35% is achieved for the composite rod, where a significant part of heat flow occurs into the undoped end cap. The undoped end cap prevents the doped pump face from expanding along its axis, therefore no surface deformation takes place at this interface.

1.6 The aberrations of the thermal lens

In conclusion to this chapter, we will introduce the thermal lens higher-order distortions id est the thermal lens aberrations. For a perfectly parabolic distortion of the wave front or equivalently a pure thermal lens, the thermal distortion can be easily compensated by addition in the laser cavity of the opposite divergent lens or by adjusting the distance of the different cavity elements. But, if aberrations are present the compensation is very difficult and requires complex systems [42]. While uncorrected, these aberrations lead to degradation in beam quality (brightness), and also to losses due to diffraction of the beam high spatial frequencies [43]. The aberrations are present when the wave front distortions induced by the absorbed pump beam are not perfectly parabolic. This occurs when the longitudinal pump beam has not a true top-hat profile, for example, in the case of a Gaussian pump beam profile [44]. Moreover, if the laser beam size is larger than the pumped area, the aberrations also become important. In general the aberrations affect the laser modes of the cavity in a way that to degrade the beam quality. This degradation can be evaluated by the M^2 factor or the Strelh ratio for example [45; 46].

As a conclusion for this section, we present a schematic diagram (Fig. 1.3) summing up the different thermal effects arising in a solid-state laser medium, and how they are related to each other.

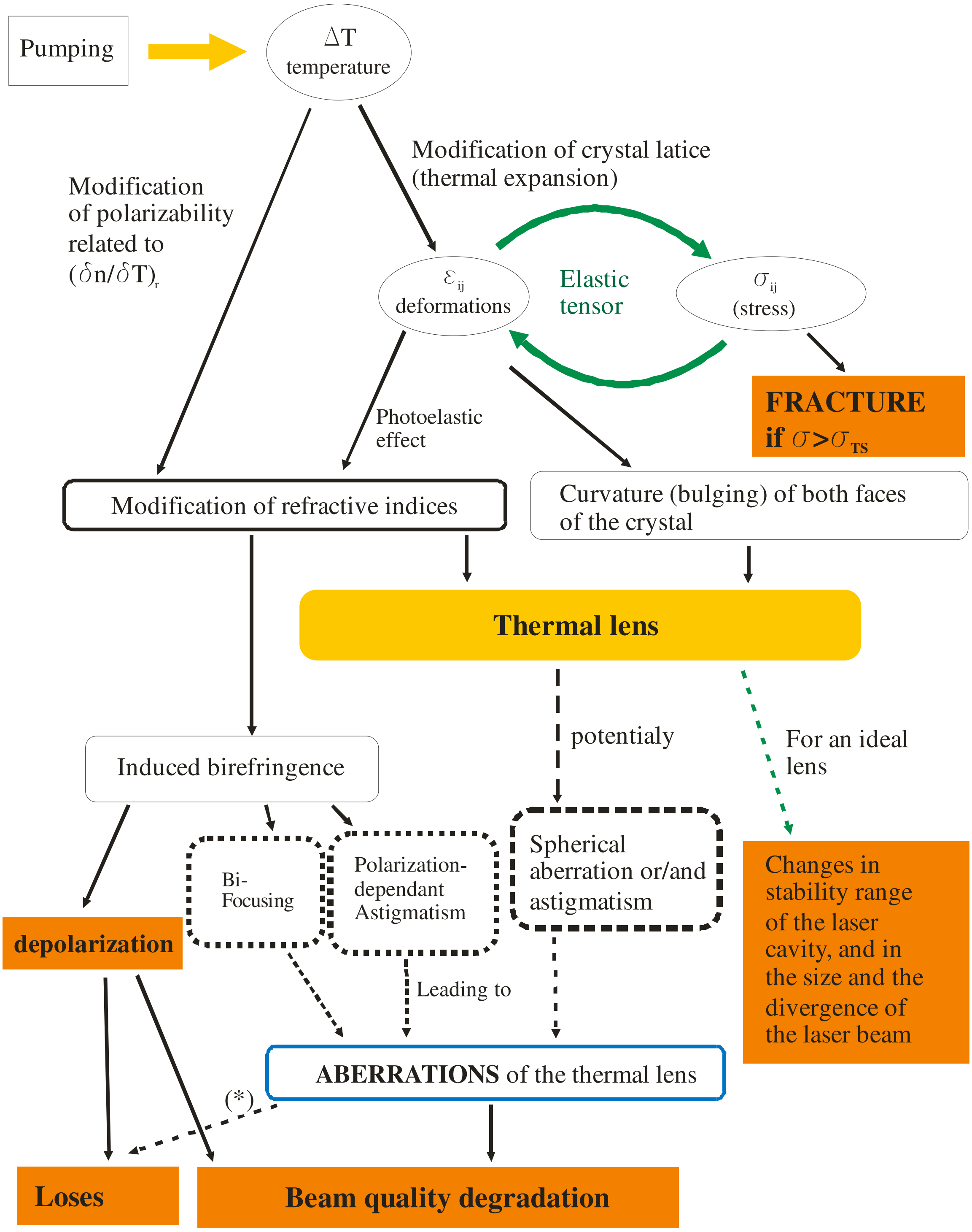

Fig. 1.3. Summary of the thermal effects in solid-state lasers. The observable consequences observable are presented in full rectangles. The aberrations can be split in two classes: the ones that do not depend on the polarization (lined rectangles) and the ones that depend on polarization (dotted rectangles) which come from the strain-induced birefringence. (*): 2 types of losses are induced by aberrations: the diffraction losses (associated with degradation in beam quality) and the losses induced by the eventual

presence of a diaphragm in the cavity to prevent from oscillation of higher order laser modes. Adapted from [47]

1.7 Thermal lens measurement techniques

The first evidence of thermal effects in lasers were demonstrated in 1965 by Gordon et al. [48], working at Bell Labs on He–Ne lasers for Raman spectroscopy applications. The use of liquids to Q-switch the laser lead to the observation of unexpected effects such as relaxation oscillation of jump of modes. The exceptionally long time constant of this phenomenon (several seconds) lead to the conclusion that a thermal lens was at the origin of the observed effects. This lens was created by the small absorption occurring in the liquids. The first application proposed by the authors was then to use it to measure very small absorption coefficients down to 10^{-4} cm^{-1}. As a matter of fact, the so-called ''thermal lens method'' allows nowadays to measure absorption coefficient lower than 10^{-7} cm^{-1} [49].

1.7.1 Geometrical methods

These methods are probably the simplest methods to measure the thermal lenses [47]. They can be separated in two sub-groups: one can exploit either the defocusing or the deflection of a beam passing through the pumped medium. The principle of the first category of methods is very simple. Considering a probe beam going through the crystal, the measurement of the axial shift of the focal point position allows to retrieve directly the thermal lens using simple geometrical optics. When the rod is relatively large, one can use a collimated beam of comparable size to directly measure the position of this focal point by Z-scan measurement for example as shown in Fig. 1.4 (a small aperture is longitudinally translated in order to find the maximum of probe-beam transmission [50]). This method is based on the assumption that the lens is perfect (without aberrations) and then is especially suited to transverse pumping with large-size materials.

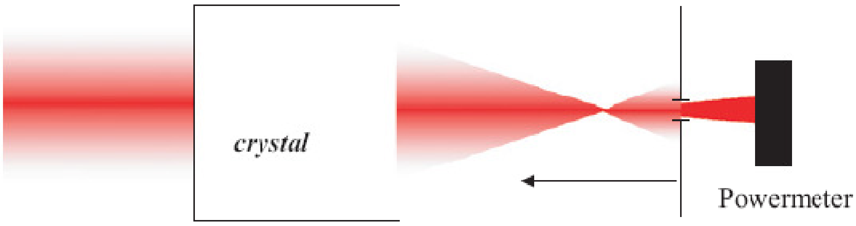

Fig. 1.4 Example of thermal lens measurement based on the displacement of the focal point [47].

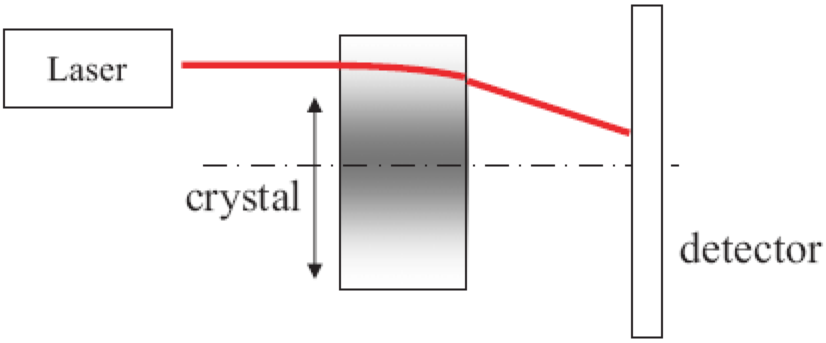

Fig. 1.5 Example of measurement based on deflection measurement [51].

We can use geometrical optics in another way by measuring the deflection of a probe beam. Instead of using a beam covering the whole pumped area, we can measure the deflection of a small beam slightly off-axis as shown in Fig. 1.5. The whole surface can be scanned in order to measure not only the focal lens but also the aberrations due to the thermal effects [51]. However, this method is complex and it can only be used for large transversally pumped crystals (even if the resolution can be lower than the probe beam size [52; 47]. Moreover, this method can be considered as a point-to-point measurement of the simpler Shack–Hartmann technique described later.

1.7.2 Methods based on the properties of cavity eigenmodes

After the development of end-pumped lasers (particularly thanks to the increasing performance of laser diodes), alternative methods appeared. These less straightforward methods are based on the properties on the laser cavity eigenmodes, in particular on the fact that the thermal lens affects the stability zones of a laser cavity [47]. All these methods are

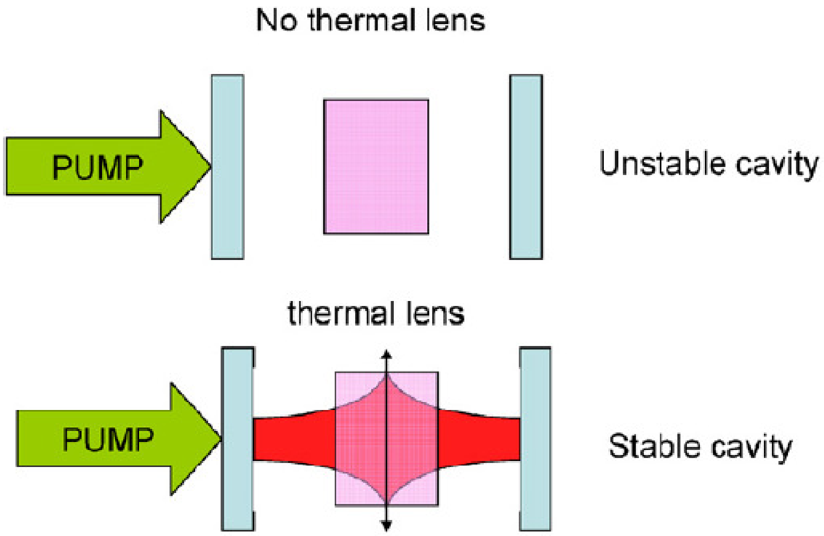

Fig. 1.6 Example of this influence of the thermal lens on the stability using a plano–plano cavity [53].

based on the theory of paraxial beam propagation theory in cavities presented by Kogelink and Li [54] and can be formalized using the ABCD matrices. An example of this influence of the thermal lens on the stability of a cavity is given in Fig. 1.6 Example of this influence of the thermal lens on the stability using a plano–plano cavity [53]. As a direct consequence, these methods consider ideal lens (aberration-free) and do not give any information on the thermally induced aberrations [47]. Nevertheless, these methods remain easy to implement since there is no probe beam (the laser itself is used to measure the thermal lens). In counterpart, it is impossible to measure the thermal lens in absence of laser extraction (with pumping but no laser emission) [47].

The methods based on the properties of the cavity modes allows to have relative precisions on the thermal focal lens of 15% for a TEM_{00} beam but down to 60% for an non-diffraction limited beam [53].

1.7.3 Classical interferometric techniques

As far as ''classical'' interferometry is concerned, one can consider equal-thickness fringes between the parallel end faces of the rod (this is the so-called Fizeau interferometer); one can also insert the rod under study in an arm of a Michelson-type [55] or Mach–Zehnder -type interferometer [56] for example. These methods are particularly well suited for large amplifier rods but in counterpart, they are not convenient for end pumping. Indeed, even if there is no fundamental contraindication to use this method for small spots, in practice in this case the number of fringes is too small to obtain an exploitable interferogram [47]. To overcome this problem, one can choose to take a probe beam larger than the pumped area. Some information on aberrations will be present, which requires an additional numerical model to fit the data and retrieve the thermal lens, as done by Pfistner et al. [57]. The weakness of this method relies precisely in the retrieving algorithm since the whole interferogram consists on only a few fringes [47]. The precision is then a hard point and in the best case this precision is evaluated to λ/4. This work [57] has also been done on YAG, GSGG and YLF crystals.

1.7.4 Shearing interferometric techniques

A classical solution to obtain information on the phase ''between two fringes'' is phase shift interferometry [47]. This technique has been used by Khizhnyak et al. [58] with longitudinally pumped Nd:YAG lasers.

Methods based on lateral shearing interferometers are particularly well suited to end pumping. The principle is the following: the beam is duplicated in several replicas, typically 2 [59; 60], 3[61] or 4 [62; 63](as presented in Figs. 24 and 25 with a tri-wave lateral shearing interferometer setup).

The replicas are slightly shifted from each other in the lateral direction, which provides an interferogram whose fringes (for 2 waves) or dots (for 3, 4 waves) separation give information on the derivative of the wave front. For example in the absence of wave-front distortion the lines are rectilinear for the 2-wave shearing interferometer, they form a homogeneous honey-comb for the 3-wave shearing interferometer and perfect squares for the 4-wave shearing interferometer. This technique is more sensitive than classical interferometry since the sensitivity is tunable by adjusting the shearing distance. The larger the shift, the more precise is the technique. The precision of this method is excellent since it is in the order of λ/50 [59] and can even reach λ/200 [61].

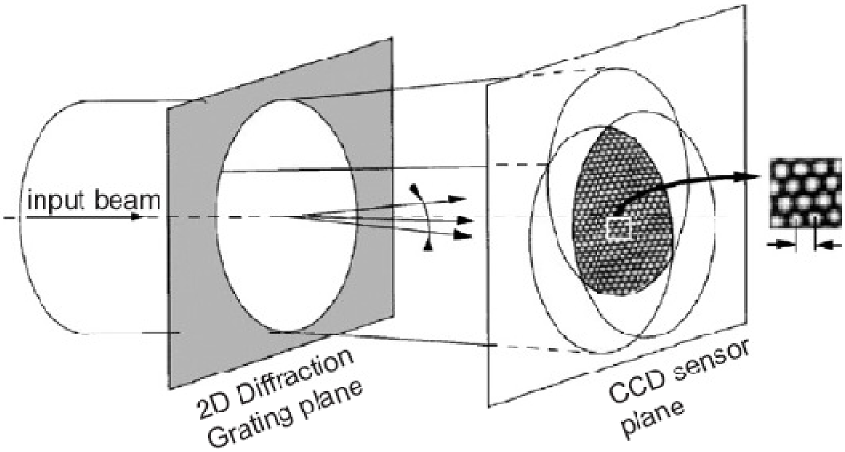

Fig. 1.7 Example of tri-wave lateral shearing interferometer [63].

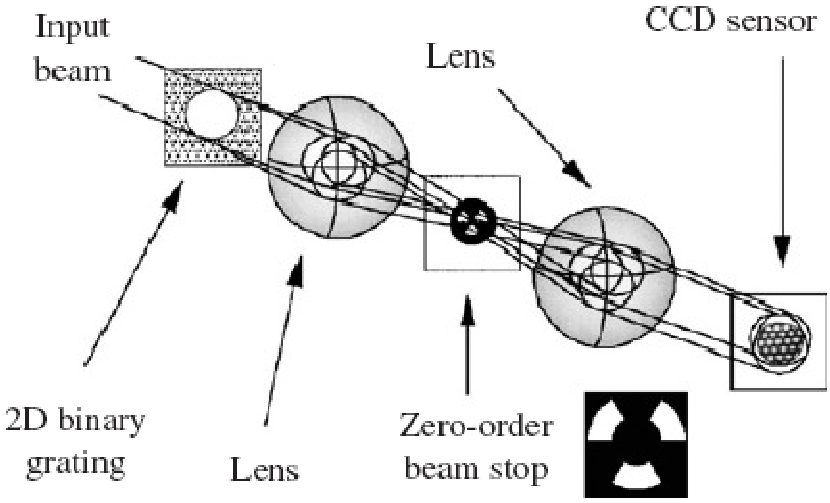

Fig. 1.8 Example of tri-wave lateral shearing interferometer setup [63].

The method using 3 (or 4)-wave ‘‘trilateral shearing interferometry’’[61] has the advantage over the 2-wave shearing interferometry to allow the cartography in the 2 dimensions in one acquisition. This method is simple to implement since the splitting of the beam can be realized readily with a 3D grating. Moreover, the use of a grating makes this method totally achromatic which allows its use for broadband lasers such as femtosecond lasers. In 1998, Chanteloup et al. [62]reported on the wave front distortions of a terawatt-class femtosecond laser system with an accuracy of λ/50. This method was also used to characterize thermal lensing in Ytterbium-doped materials, namely in Yb:YAB by Blows et al. [64], who used the 2-wave shearing interferometer technique to measure thermal lenses, and then thermal conductivities and fractional thermal loadings [47].

1.7.5 Methods based on Shack– Hartmann wave front sensing

In 1900, Hartman proposed to use a drilled plate [65] to measure wave fronts. The principle is simple: since light rays run perpendicular to the wave front, one can retrieve the local wave front slope as soon as the direction of the ray is measured. The Hartmann plate is made of small apertures which scatter the beam into regularly spaced diffraction patterns, and behind which is located a detector (typically a CCD camera nowadays). In 1971, Roland Shack and Ben Platt improved the Hartmann setup by replacing the array of holes by an array of microlenses (see Fig. 1.9).

The small axial shift of the microlens diffraction pattern centroid is directly proportional to the average local slope of the wave front on the aperture of the microlenses [47]. The displacement vectors allow having 2D information. The standard sensitivity of such systems is typically λ/100 RMS for commercial products, which settles this technique as a competitor of lateral shearing interferometry. One of the advantages of this method, compared to interferometric ones, is its insensitivity to mechanical vibrations or thermal fluctuations. In counterpart, the principal limitation of this kind of sensor is the discrete sampling that limits the transverse resolution and thus prevents from obtaining information about high-spatial-frequency phase distortions [47]. Nevertheless, it is noteworthy that this point is not a problem for thermal lensing and aberration measurements because in virtue of the general heat, temperature variations in a crystal are smooth even if the thermal load exhibits sharp variations.

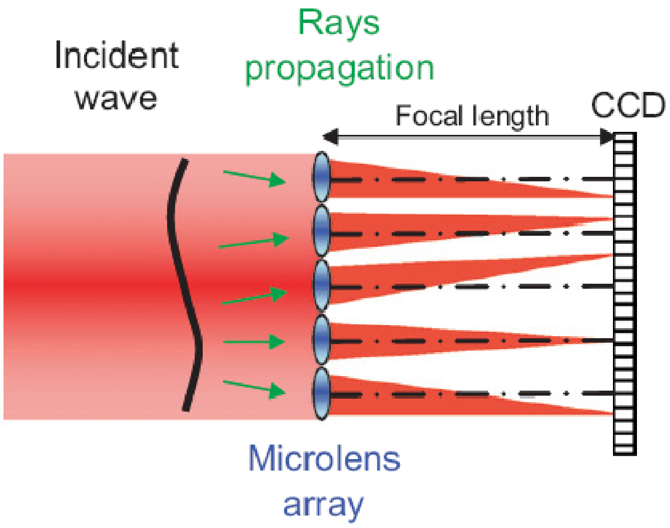

Fig. 1.9 Shack–Hartmann wavefront sensor setup [47].

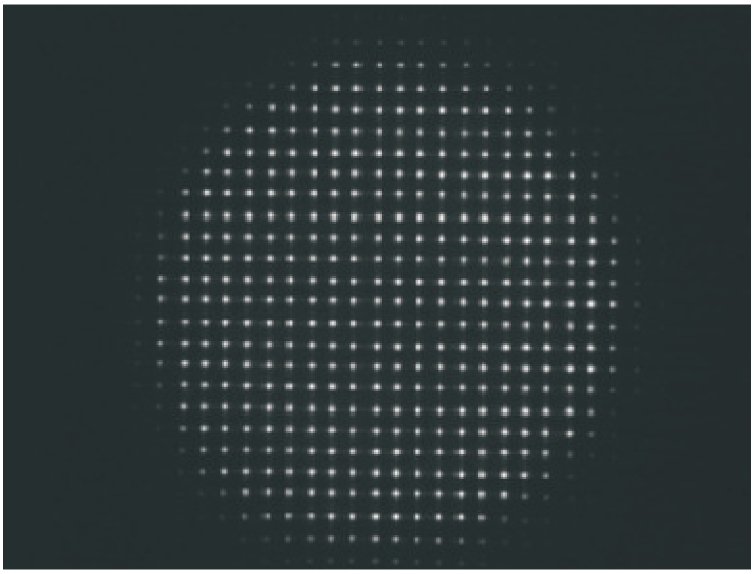

Fig. 1.10 Example of intensity pattern observed in the focal plane of the Shack–Hartmann microlenses.

1.7.6 Other techniques

There exist some more marginal and less used techniques to measure thermal lensing. For example, it is possible to achieve phase reconstruction basing on Fourier optics. One can show that it is possible to retrieve the phase by knowing the intensity profile in different planes linked by Fourier transformation [47]. For instance it is quite obvious that a uniform intensity over a circular aperture and an Airy pattern appearing in two Fourier related planes implies that the wave front propagating from one plane to the other is purely spherical. Nevertheless, the general inverse problem is far from being obvious. Grossard et al. [66] proposed a technique for measuring thermal lensing aberrations in a diode pumped Nd: YVO_4 crystal using intensity profiles in 3 planes and a complex phase retrieval algorithm derived from Gerchberg and Saxton's work.

2 Shack – Hartmann wavefront sensor for small dimension thermal lens characterization

Shack Hartman wave front sensor has numerous advantages compared to other thermal lensing techniques: it is insensitive to vibrations and allows real time acquisition in lasing and non lasing regimes. Comparing to its closest competitor, Shack Hartmann wavefront sensor offers straight forward phase reconstruction algorithms, and lacks implementation complexity of shearing interferometers [47]. The Shack-Hartmann wavefront sensor was built using 4.607mm focal length lenslet array and Dalsa 1M15 CCD camera. Lenslet array was manufactured by WavefrontSciences, its size 80x100 lenslets with pitch of 108 µm. The 632nm He-Ne laser was chosen as probe beam. Fig. 2.1 Shack Hartmann wavefront sensor construction. Fig. 2.1 shows a schematic of the operation of the wavefront sensor. The wavefront sensor measures the tilt over each aperture by comparing the measured positions of the diffracted spots to the positions of the diffracted spots for a reference input beam. The tilt measurements are then converted into a replica of the wavefront by performing a form of integration called wavefront reconstruction. Entire wavefront sensor operation and accuracy completely relies on software. One of initial tasks was development of reliable, accurate and fast software algorithm for Shack Hartmann wavefront sensor.

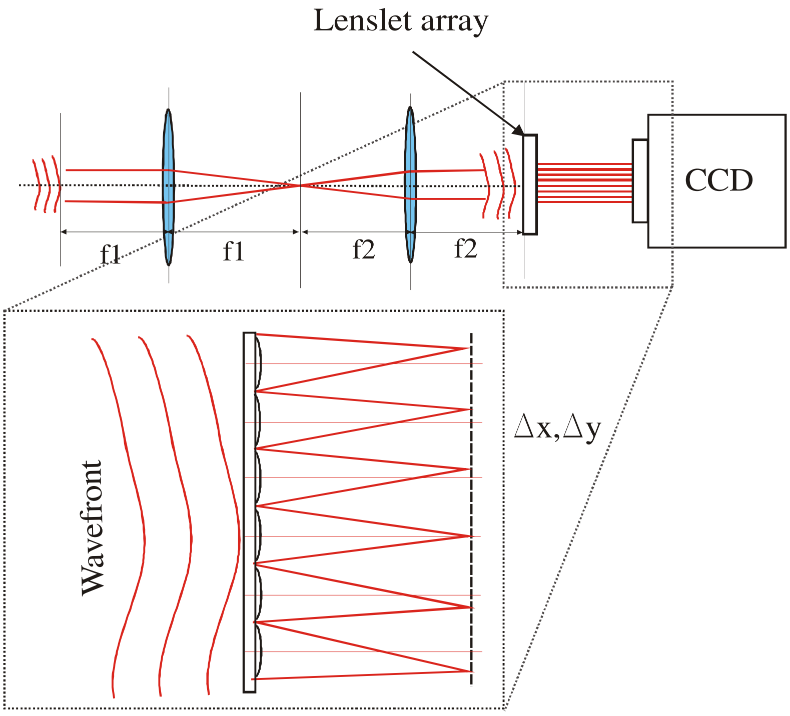

Fig. 2.1 Shack Hartmann wavefront sensor construction.

2.1 Diffracted spot location

The first step in measuring a wavefront is to determine the location of the diffracted spots. Algorithm based on MatLab functions in fallowing way: a) image is divided into smaller cells, containing one diffraction spot in each, b) evaluation of highest spot coordinates (*i,j*) in the cell, c) additional points are interpolated into image cross sections for x and y directions using *spline* algorithm (see Fig. 2.3), d) diffracted spot location according to highest point in *spline* function evaluation for x and y directions, e) for increased accuracy, steps c and d are repeated for additional cross sections *i*±1 and *j*±1.

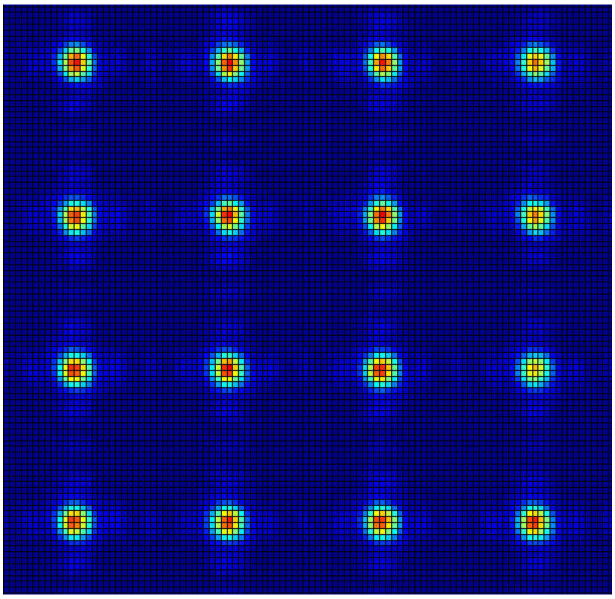

Fig. 2.2 Magnified diffracted spot pattern.

Unfortunately, initial test have shown, that in our setup, this algorithm did not ensured accuracy higher than 1 sub-pixel of CCD camera. This was caused by small diffraction spot size in lenslet array focal plane compared to CCD pixel size (14x14 µm). Lenslet array and CCD array pitch ratio of the equipment we have used is equal ~ 7,7, which results in diffracted spot occupying area sized ~2x2 pixels (measured at FWHM).

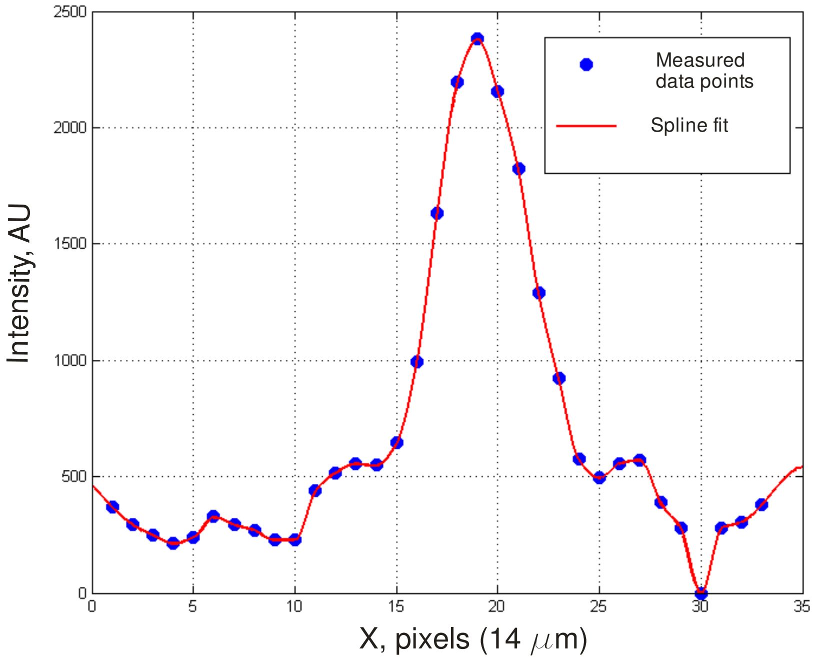

Fig. 2.3 Diffracted spot cross section.

For accurate determination of diffracted spot location simulation was performed, to find optimum spot size on CCD. It was found, that at least 5x5 pixel spot size is needed for sub-1/10 pixel accuracy, and 7x7 pixel diffraction spot size allows measurements of its location with sub-1/100 pixel accuracy. This simulation was performed in fallowing way: a) image, with known diffraction spot location was generated, b) noise corresponding to CCD cameras dynamic range added to image, c) diffracted spot location evaluated using interpolating spline algorithm, and compared to its known location. Acquisition error results for 1000 measured spots are shown in Fig. 2.4 and does not exceed ±0.01 pixel. Further magnifying lenslet array focal plane to CCD increases spot location acquisition accuracy, however, at the same time reduces number of spots that fit on CCD array, this way reducing resolution of wavefront measured. Wavefront resolution between 30x30 to 40x40 lenslets was determined for CCD camera we have used, by magnification ratio needed for accurate diffracted spot location acquisition.

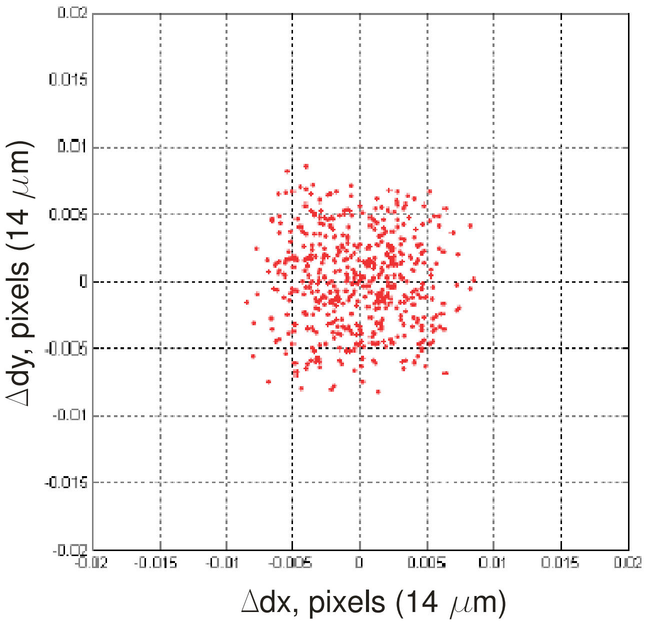

Fig. 2.4 Simulated diffracted spot location error. Zero corresponds to real center location.

2.2 Wavefront measurement and reconstruction

Measurements were performed with MatLab based wavefront measurement algorithm with graphic user interface (Fig. 2.5). Initially, reference wavefront diffracted spot locations are measured (for example probe beam passing laser active element in ambient temperature, with pump turned off). After reference has been saved, wavefront distortions can be measured - software takes snapshot from CCD camera and searches for spot centers in preset grid. Once spot locations have been evaluated, their dislocations Δx, Δy reference-wise are calculated. Local wavefront slopes can be evaluated:

$$Sy = \frac{d\phi(x,y)}{dy} = \frac{\Delta y}{f} \tag{2.1}$$

Typical local wavefront slopes measured with Shack-Hartmann wavefront sensor are shown in Fig. 2.6. Cursor direction and length indicates wavefront slope direction and angle (shown in arbitrary units). Once the local wavefront slopes have been determined, the wavefront can be reconstructed by performing a type of integration on the gradient measurements.

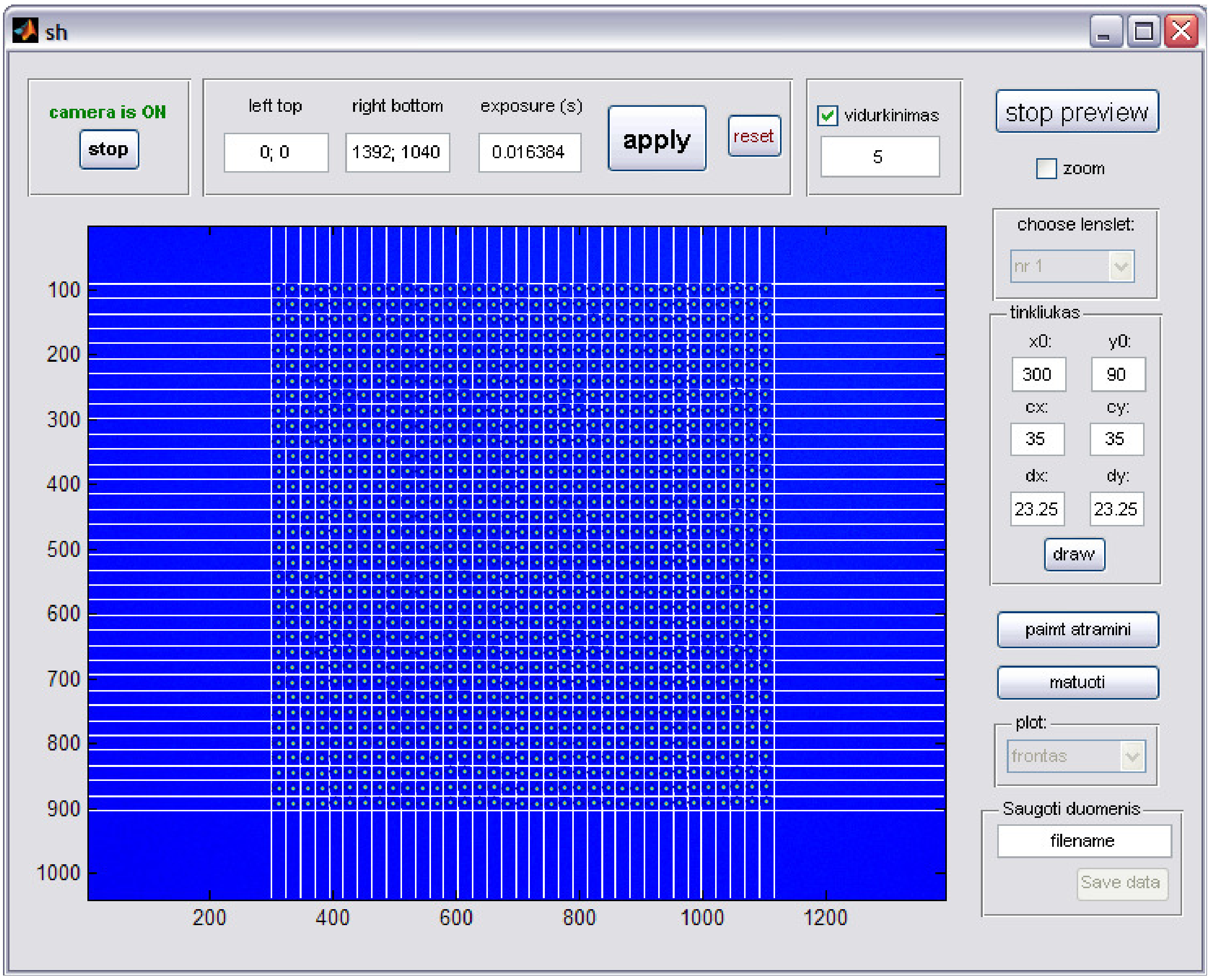
camera is ON

left top: 0; 0

right bottom: 1392; 1040

exposure (s): 0.016384

☑ vidurkinimas: 5

☐ zoom

choose lenslet: nr 1

tinkliukas

x0: 300

y0: 90

cx: 35

cy: 35

dx: 23.25

dy: 23.25

plot: frontas

Saugoti duomenis: filename

Fig. 2.5 Wavefront measurement software graphic user interface.

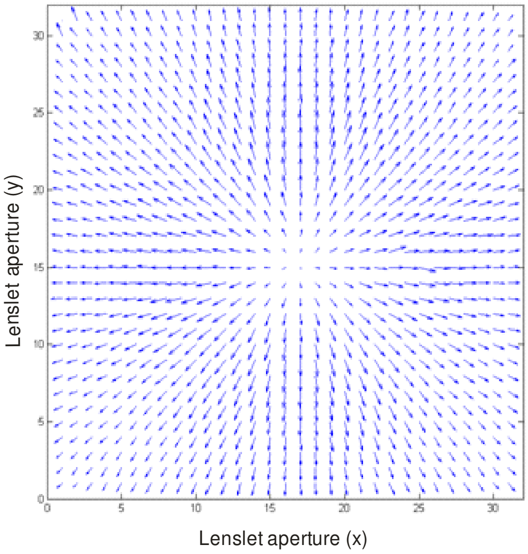

Fig. 2.6 Typical local wavefront slopes measured with Shack-Hartmann wavefront sensor (AU) (after probe beam passing pumped Nd:YVO$_4$ rod).

2.3 Linear Integration

In this simplest of wavefront reconstructors, the computer begins at one edge of the wavefront sensor slope data and defines the wavefront height at each integration area as zero. The height of the wavefront in the next adjacent integration area along the scan direction is calculated as the previous wavefront height plus the slope of the previous integration area times the aperture separation. Mathematically, this is given for the *x* direction by,

$$\Phi^{x}_{n,m} = \Phi^{x}_{n-1,m} + \frac{\partial \Phi_{n-1,m}}{\partial x} \times s'; \tag{2.2}$$

where ϕ is the wavefront surface and *s'* is the aperture separation. This is also performed in the *y* direction using the same formula. After the linear integration is performed along both axes, the wavefront height is found by summing both individual scans, or,

$$\Phi_{n,m} = \Phi^{x}_{n,m} + \Phi^{y}_{n,m}. \tag{2.3}$$

While this reconstructor is very fast, its results are very often noisy.

2.4 Southwell Reconstructor

William Southwell introduced a simple zonal wavefront reconstructor that is very popular because of its high speed and high accuracy [67]. The idea behind the Southwell reconstructor is to minimize the error between the reconstructed wavefront and the measured wavefront slopes. To achieve this goal, a scan is made through the entire grid of wavefront slope data and the wavefront height is calculated at each point as average height predicted by each of the neighbors as follows,

$$\Phi_{n,m} = \sum_{j=-1}^{1}\sum_{i=-1}^{1} I_{n+j,m+i}\left[\Phi_{n+j,m+i} + \left(\frac{\partial\phi}{\partial x_{n,m}} + \frac{\partial\phi}{\partial x_{n+j,m+i}}\right) * \Delta\right]; \tag{2.4}$$

where *n,m* ϕ is the wavefront at grid location (*n*,*m*), Δ is the separation between the (*n*,*m*) integration area and the (*n* + *i*,*m* + *j*) integration area, and $I_{n+j,m+i}$ is the intensity measured in the (*n* + *i*,*m* + *j*) integration area. The intensity weighting in the above equation is able to be toggled on and off by the user. It is present to give a measure of the validity of a wavefront slope measurement because generally integration areas with high intensity have a more accurate slope measurement. This algorithm takes many iterations through the measured wavefront sensor data to achieve an accurate result. The code allows the user to adjust the number of iterations through this reconstructor. The absolute maximum number of iterations should be equal to the number of integration areas, although it will always converge much faster for real data.

2.5 Thermal lens measurements

In order to image crystal face plane and match the dimensions of pumped region in laser crystal and lenslet array we used a magnifying 4f lens system. Magnification ratio was chosen to magnify area of interest size in the crystal (usually between 0.2x0.2 to 1.5x1.5 mm) so it covers 30x30 to 40x40 lenslets on the array (which corresponds to ~3x3 to 4x4 mm). Then, second 4f imaging system translated lenslet array focal plane to CCD at the same time magnifying it to dimensions of CCD array (14x14 mm). Such setup allows measurement of thermal lens with different aspect ratio, for example 20x60 wavefront spots, which is important for measurement of non symmetric thermal lenses.

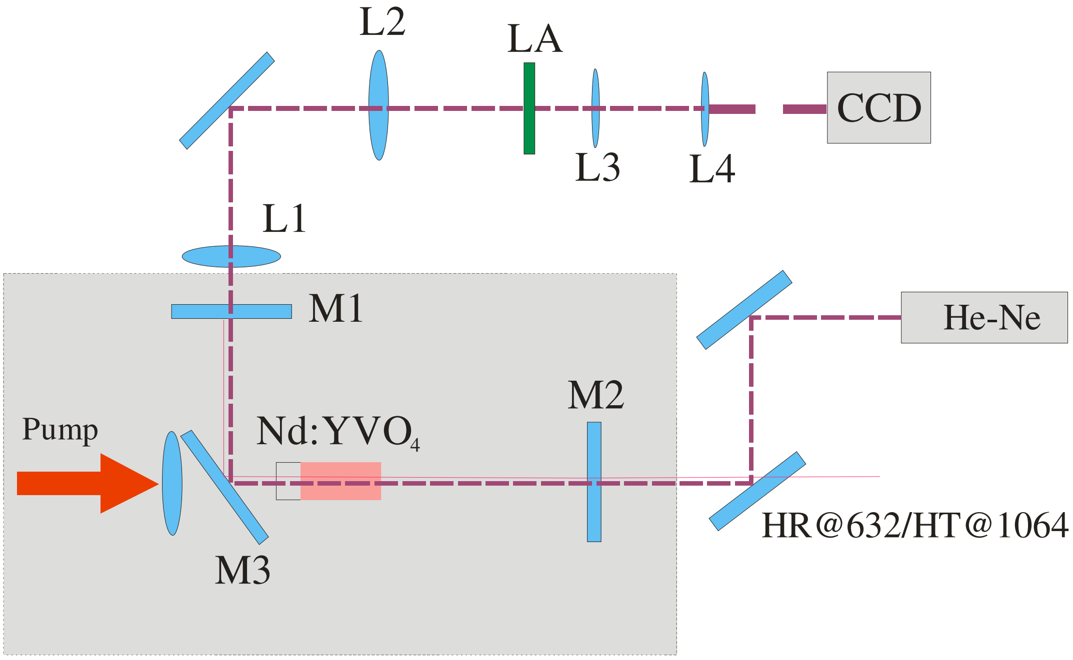

Fig. 2.7Typical thermal lens measurement setup. M1-M3 are laser cavity mirrors, M2 – laser output coupler. LA – lenslet array, L1 and L2 are lenses of first 4f system, used to translate and magnify crystal face to lenslet array. L3 and L4 are lenses of second 4f system used to translate and magnify lenslet arrays focal plane to CCD camera.

In order to determine the accuracy of the developed Shack Hartmann wavefront sensor we performed the test measurement replacing active element by f=30 mm spherical lens on translation stage. Lens focal length measurement for two different positions along probe beam axis is done, to evaluate accuracy of measurement setup. Ideally, focal length difference should be equal to distance between measurement positions. Element placement and its position determination error results in measured focal length error which varies from setup to setup, but does not exceed 10%.

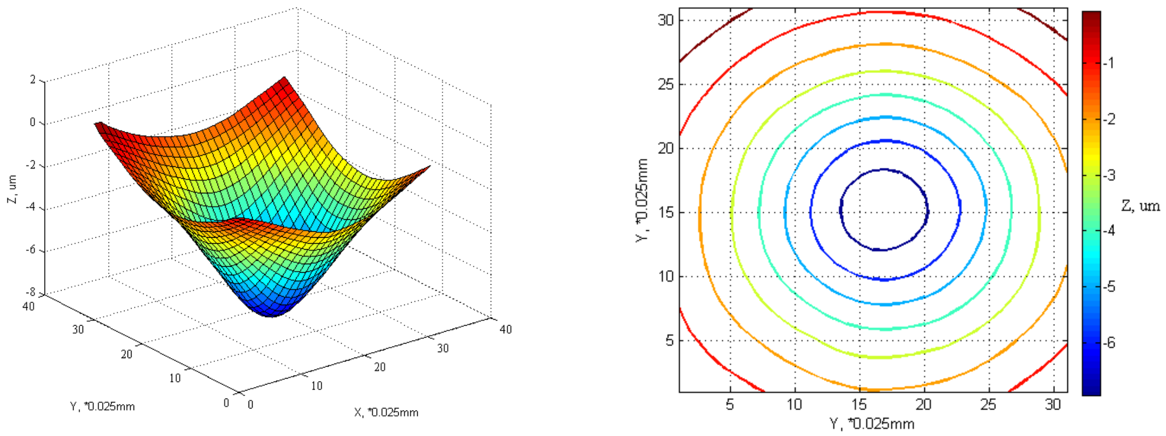

Fig. 2.8 Reconstructed wavefront measured with Shack-Hartmann sensor after probe beam passing pumped Nd:YVO$_4$ rod (pump power 17W).

For thermal lens focal length determination, wavefront distortions have to be measured first. Typical reconstructed wavefront measured with Shack-Hartmann sensor after probe beam passing pumped laser rod is presented in Fig. 2.8. Thermal lens focal length is calculated with help of MatLab based software, which functions in fallowing way: a) wavefront center is traced, b) wavefront tilt is compensated, c) using ray-tracing focal length dependence on distance from symmetry center is calculated. Measured thermal lens raytrace is presented in Fig. 2.9 a. Thermal lens aberration is clearly visible: for the center of the rod, focal length is ~20 mm, and drops to ~40 mm at edge of lasing mode (r=0.2 mm). For easier interpretation, thermal lens focal length dependence on distance from rod center is presented in Fig. 2.9 b. Our Shack Hartmann wavefront sensor allows measurement of spherical lens as short as 10mm and as long as ~2m. For shortest lenses, limiting factor is very high slope at edge of measured area: diffracted spot moves to neighbor cell, thus cannot be identified. This problem can partially be solved by reducing measurement area and resolution of wavefront.

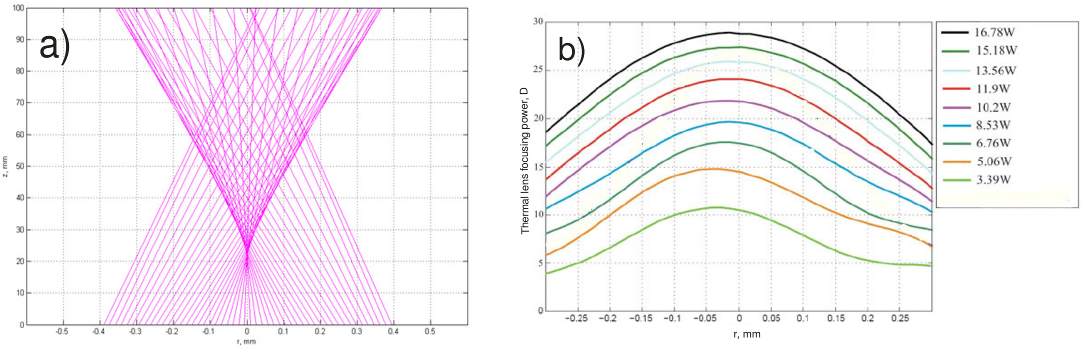

Fig. 2.9 a) ray-trace of wavefront distortions after probe beam passing pumped Nd:YVO$_4$ rod, b) thermal lens focal length dependence on distance from rod center. Cavity mode radius inside active element – 0.2mm, pump spot radius – 0.25mm, pump power 17W. Notably, focal length differs almost two times at the center and at the edge of lasing mode.

Longest focal length measured is usually limited by noise in central part of measured area: in center of spherical wavefront slopes can be so small, that diffracted spot dislocation approaches 1/100 pixel. Therefore, resulting noisy and inaccurate wavefront measured. However, thermal lens is always strongest in the center of measured area, and weaker at the edge of pump mode. This allows measurement of somewhat stronger thermal lenses than limits for spherical lenses.

3 Thermal lens compensation in high average power diode pumped Nd:YVO$_4$ laser using aspheric optical element

High average power, picosecond lasers have been studied intensely because of their suitability for industrial applications such as laser micromachining [68; 69; 70], drilling precise holes for fuel injection [71], thin film patterning for solar cells [72].

Neodymium doped yttrium vanadate (Nd:YVO$_4$) crystal is a promising material for high average power pico second lasers, because of its large stimulated emission cross-section, and broad emission band, in comparison with conventional Nd:YAG [73; 74]. However, the power scaling of Nd:YVO$_4$ lasers is limited by thermally induced optical distortions that are quite significant in these lasers due to poor thermal properties of active medium and lead to severe degradation of beam quality. The spherical component of thermal lens can be compensated by proper laser cavity design: choosing right radius of curvature and position of spherical resonator’s components. Nevertheless, the non-spherical component cannot be compensated in the same manner. This leads to reduced efficiency and multi-mode oscillation as the heat load increases. Spherical aberrations of thermal lens of the active media are quite severe when the solid state lasers are strongly pumped. The aberrations influence the diffraction loss, the output power, the mode profile and other laser beam properties [75].

Effective thermal lens compensation in diode-pumped and flash-lamp lasers employing phase-conjugatation has been demonstrated [13; 14]. This approach, however, has certain disadvantages, that include the use of fluid-filled or high-pressure gas cells (which defeats the all-solid-state characteristic of diode pumped lasers), high sensitivity of laser operation to induced grating parameters, thermal concerns in phase conjugation element for higher-power scaling. Thermally induced optical effects can be exploited to generate adaptive optical devices such as self-adjusting lenses. An adaptive lens in a resonator can be used to compensate for the thermal lens in a high-power solid-state laser rod and herewith significantly improve the beam quality and increase the output-power range of solid-state lasers. With suitable materials and an appropriate design of the compensating device, resonators with self-balancing thermal lenses can be developed [15]. Usually material with negative dn/dT is inserted between 2 identically pumped laser rods. However, this method is best suited for side pumping, and is not applicable for end pumped laser designs. Alternative technique for thermal lens aberration correction is the use of adaptive mirrors [76]. However, mirrors based on MEMS or piezo-crystals are relatively expensive and sometimes also lack in lateral resolution. Recently a thermo-optically driven adaptive mirror based on thermal expansion has been proposed [16; 17]. Although adaptive mirrors would allow thermal lens compensation in wide range of operation, they are not attractive for industrial application because of added complexity. As a good alternative to the expensive adaptive mirror a suitably shaped optical element, designed to cancel thermal distortions can be used instead [18].

In this chapter, results on compensation of thermal lens aberrations of high average power Nd:YVO$_4$ laser by the use of aspherically shaped optical element are presented. The highly reflecting optical element was shaped basing on measurements of actual thermal lens aberrations in active element, and manufactured using thin film deposition technology.

3.1 The experimental set-up and measurements of thermal lens aberrations

Experimental laser setup (Fig. 3.1) is based on optical layout of PL10100 (produced by Ekspla) regenerative amplifier. PL10100 features high pulse energy (up to 200 µJ), high beam quality ($M^2 < 1.5$) and a high repetition rate (up to 100 kHz) of typically less than 10 ps pulses. It consists of a diode-pumped passively mode-locked Nd:YVO_4 oscillator, and a diode-pumped regenerative amplifier [77]. However, parameters of this laser are optimized for highest output power which results in high lasing threshold and reduced beam quality at lower pump powers. Correction of thermally induced phase distortion in regenerative amplifiers active element could further improve parameters of this laser system in various operation regimes.

In order to design appropriate optics for thermal lens compensation we have performed the measurements of thermally induced lens in active medium when laser is operated at highest available pump powers. Experimental laser layout for thermal lens measurements is shown in Fig. 3.1.

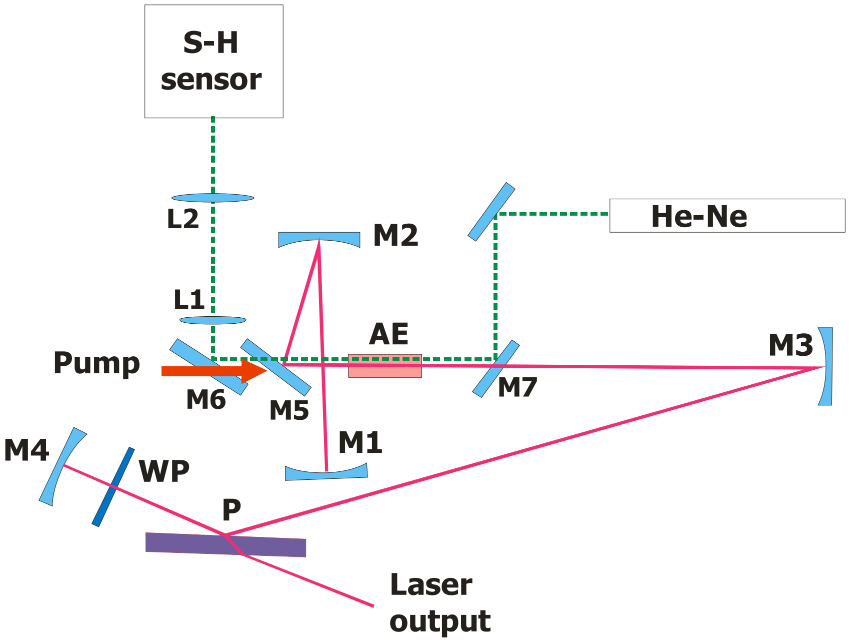

Fig. 3.1 Setup for measuring the thermal lens focusing power in laser active element by means of Shack-Hartmann sensor. M1, M2, M3 and M4 – cavity mirrors (M1=-1275 mm, M2 – R=4000 mm, M3 – R=-340 mm, M4 – R=-333 mm), P – polarizer, WP – λ/4 phase plate, M5 – pump coupling mirror, M6 and M7 – HT@1064 HR@632 mirrors for Shack-Hartmann wavefront sensor probe beam. L1 and L2 are 4f imaging system lenses. Thermal lens aberration compensator was designed to replace M2 cavity mirror.

Active element (AE) is 14 mm long Nd:YVO_4 crystal of 0.3% Nd concentration and 3 mm undoped caps on both ends. Aperture size of AE is 3x3mm. AE is pumped from both sides by two fiber coupled laser diode modules. We employed a Shack-Hartmann wavefront sensor for measurement of the phase distortions acquired by probe beam of He-Ne laser after passing the pumped laser crystal. The Shack-Hartmann wavefront sensor was built using 40x40 lenslet array with lenslet size of 108 μm and Dalsa 1M15 CCD camera.

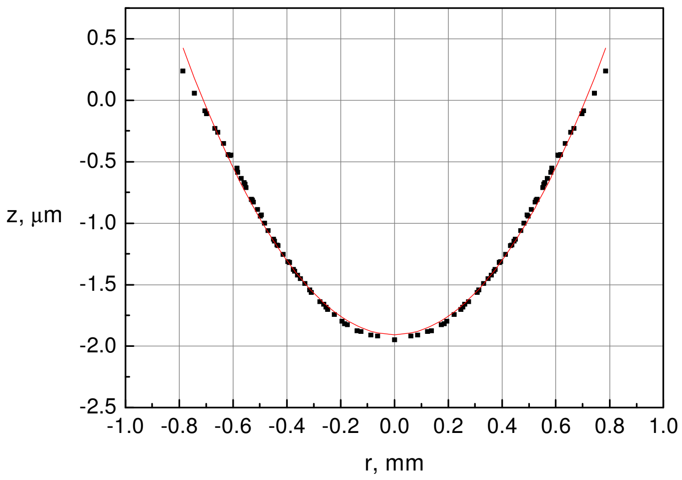

Fig. 3.2 Measured probe beam wavefront after passing laser active element. Dotted line marks measured spots, continuous line – r = 230 mm sphere (at 26,5W pump power).

In order to match the dimensions of pumped region in laser crystal and lenslet array we used a magnifying 4F imaging lens system. Measured probe beam wavefront cross-section after passing laser active element (at 26W pump) is shown in Fig. 3.2. Thermal lens focal length (f=230mm) was evaluated by fitting spherical wavefront to measured data. We have calculated thermal lens aberration by deducing spherical wavefront from measured data (see Fig. 3.3).

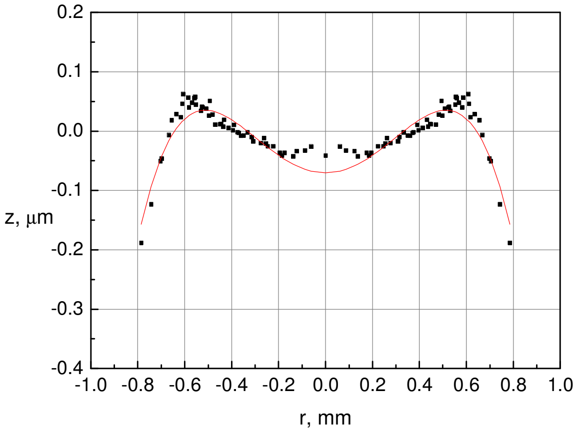

Fig. 3.3 Measured probe beam wavefront aberration after passing laser active element. Dotted line marks measured spots, continuous line – fitted spherical aberration.

3.2 Design, production and characterization of spherical wave compensators

The set of 10 samples for thermal lens compensation experiments were manufactured using thin film deposition technology. The same technique which is typically used for manufacturing of gradient filters is applied (Fig. 3.4). In order to form the profile of mirror surface, that is required for compensation of thermal lens aberration, Gaussian shaped spacer layer was deposited through the appropriate aperture on the geometric center position of each concave (*R*=-1750 mm) BK7 substrate. Every sample has different spacer layer parameters (width and height) that were designed in order to match the cavity mode parameters at compensator position in laser cavity and the thermal lens estimations obtained by Shack-Hartmann sensor. All substrates with spacer layer were further coated with high reflective (HR) conventional alternating $\lambda/4$ dielectric layers centered at $\lambda = 1064$ nm wavelength.

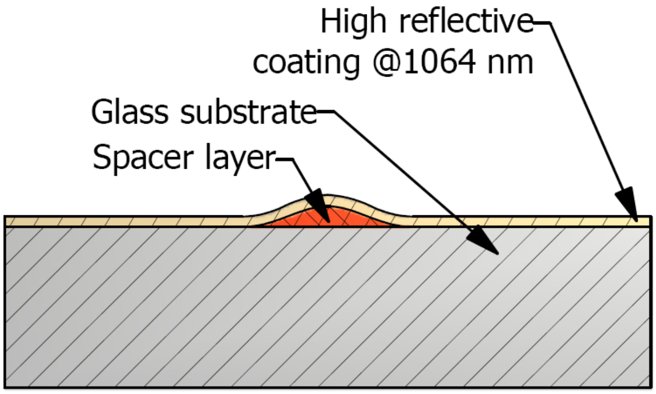

Fig. 3.4 Thermal lens aberration compensator design.

The wavefront distortions arising when probe beam is reflected from the curved compensator mirror surface were characterized using so called off-axis digital holography (DH) technique. DH imaging technique is capable to provide phase-contrast image of three-dimensional surface structure of the specimen by computational means with a single hologram (interferogram) acquisition [78; 79].

Michelson interferometer and CCD sensor were used for digital hologram registration in CCD plane. The experimental scheme is equivalent to that described in [80].

As a coherent light source for DH measurements we use spatially filtered and collimated radiation of Q-switched and frequency tripled Nd:YAG laser, producing pulses of ~4 ns duration at the wavelength of 355 nm with 10 Hz repetition rate. In fact the use of 355 nm instead of 1064 nm increases the resolution of interferometric measurements. The distance of 165 mm between the testing HR mirror and surface of CCD sensor was set. The numerical algorithm was further employed to extract the phase information of reflected light [78]. The typical phase difference diagram in reflected light obtained by DH is shown in Fig. 3.5. Compensator can be seen as curved mirror with aberration. From the phase information the relative surface height of thermal lens compensators can be extracted by using relation:

$$h = \frac{\Delta\varphi}{2\pi}\lambda. \tag{4.1}$$

Here $\lambda = 355$ nm is the wavelength used in DH measurements and $\Delta\varphi -$ phase difference in the wavefront of reflected light. The height profile extracted from phase information is shown in Fig. 3.6.

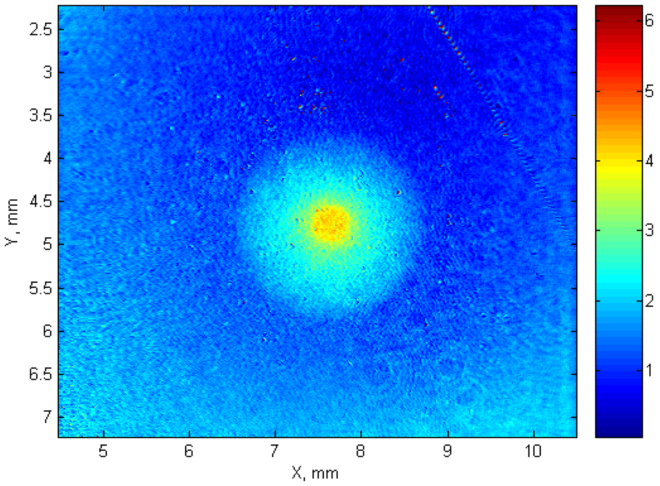

Fig. 3.5 Typical compensator phase difference diagram in reflected light obtained by digital holography.

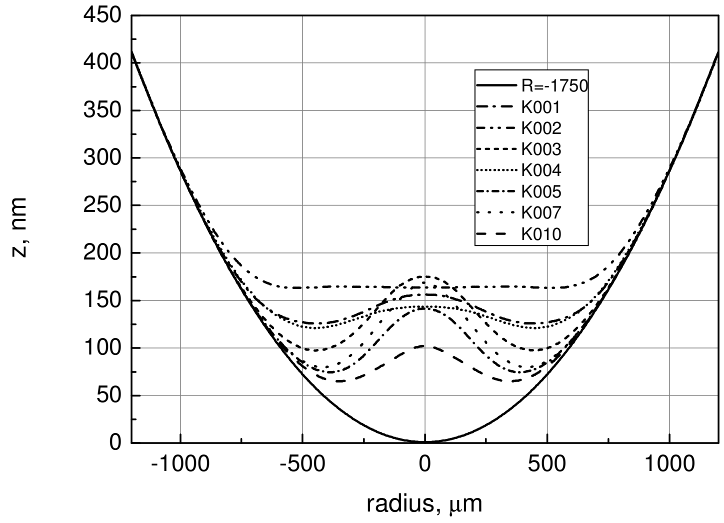

Fig. 3.6 Typical cross section of measured thermal lens compensator.

From sample measurement results, we estimate that sample K010 profile exhibits best match to measured thermal lens aberration presented in Fig. 3.3.

3.3 Experimental results

Thermal lens aberration compensators were placed in place of M2 mirror (see Fig. 3.1). Kinematic M2 mirror mount was attached to XYZ stage, to provide necessary degrees of freedom for optimal placement of compensator. The main criteria for compensator positioning in resonator was TEM_{00} output beam profile, M^2 parameter and output power.

As compensator is manufactured on spherical substrate, it can be considered as aberration compensator plus spherical mirror. By deducing aberration from compensator profile, radius of this spherical mirror was evaluated. We estimated, that concave R= -2000 mm curvature radius mirror is closest match for K010 compensator. Therefore, laser performance with R= -2000 mm mirror had to be investigated as well, in order to find out if laser performance changed because of different curvature mirror.

Initially, laser performance was investigated with convex R=4000 mm curvature radius M2 mirror that is standard element in PL10100 cavity. Laser free-running output power, beam quality parameter M^2 and output beam profile were measured. The same measurements were performed with 10 compensators. Measured laser output power dependence on pump power in CW operation regime is shown in Fig. 3.7. Highest slope efficiency was obtained when using R=4000 mm mirror. Maximum output power is closely the same for all samples tested. However, lasing threshold is almost 3 times smaller with compensator K010 and R= -2000 mm mirror as compared to case with R=4000 mm mirror.

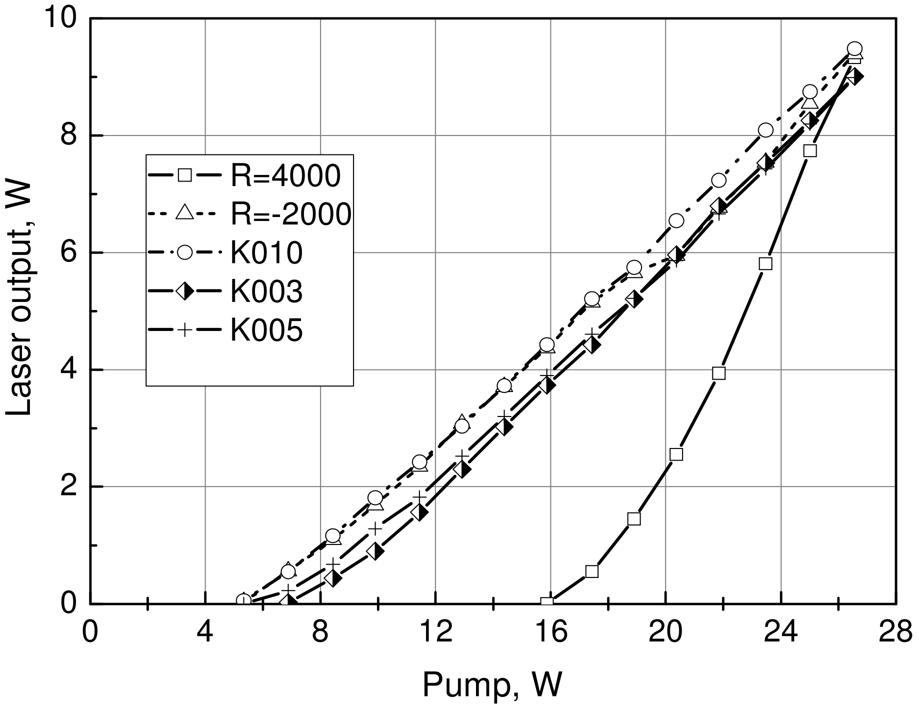

Fig. 3.7 Measured laser output power dependence on pump power in CW mode operation.

Beam intensity profile was measured by CCD camera at 200÷2500 mm distance from the laser output. These measurements were performed at maximum pump power, with different M2 mirrors and thermal lens compensators. In case when M2 curvature is R=4000 mm output beam near field profile is nearly Gaussian (see Fig. 3.8 a). However, due to thermal lens aberrations, intensity distortions are clearly visible in 1-2 m distance. As aberration component diverges (at distances 2.5 m and above), output beam profile becomes Gaussian. By replacing M2 mirror with compensator, significant output beam quality improvement was achieved (see Fig. 3.8 b). Laser output mode and power is sensitive to compensator X-Y position, but relatively insensitive to its Z position. Maximum laser output power with compensator can be higher by up to ~1,5W (compared to performance with R=4000 mm mirror), however, at expense of beam quality.

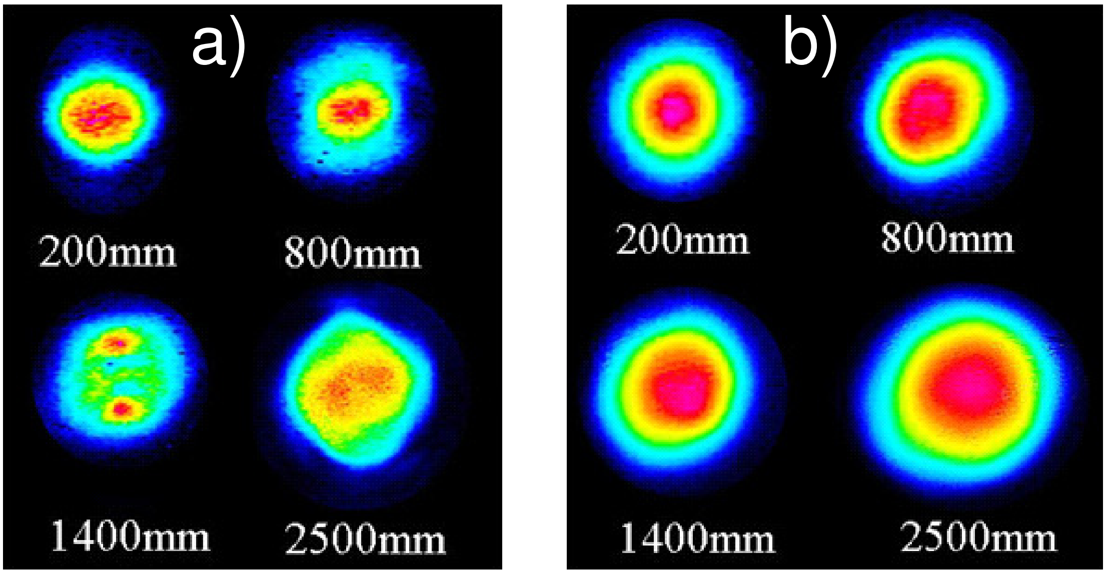

Fig. 3.8 Output beam intensity profile at various distances from output coupler when using: a) R=4000 curvature radius M2 mirror, b) K010 compensator.

Output beam quality was measured with Spiricon M2–200 Beam Propagation Analyzer. The results on beam quality parameter M^2 versus output power is presented in Fig. 3.9.

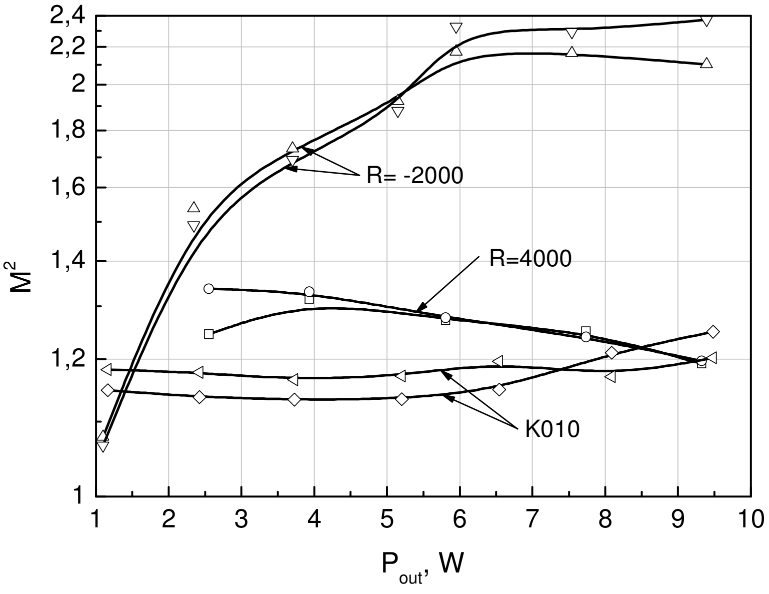

Fig. 3.9 Laser output beam M^2 parameter at different output powers (with different M2 mirrors and K010 compensator).

With mirror (M2) R=4000 mm ~9.5W output power and beam quality parameter M^2=1.2 was achieved at highest pump powers. However, output beam profile at 1-2 m distance from output coupler was unsatisfactory. For industrial applications, where laser is operating at highest output powers, high threshold is not an issue, but when lower output powers are needed, pump to output conversion efficiency drops rapidly. Replacing R=4000 mm mirror by R=-2000 mm, lasing threshold was reduced by more than 3 times, however, without positive impact on output beam profile and resulted in worse output beam quality parameter M^2 (above 2 at highest pump powers). Aberration compensator on the other hand, has improved all parameters mentioned above. Although output power was increased only by few percent, threshold is more than 3 times lower and output beam quality parameter M^2 does not exceed 1.2 in wide pump power range. Moreover, output beam profile was significantly improved compared to results achieved with R=4000 mm M2 mirror.

3.4 Summary

The static aberration compensator approach was shown to be well suited for high-power diode pumped lasers. This method has the advantages of greater simplicity and a wide applicability to laser designs. A diode-pumped Nd:YVO_4 laser with a 1.2 diffraction-limited output of 9.5 W using a thin film deposition technology made aberration compensator to correct the thermally induced phase distortion of the lasing medium has been demonstrated. Employment of proper thermal lens aberration compensator allows for laser threshold reducing and ensures improved output beam quality parameter M^2 in wide pump power range.

4 CW and Q-switched performance of a end-pumped Yb:YAG laser with elliptical mode geometry

Yb:YAG medium was demonstrated to be a promising candidate for efficient diode pumped laser systems. The large spectral linewidth of Yb in crystalline hosts, as compared to Nd, permits solid state laser operation with sub-picosecond pulses, using direct diode pumping. Another advantage of Yb-doped versus Nd-doped materials is the longer lifetime which may allow a better storage of the pump energy. Since Yb is a quasi-three level system, higher intensity pumping is required than for Nd lasers, but the thermal effects in Yb lasers are reduced as a consequence of a smaller quantum defect. The main reason for this is the very simple electronic level structure of the Yb^{3+} ion, which consists on two manifolds as shown in Fig. 4.1. This singular property allows avoiding most of the parasitic effects such as upconversion, cross relaxation or excited-state absorption which are present in Nd-doped materials [81]. This is a real benefit for reducing the thermal problems and thus to attain very high average powers [47].

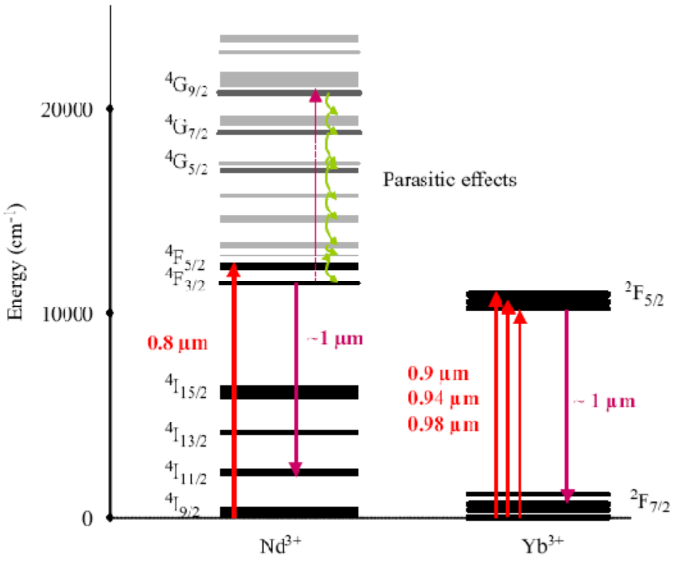

Fig. 4.1 Energy levels of Yb and Nd ions. Typical laser transition lines are represented for both pump absorption and laser emission [47].

Nevertheless, despite very low quantum defect in this medium the average power and beam quality of these solid state lasers are limited by the onset of thermooptic distortion and birefringence [82; 83]. A variety of resonator designs and novel pumping schemes has been invented in order to minimize these effects. One of the most significant steps in achieving high average powers was the development of thin disk laser [5]. However, this design tends to be quite complex due to multiple passes of pump beam through short active element. End-pumped schemes offer more reliable and less expensive laser designs yielding an optical to optical efficiency of more than 40% [10; 11]. Traditionally a rod-shaped active element was used in such setups. Unfortunately, this leads to depolarization losses due to thermally induced birefringence in laser active element [12]. Thin slab active element geometry is attractive due to efficient heat removal and offers more convenient distribution of thermally induced stress in active element, thus offering significant improvement of high power diode pumped solid-state laser operation [84]. However there is a limiting factor of crystal fracture due to stress, induced by non-uniform thermal expansion, as in end-pump geometry heat load is concentrated in a small volume while the rest of the laser crystal is cooled. Employment of elliptical mode configuration allows for larger mode area in active element and consequently for higher output pulse energies and average power scaling, as in that case heat load is distributed in larger volume without losing in cooling efficiency [85; 86]. However this approach leads to formation of power dependent astigmatic thermal lens which can seriously affect the resonator stability [87], therefore it requires nontrivial laser cavity design employing cylindrical optics and accounting for the dynamic focusing power of thermal lens. Although thermal effects in Yb:YAG lasers with elliptical mode geometry have been studied by R. Paschotta et al. [87], actual thermal lens measurements havent been reported.

In this chapter diode end-pumped Yb:YAG laser with elliptical cavity mode configuration is investigated. Results on numerical modeling of laser cavity based on measurements of astigmatic thermal lens in active element and on laser performance in free running and Q- switched mode featuring a high beam quality (M^2 <1.1) even at maximum laser powers are presented.

4.1 Measurement of thermal lensing

Elliptical pump geometry leads to non-symmetrical temperature distribution in laser crystal and, consequently to astigmatic thermal lens. The data on thermally induced lens in diode pumped Yb:YAG has been already published [29], however the measurements were performed only for case of symmetrical pump and lasing modes with pump power not exceeding 6 W. Therefore, in order to have more accurate data for laser design, the thermal lens measurements for elliptical pump configuration and for higher pump powers were performed. As an active element we have used Yb:YAG crystal of 5% doping concentration. The crystal was shaped as a thin plate of 1 mm height, 7 mm width and 5 mm length. The crystal was put between two sapphire plates on a water-cooled copper heat sink. Such configuration utilizes the largest surface area for effective cooling of thin plate-shaped laser crystal and this is especially effective when heat load is distributed in large crystal volume [86]. In order to achieve higher pump power densities we have chosen a pump scheme, where the laser active element is longitudinally pumped from both ends. We have used two high brightness polarization preserving diode laser pump modules of 40 W maximum optical output power at 940 nm wavelength. These modules are produced by Light Conversion, Ltd. and contain special assemblies of micro-optic elements that are used for shaping of diode laser bars radiation. The pump beam from the modules focuses to almost symmetric beam spot of ~ 250 μm diameter and has comparatively low divergence (beam quality parameters in different planes are M^2_{fast}= 12 and M^2_{slow}=27). The pump beam was reshaped to elliptical one with transverse dimensions of 280x1000 μm in laser crystal using system of lenses (PS – pump shaping optics). The resulting pump power from each diode laser bar after the reshaping of the beam was 26 W due to the losses on beam-shapers, lenses and mirrors.

We employed a Shack-Hartmann wavefront sensor for measurement of the phase distortions acquired by probe beam of He-Ne laser after passing of pumped laser crystal (see experimental set –up presented in Fig. 4.2). The Shack-Hartmann wavefront sensor was built using 40x40 lenslet array with lenslet size of 108 μm and Dalsa 1M15 CCD camera. In order to match the dimensions of pumped region in laser crystal and lenslet array we used a magnifying 4F imaging lens system. Different values of the imaging system magnification were set for thermal lens measurements in horizontal and vertical directions optimizing in this way the resolution of the registration system.

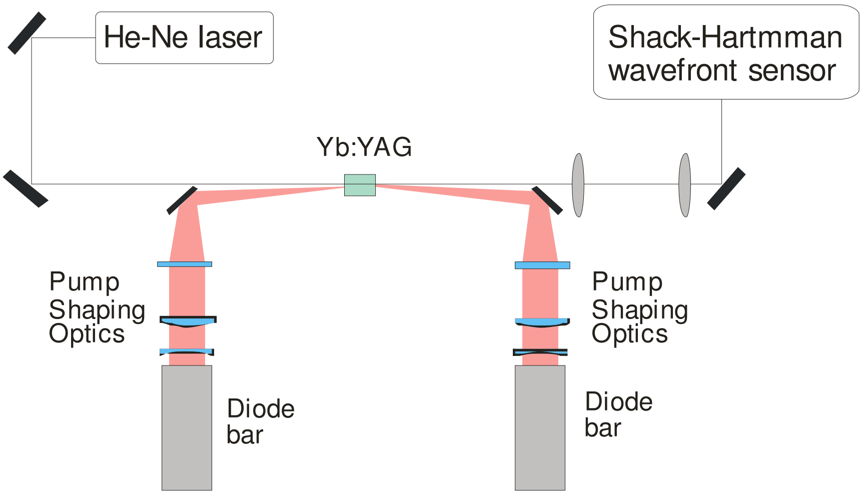

Fig. 4.2 Setup for measuring the thermal lens focusing power in laser active element by means of Shack-Hartmann sensor.

Variation of thermally induced lens focusing power calculated from data of wavefront distortion measurements versus total pump power is presented in Fig. 4.3. These results show that thermal lens's focusing power differs up to 10 times in horizontal and vertical directions at highest pump power.

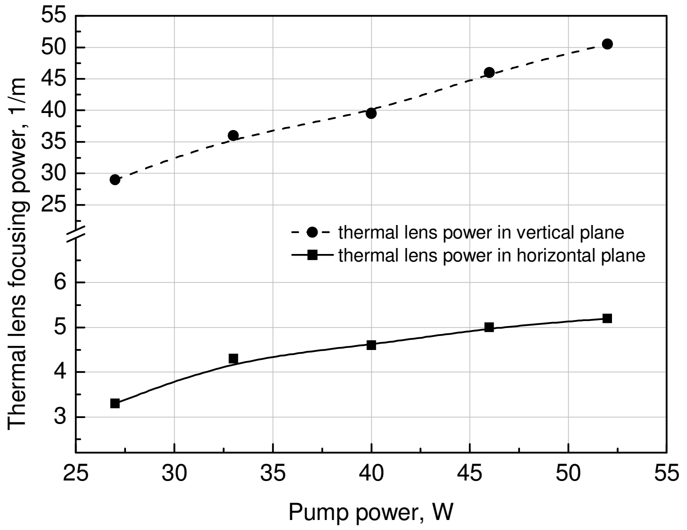

Fig. 4.3 Thermal lens focusing power in horizontal (width) and vertical (height) planes dependence on pump power, measured by Shack-Hartmann wavefront sensor. Thermal lens is highly astigmatic and its focusing power may differ up to 10 times in orthogonal planes.

Thermal lens measurements were performed in non-lasing conditions only due to technical limitations and complexity of experimental laser resonator. However we should note that in lasing conditions thermal lens can be up to 3 times smaller than in non–lasing conditions, as simulated emission dominates over fluorescence and non-radiative decay thus reducing thermal loading [29]. Therefore, an expected focal length of thermal lens in lasing conditions should be ~300÷600 mm range in horizontal and ~30÷60 mm range in vertical planes.

4.2 Laser design

4.2.1 Numerical modeling

The goal of this numerical modeling was to find out optimum laser resonator parameters at which the laser reaches stable operation and is least sensitive to thermal lensing. Additionally, the effects of an elliptical thermal lens on the resonators output mode were investigated.

Fig. 4.4 depicts the resonators model used in computer simulations. Cylindrical lenses, CL1 and CL2, were considered as thin lenses. The active element was replaced by variable strength thin lens, which stands for thermal lens induced in active element.

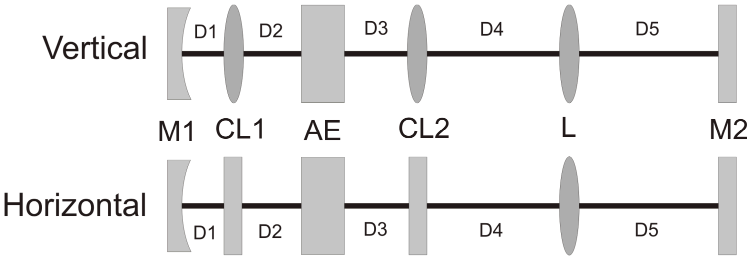

Fig. 4.4 Resonator model used in numerical calculations. M1 – spherical mirror R=1500 mm, M2 – flat output mirror, CL1, CL2 cylindrical lenses of f_{cl} focal length, AE – active element, L – lens f=500 mm.

The modeling was performed in two spatial directions: in vertical direction the curvature of cylindrical lenses CL1 and CL2 had an effect on the beam and in the horizontal direction. The thermal lens is considered to be astigmatic with focusing power varying in the ranges corresponding to ones evaluated from measurements. The resonator was modeled using ABCD matrix formalism well described in [88]. All elements in the resonator are given a corresponding ABCD matrix and the path of the beam is computed after one complete roundtrip around the resonator. ABCD matrices of the resonator elements are multiplied in the order in which the beam passed through them. The parameters of interest – stability parameter $\tilde{m}$ and output beam radius ω - were computed using following relations:

$$\tilde{m} = \frac{A+D}{2}, \tag{5.1}$$

$$\omega^2 = \frac{|B|\lambda}{\pi}\sqrt{\frac{1}{1-m^2}}, \tag{5.2}$$

where λ is the resonators operating wavelength, parameter $\tilde{m}$ representing is resonator stability is a half trace of all system ABCD matrix and is invariant regarding plane of reference, A, B and D are the elements of the cavity ABCD matrix.

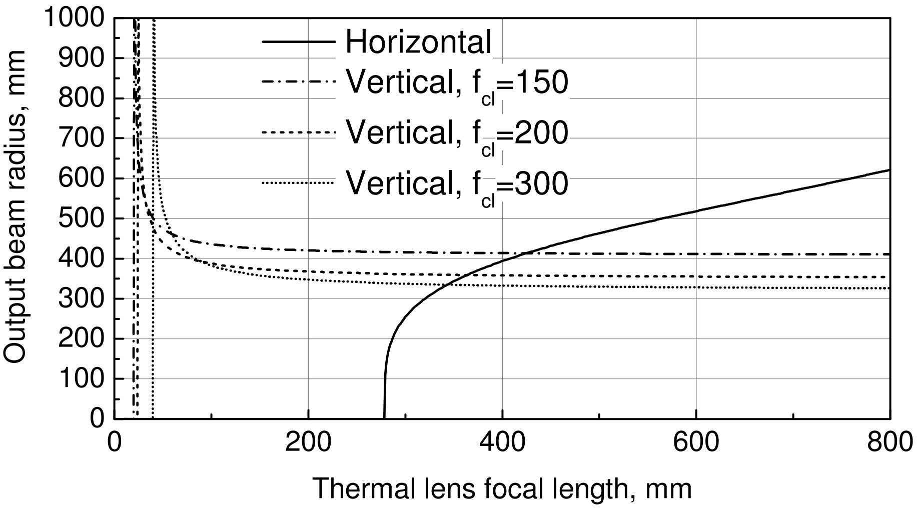

Fig. 4.5 Output beam radius versus thermal lens focal length at three sets of cylindrical lenses CL1 and CL2 (for horizontal and vertical directions)

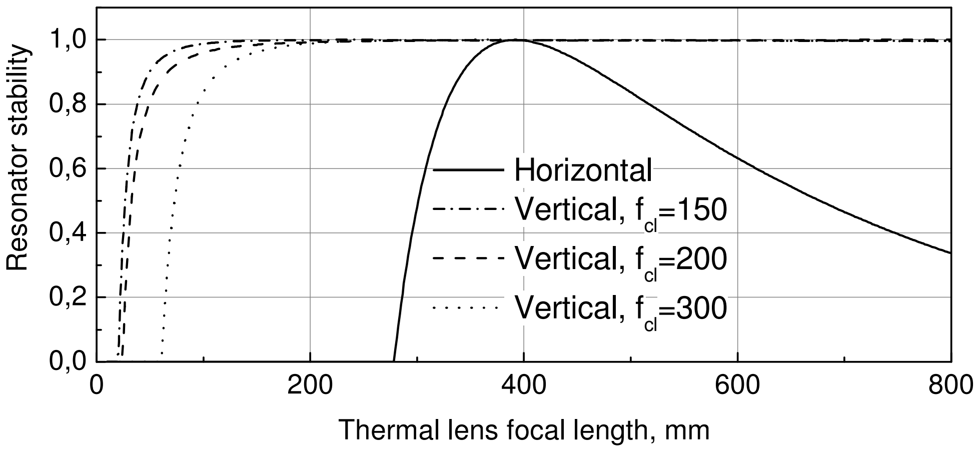

Fig. 4.6 Resonator stability versus thermal lens focal length at three sets of cylindrical lenses CL1 and CL2 (for horizontal and vertical directions)

Main criteria for resonator geometry selection was its stability within broad range of thermal lens values, with special attention devoted to high pump power range. Another important optimization criteria is good cavity mode overlap with pump beam in active element that ensures high eficiency of pump conversion to laser output. In addition we were seeking for circular beam profile at laser output. Different sets of cylindrical lenses were used in numerical modeling in order to find optimum performace for thermal lens values obtained from measurements. Cavity configuration was optimized with refference to criteria mentioned above, by changing position of cylindrical lenses inside resonator, without altering overall length of cavity. In all cases, distace between cylindrical lense and active element was slightly smaller than focal length of cylindrical lens. Obviously, mode parameters in horizontal direction are not sensitive to cylindrical lens focal length and position. Main results of numerical modeling are presented in Fig. 4.5-Fig. 4.7. As we can see from Fig. 4.5. output beam radius in vertical direction remains nearly constant for thermal lens focal lenghts above 100mm. For thermal lens focal lenghts bellow 100mm output beam size starts to rize, untill resonator becomes unstable (see Fig. 4.6). In horizontal direction, output beam diameter decreases, as thermal lens focal length drops. Numerical modeling shows, that for f_{cl}=150mm cylindrical lens output beam exhibits highest elipticity ratios at thermal lens values 300-400mm in horizontal direction, and 30-40mm in vertical direction (i.e. at expected thermal lens values estimated for highest available pump). Switching to 300mm focal length cylindrical lenses would result in less elliptical output beam profile, however, at cost of reduced resonator stability range in vertical direction, limiting it to thermal lense focal length value of 60mm. 200mm focal length cylindrical lens ensures stable resonator for thermal lenses above 25mm (in vertical direction), and has smallest output beam radius when thermal lens focal length is below 100mm (in vertical dirrection). Mode radius variation in laser cavity for different values of thermal lens (for f_{cl}=200mm) is shown in Fig. 4.7. One can see that chosen geometry leads to aproximately 240 x 800 μm beam spot size witch changes by no more than 10% when varying available pump power.

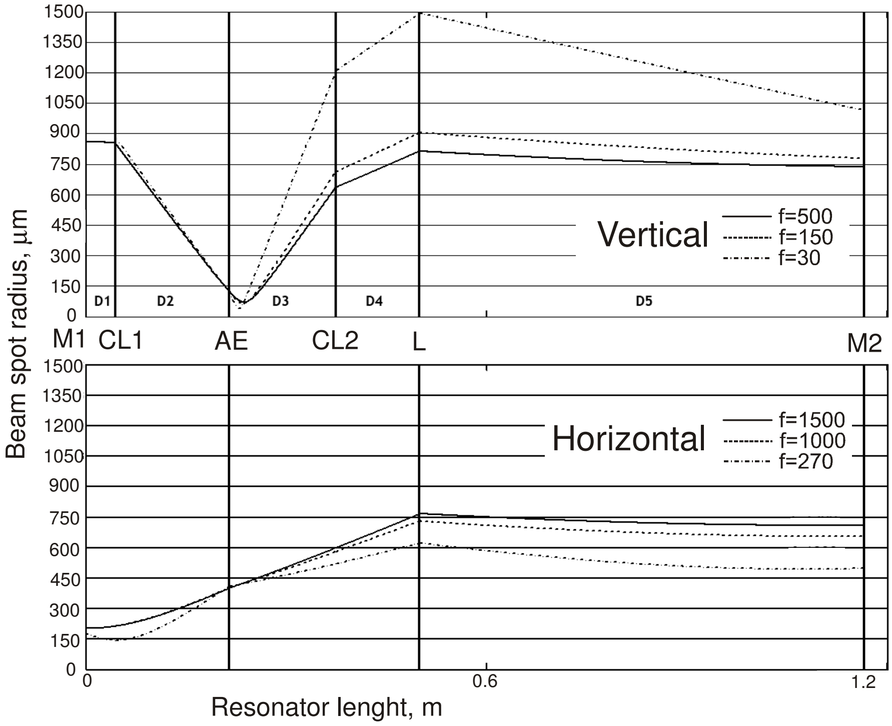

Fig. 4.7 Mode radius variation in laser cavity for different values of thermal lens (for fcl=200mm).

4.2.2 Experimental setup

The scheme of the resonator setup is shown in Fig. 4.8. There are two identical cylindrical lenses CL introduced into resonator to match elliptical lasing mode and pump beam inside the laser active element. Pockels cell modulator coupled with λ/4 phase plate was employed for Q-switch operation mode.

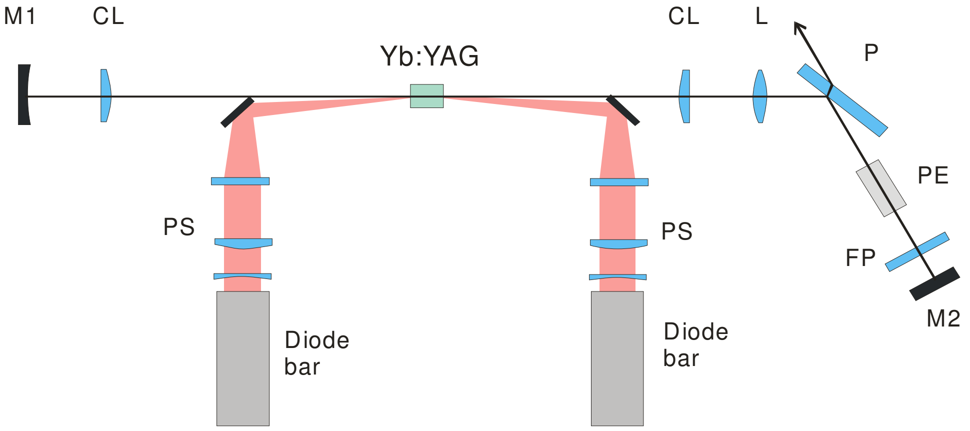

Fig. 4.8 Scheme of the resonator with elliptical mode geometry. Pump beams from two diode laser modules were focused into thin Yb:YAG slab from both ends into elliptical spot with transversal dimensions of 280x1000 μm. M1, M2 – cavity mirrors (R_{M1}=1500 mm, M2 - plane mirror), CL – cylindrical lens (F=200 mm), L – lens (F=500 mm), P – polarizer, PE – Pockels cell , FP – λ/4phase plate, PS – pump shaping lens system.

In this setup the pump was slightly non-collinear in order to avoid optical damage of laser diode modules by counter propagating pump beams.

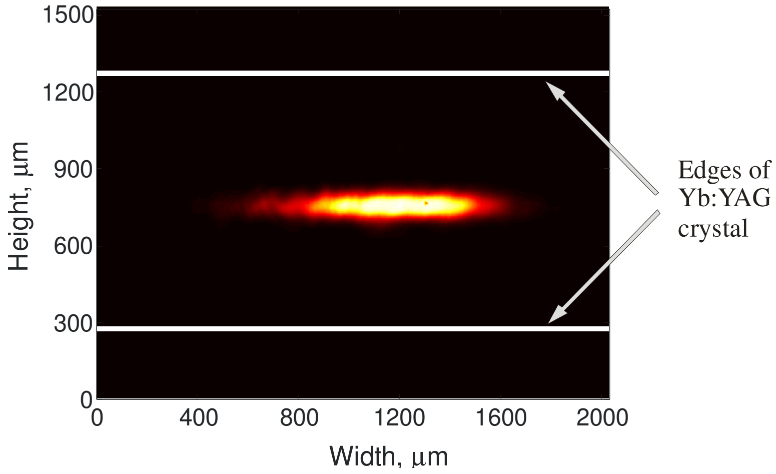

Fig. 4.9 Intensity distribution of laser radiation in active element. The beam spot dimensions are 150x1000 µm.

The actual lasing mode dimensions in Yb:YAG crystal was measured by imaging the crystal plane into CCD camera . For this measurement a fused silica plate was introduced in between Yb:YAG crystal and cylindrical lens CL and the reflection from the plate was directed through the imaging lens to CCD camera. The measured beam spot transversal dimensions were 150x1000 µm (see Fig. 4.9). The size of elliptical laser mode along major axis was close to that of the pump spot; however, its extent along the minor axis was by ~ 40 % less than pump spot size.

4.3 Laser operation in CW and Q-switched laser regimes

As the first step the laser was tested in CW operation regime. In this case the Pockels cell modulator was switched off and the laser output through polarizer was optimized for maximum value at given pump powers by changing the rotation angle of the phase plate. Such coupling of phase plate with polarizer is equivalent to laser operation with output mirror of variable transmittance. The dependence of average laser output power on pump is shown in Fig. 4.10. We have obtained a maximum laser output power of 8.3 W (lasing wavelength 1030nm) at 52 W pump power and the lasing threshold was about 15 W. These results are comparable to ones presented by other groups [84; 85]. The average slope of this curve is 24 %. Note the almost linear growth of the laser output with pump power indicating negligible impact of thermo-optics effect on laser operation.

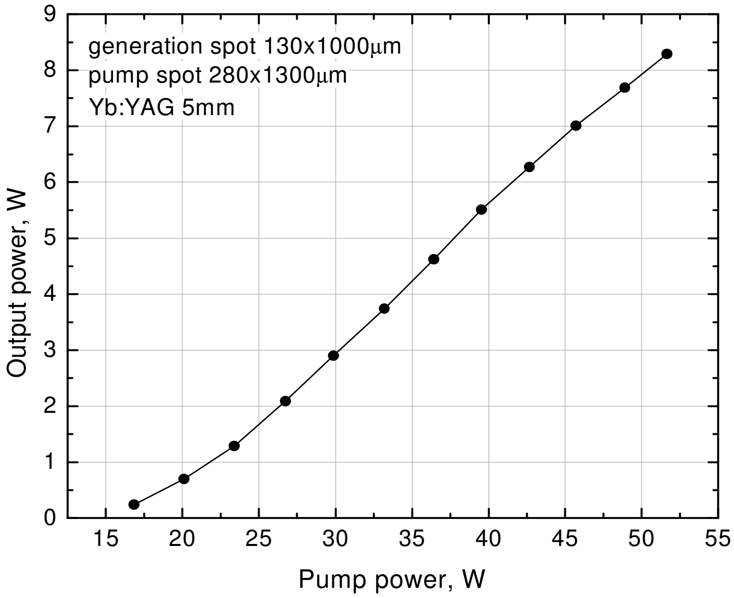

Fig. 4.10 Measured laser output power dependence on pump power in CW mode operation.

We have calculated the optimum effective output coupler transmittance using the values of average power of radiation leaking through the mirror M2 and found out that it steadily grows from 20-22% at threshold to the value of 38% at the maximum output power.

BBO crystal based Pockels cell of 3 mm clear aperture (LightGate 3 from Cleveland Crystal Inc)., and Pockels cell driver (PD4 from Bergmann Messgeräte Entwicklung KG) allowing operation at repetition rates of up to 100 kHz was employed for laser operation in Q-switched mode. Switching of the cavity to high-Q conditions were performed by applying ~ 2,12 kV pulse to Pockels cell. The moment of cavity dumping was regulated by pulse width of high voltage driving pulse and during the measurements was set to obtain highest average output power. The laser output pulse duration in this regime was 8 ns, which corresponds to duration of cavity round trip. The dependences of measured average out power and corresponding energy per pulse on laser repetition rate for different values of pump power are presented in Fig. 4.11.

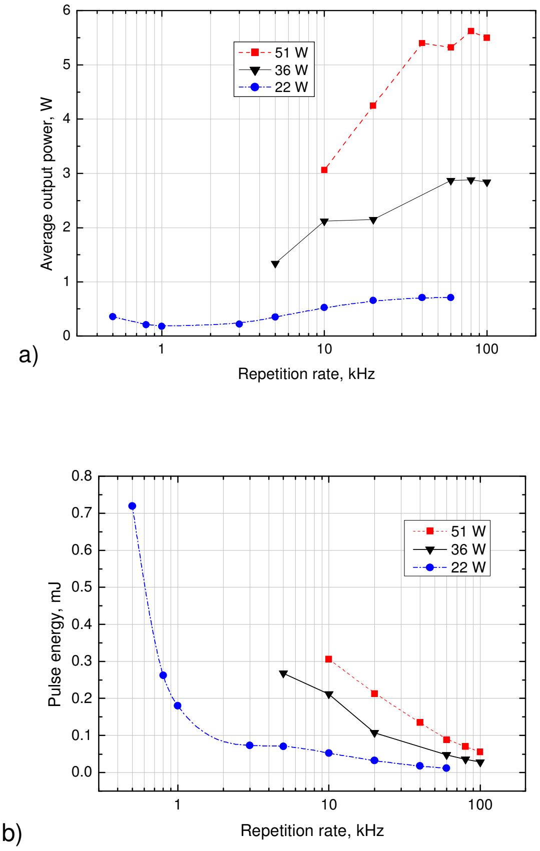

Fig. 4.11 Laser output in Q-switched mode operation: a) average output power versus repetition rate at given pump powers; b) laser pulse energy versus repetition rate at given pump powers.

The maximum average power of ~ 5.5 W was obtained at repetition rates of 30-100 kHz. We have observed a relatively fast drop of average power when decreasing the repetition rate below 30 kHz. That is caused by appearance of irregular pulsing of laser output when the laser cavity dumping rates approaches to the inverse upper state lifetime of Yb:YAG (τ= 0.95 μs) [89]. The appearance of this phenomenon is function of the high-Q phase duration, i.e. depends on the moment of cavity dumping. In the case when cavity dumping is performed in early stage of amplification the circulating pulse cannot extract the whole stored energy form the amplifier medium and a large fraction of initial gain remains at the end of the high-Q phase. In this case the active medium gain has enough time to recover during following low-Q phase. However, when setting the cavity dumping moment closer to the moment of amplification saturation the energy of amplified pulse increases while remaining gain at the end of high-Q phase decreases and the gain cannot recover the previous value during low-Q phase. As the result, the system becomes unstable and the laser output exhibits multi-energy behavior. So, during measurements the pulse width of high voltage driving pulse for Pockels cell was adjusted for maximum output power, but keeping the system in the stable operation conditions. We should note that at lower pulse repetition rates pump power was reduced in order to avoid optical damage of laser active element.

4.4 Beam quality measurement

Beam intensity profile was measured by CCD camera at ~4m distance from the laser output. As seen in Fig. 4.12, output beam profile remains close to Gaussian one even at highest output powers, however when pump power increases, symmetrical output beam becomes elliptical. According to numerical modeling (see Fig. 4.5), output beam dimension in horizontal plane decreases as thermal lens value increases. This leads to higher divergence in horizontal direction.

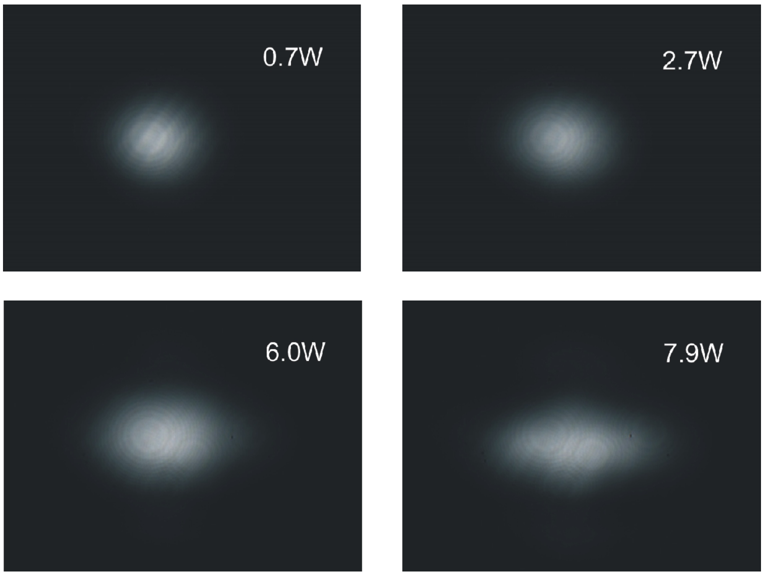

Fig. 4.12 Beam intensity profile taken by CCD camera at ~4m distance from the laser output.

We use a method described in ISO 11146 standard to measure laser beam quality parameter M^2. The beam is focused by a lens and then a number of beam spot measurements are made by CCD camera along the beam propagation direction. In our case we kept the lens position fixed and CCD camera has being moved to measurement positions. After determining of beam width in every position a comparison with Gaussian beam propagation was made in order to estimate M^2 parameter of the laser beam.

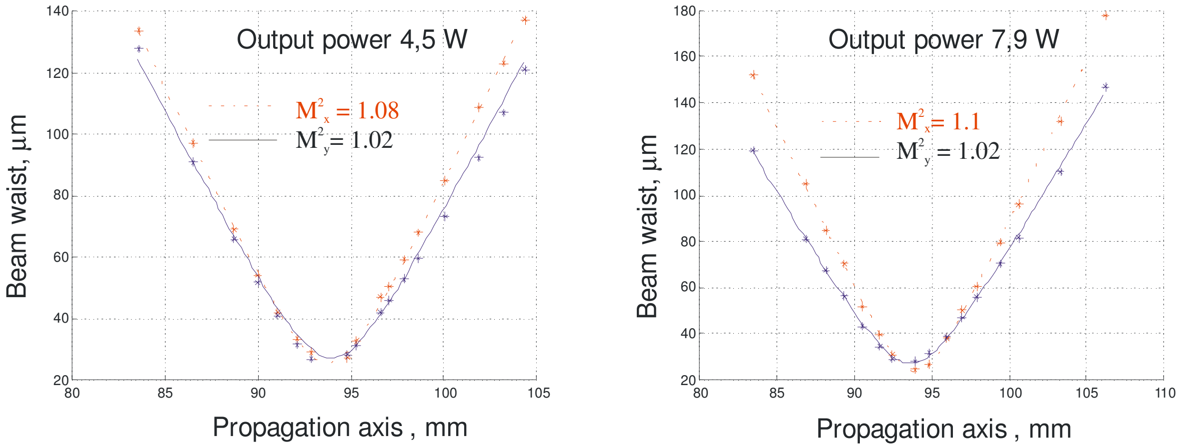

Fig. 4.13 Laser output beam M^2 parameter measurement at 36 W and 48 W pump power. Solid line corresponds to vertical beam section, dotted line – to horizontal.

As we can see in Fig. 4.13, the beam quality measurement resulted in M^2 values close to unity. The beam quality in horizontal direction is slightly decreased, as in vertical direction beam quality remains very good. This probably occurs due to high ellipticity of the beam in laser active element, meaning that the beam is more sensitive to thermal lens and its aberrations along the direction of larger beam dimension. We can also see that the laser beam is slightly astigmatic, as there is a focus shift between horizontal and vertical directions. However, as the beam quality is excellent even at higher powers and the astigmatism can be easily compensated by employment of simple cylindrical optics.

4.5 Summary

In this chapter the operation of diode end-pumped Yb:YAG laser with elliptical mode geometry was investigated in CW and Q-switch regimes. In Q-switch mode laser produced 8 ns pulses with average output power up to 5,5 W at pump power of 52 W, while in CW operation mode the 8 W output power was achieved. We have measured the focusing power of astigmatic thermal lens in laser active element and examined the quality of output beam at different output power. In spite of strongly astigmatic thermal lens due to optimized cavity design the output beam exhibit high spatial quality. Slight rise of laser output beam ellipticity reaching ratio of 1.2 for highest pump power was observed. Nevertheless, the beam quality parameter M^2 in both vertical and horizontal plane was close to unity, thus the output beam can be easily reconstructed to circular mode by cylindrical telescope. Such laser design offers good prospects for output pulse energy scaling of high average power diode pumped lasers.

5 Thermal lensing in high-power diode-pumped Yb:KGW laser

Femtosecond laser sources became promising tool for various scientific and industrial applications. High average power and repetition rates are required to speed up operation processes. Relatively broad spectral amplification bandwidth of Yb in crystalline hosts, along with small quantum defect, allows design of efficient, high average power femtosecond lasers, using direct diode pumping [90]. During the last decade, a lot of research has been committed to Yb^{3+} doped laser crystals like YAG, YVO_4, $KGd[WO_4]_2$ (KGW)and $KY[WO_4]_2$ (KYW) for the development of high power ultrashort pulse lasers has been shown [90; 10; 91; 92]. Yb:KGW exhibits an attractive set of parameters which makes it as one of the best choices for lasers operating around 1 µm. Small quantum defect together with absence of upconversion and excited-state absorption gives high slope efficiencies [93]. Intrinsic Yb:KGW birefringence allows for low intra-cavity losses caused by thermally induced birefringence. The broad gain bandwidth obtainable in these crystals makes available the femtosecond pulse generation. Another attractive feature seems to be existence of athermal crystal cut direction that helps to reduce thermal lens in active element of laser [30]. Although thermal conductivity in Yb:KGW is about three times lower than in Yb:YAG, it is, however, significantly higher as compared to Yb:glass, making the use of Yb:KGW quite promising for femtosecond pulse average power scaling. Average output power levels of ~ 130 W using femtosecond fiber lasers was demonstrated [94]. Main drawback of fiber laser design is small aperture of fiber core, which limits the maximum pulse energy to some 200 µJ before compression, with a compressed pulse width of 650 fs and pulse

energy of 100 µJ [4]. Although pulse lengths of ~200 fs are achievable in fiber lasers [95; 96; 97], due to small pulse energies those lasers are aiming at different market, where high repetition rate and high average power in sub picoseconds pulse length range is needed. The possibility to achieve high doping levels makes Yb:KGW attractive for thin disk laser applications. It has been demonstrated that thin disk lasers are well suitable for sub-200 fs pulses in 500 µJ energy range [98]. Such systems can be easily scaled to 1 mJ range. Thin disc lasers are well suited for extremely high output powers: around 500 W of output power in a diffraction-limited continuous-wave beam have been obtained with a single disk or around 1 kW using two disks [6]. So far, thin-disk lasers have lead to the highest average output power of 80 W from a mode-locked laser [7; 8], and pulse energies of > 20 µJ combined with sub-picosecond pulse durations are possible [9]. While typical pulse durations with Yb:YAG are around 700–800 fs, significantly shorter pulses are possible, e.g. with ytterbium-doped tungstate crystals such as Yb:KGW or Yb:KYW [99]. However, such designs tend to be quite complex due to multiple passes through short active element limiting in this way the use of such lasers in industrial applications. End-pumping schemes offer in most cases more compact and less expensive laser designs. Highest slope efficiencies have been reported for end-pumped configurations[10]. To our knowledge, highest average output powers up to date are demonstrated with commercial chirped pulse amplification systems Pharos [100] and FemtoRegen [101], with output powers up to 10 W and pulse energies of ~1 mJ at repetition rates of 1 kHz. With some exceptions, such as in [29], many of the Yb:KGW crystals in laser systems have been cut for propagation along the b crystallographic direction (b-cut), which is parallel to N_p, giving access to the largest absorption and emission cross sections. Thermal lens measurements in c-cut 5 at. %-doped Yb:KGW have been performed at relatively low absorbed powers in [29; 28]. Unfortunately, data regarding thermally induced astigmatism have not been reported there. However, based on recent measurements of thermo-optic coefficients and thermal expansion using homogeneous heating, Biswal et al.

[102; 103] proposed possible athermal propagation directions, where the thermooptic and thermal expansion effects approximately cancel each other. One of the proposed directions for the light polarized along the N_p axis is in the *m–g* plane, 15º clockwise from the optical axis N_m [102; 103]. This athermal direction was investigated by J. H. Hellstrom at el. [30]. Another athermal orientation of interest is for E||*m* because the emission and absorption cross sections for this polarization are significantly higher in Yb:KGW. The athermal direction of propagation is located ±46º from the N_p axis in the N_p-N_g plane as shown in (b) [102].

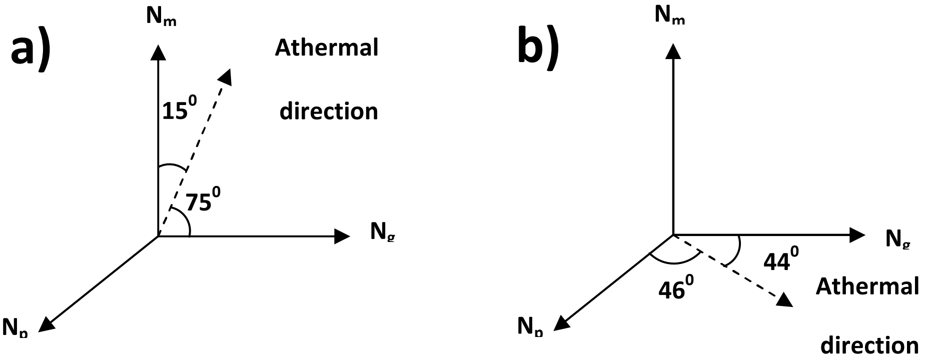

Fig. 5.1 (a) Athermal direction of propagation relative to the principle axes for KGW in the *m-g* plane for E||*p*. (b) Athermal direction of propagation in the *p-g* plane for E||*m*. Adapted from [102].

The goal of this chapter is to investigate and compare properties of the thermal lensing and thermal beam distortions in high-power laser diode end-pumped Yb:KGW crystals cut for beam propagation along the N_g axis and along the athermal direction in the N_p- N_g plane.

5.1 Experiment

Two types of Yb:KGW crystal were used: first was cut for light propagation along the N_g crystallographic direction (see a)[104] and second was cut for propagation along athermal orientation (see b)[102]. We have used 5 mm length, 6x1,2 mm aperture and 1,6 at. %-doped active elements pumped by two high brightness, polarization preserving laser diode pump modules of 50

W maximum optical output power at 980 nm wavelength, produced by Light Conversion Ltd., and ensuring pump intensity on the crystal up to 70 kW/cm^2. Crystal orientation and orientation of thermal expansion axes [102; 103; 104] in relation to laser beam propagation is shown in Fig. 5.2.

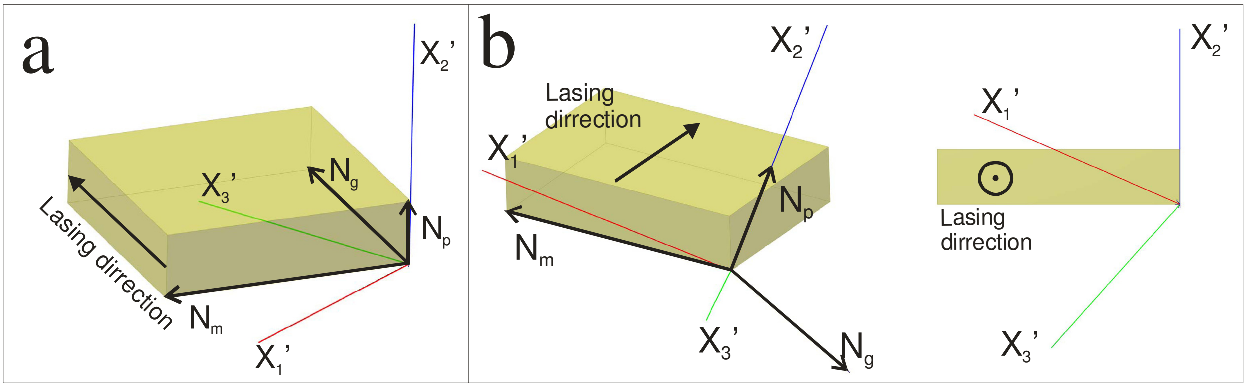

Fig. 5.2 a) N_g-cut crystal orientation in relation to direction of propagation. Thermal expansion axes X_1' and X_3' are in N_m-N_g plane, X_2'is orientated along N_p axis. b) Athermal direction cut crystal orientation in relation to direction of propagation. Thermal expansion axes X_1' and X_3' are in N_m-N_g plane.

The schematic diagram of experimental setup that employs slab shaped Yb:KGW active element is presented in Fig. 3 . Resonator consists of flat mirror M3 (reflectivity R=100%) and spherical mirrors M1 and M2 (radius r= -300 mm, R= 100%). Other components are λ/4 phase plate FP and pair of the thin-film polarizers P. The polarization plane of pump radiation in all the cases was parallel to N_m optical axis.

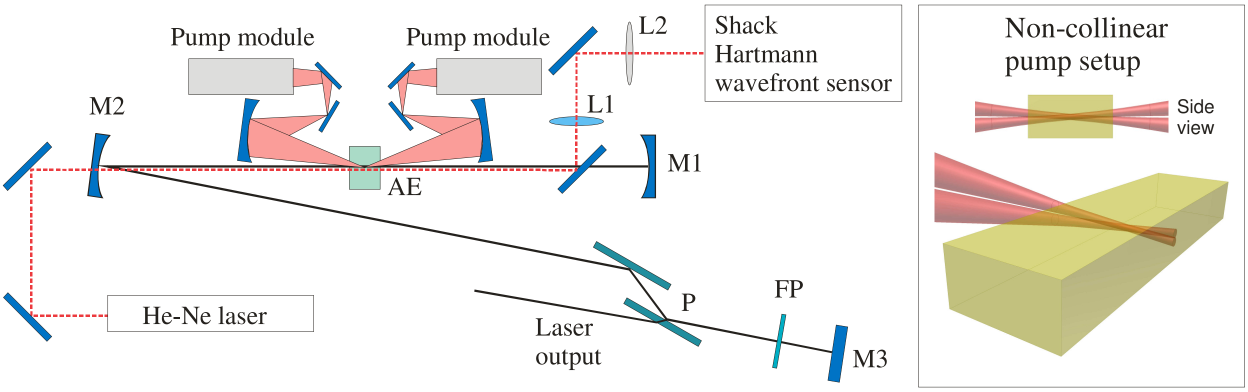

Fig. 5.3 Experimental setup. Pump setup of laser active element is shown on the right. Note, that non-collinear arrangement of pump beams results in oval shaped pump distribution at active elements facet.

We employed a Shack-Hartmann wavefront sensor for measurement of the phase distortions acquired by probe beam of He-Ne laser after passing of pumped laser crystal (see experimental setup presented in Fig.3). The Shack-Hartmann wavefront sensor was built using 40x40 lenslet array with lenslet size of 108 µm and Dalsa 1M15 CCD camera. In order to match the dimensions of pumped region in laser crystal and lenslet array we used a magnifying 4F imaging lens system (lenses L1 and L2 in Fig.3). Additional mirror M4 (anti reflective coated for lasing wavelength 1030 nm and high reflective for 632 nm probe beam) was used to pickup probe beam from laser cavity. Such setup allows measurements of thermal lens in both lasing (with laser oscillation) and non-lasing conditions (with laser cavity blocked).

5.2 Thermal lensing in N_g-cut Yb:KGW active element

At the first stage of experiments we examined N_g-cut active element. Thermal lens measurements were carried out at various pump powers for lasing and non-lasing conditions. Typical probe beam wavefront distortion after passing thermal lens in N_g-cut active element at highest pump power (lasing conditions) is presented in Fig. 5.4.

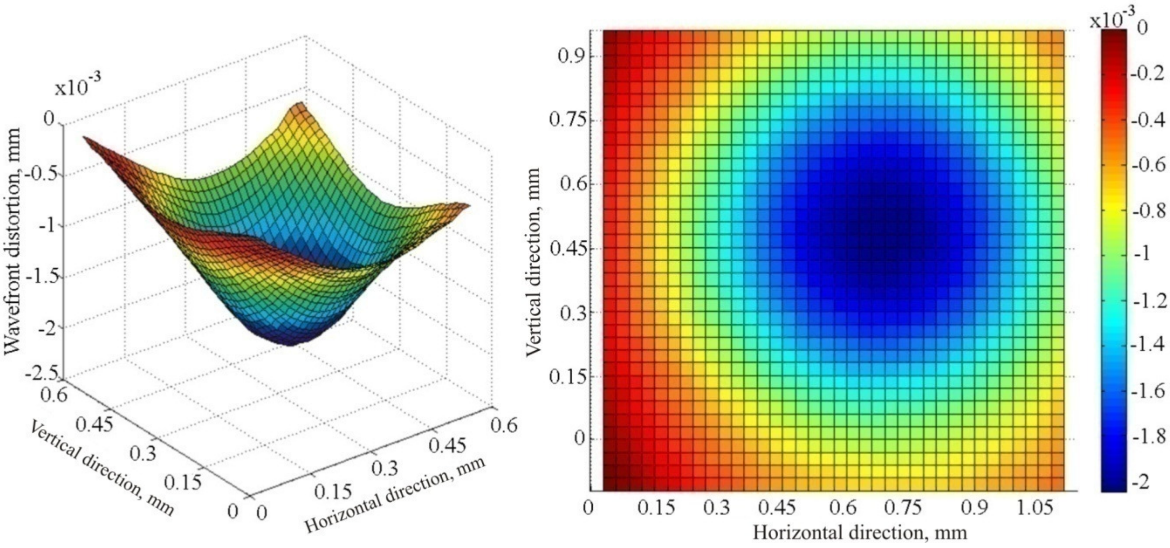

Fig. 5.4 Measured probe beam wavefront distortion after passing thermal lens in c-cut active element at 94W pump power (lasing conditions).

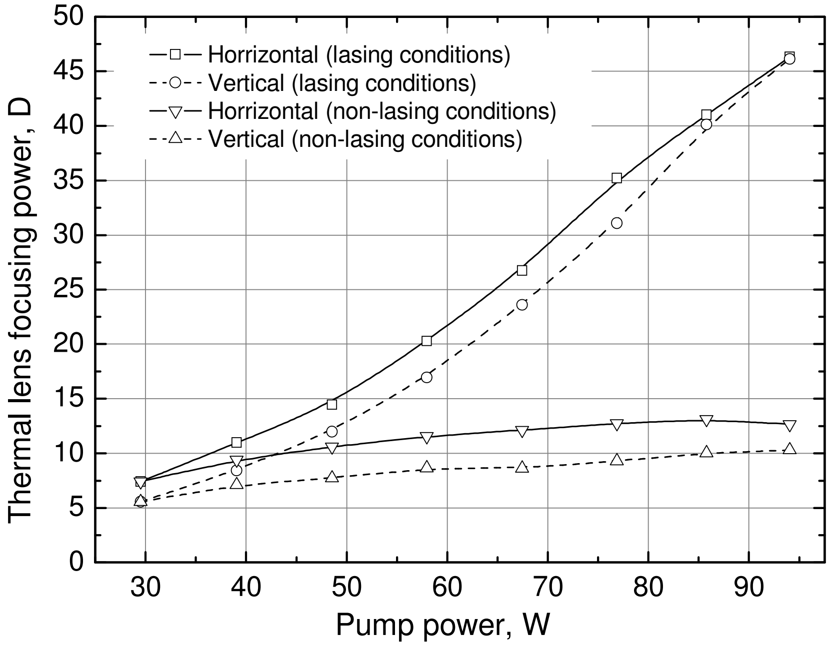

Fig. 5.5 Thermal lens focusing power for vertical and horizontal directions in lasing and non-lasing conditions at different pump powers.

Variation of thermally induced lens maximum focusing power calculated from data of wavefront distortion measurements versus total pump power is presented in Fig. 5.5. These results show, that thermal lens's focusing power differs up to 4 times in lasing and non-lasing conditions at highest pump power. In majority of laser crystals thermal lens tends to be stronger in non-lasing conditions, but among them the Yb:KGW crystal exhibits a different, and apparently opposite, behavior. Indeed, the thermal lens dioptric power is here higher under lasing action than under non-lasing conditions. It can be interpreted as illustrated in Fig. 5.6.

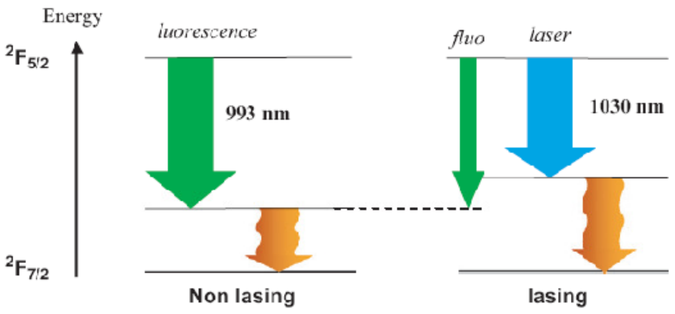

Fig. 5.6 Qualitative explanation of the paradoxical behaviour of the Yb: KGW crystal. Under non-lasing conditions (left), the thermal defect is low due to a low mean fluorescence wavelength (993 nm). When laser extraction at 1030nm becomes the dominant way down for excitation, then the quantum defect is higher [29].

The average fluorescence wavelength is particularly low in this material (993 nm). The quantum defect with laser oscillation at 1030 nm is thus higher than without oscillation [29]. Yb doped KGW absorption and fluorescence spectras are shown in Fig. 5.7.

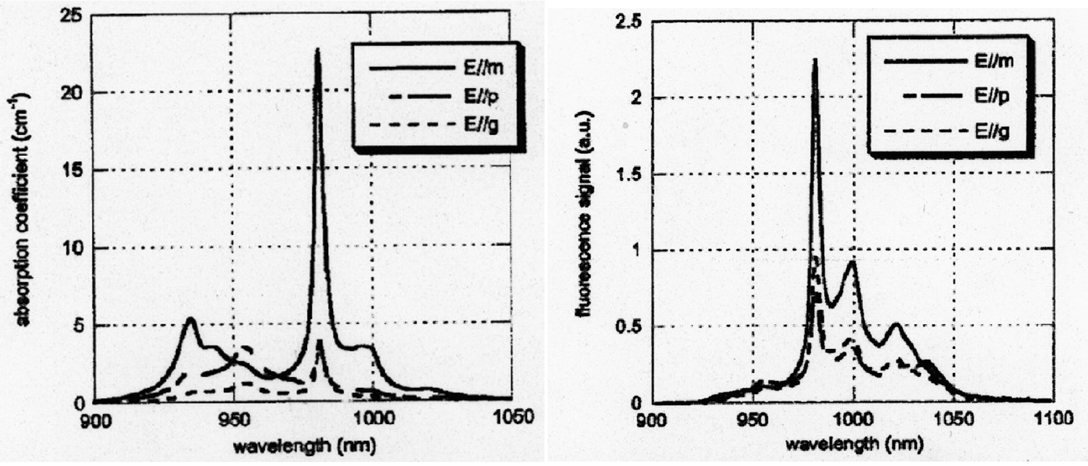

Fig. 5.7 Yb doped KGW absorption and fluorescence spectras [102].

Such thermal lens influence on laser performance corresponds well to published data of Yb:KGW thermal lens measurements [29]. In lasing conditions, as shown in Fig. 5.5, at low pump powers thermal lens is astigmatic - focusing power ratio between horizontal and vertical components is 1.4 (stronger in vertical direction). As pump power increases, focusing power ratio drops, eventually reaching 1 (symmetrical thermal lens) as pump power reaches maximum (94 W). In non-lasing conditions thermal lens remains astigmatic (stronger in vertical direction) even at highest available pump powers. Such thermal lens behavior can be explained assuming non-symmetrical cooling geometry of slab shaped active element and thermal properties of active element: thermal expansion coefficient for X_1' axis is ~2.6 times larger than X_2' axis which is orientated vertically [102].

Laser output beam profile was measured using CCD camera at the distance of 1 m from laser output mirror (see Fig. 5.8). The main criteria for cavity adjustment were symmetrical TEM_{00} output beam profile and output power. By adjusting cavity end mirrors and pump position it is possible to maintain symmetrical laser output up to ~80 W of pump power. Increasing of the pump power above 80 W results in gradual raise of distortions of beams profile and the beam cross-section transforms into the elliptical one. However, as seen in figure, distribution remains nearly Gaussian in traverse directions. At first, it might be surprising, that for symmetrical thermal lens laser output beam becomes non symmetrical. We attribute such behavior to non-symmetrical arrangement of pump (as shown in Fig. 5.3) that results in slightly asymmetric pump channel whose cross-section ellipticity increases towards crystal faces. When laser output power is low, spatial gain profile in Yb:KGW crystal is determined essentially by symmetric Gaussian mode of the cavity. As pump increases, absorption saturation in active element volume defined by cavity mode is eventually reached and larger pump portion absorbed in peripheral pump channel area leads to perturbation of symmetric gain profile.

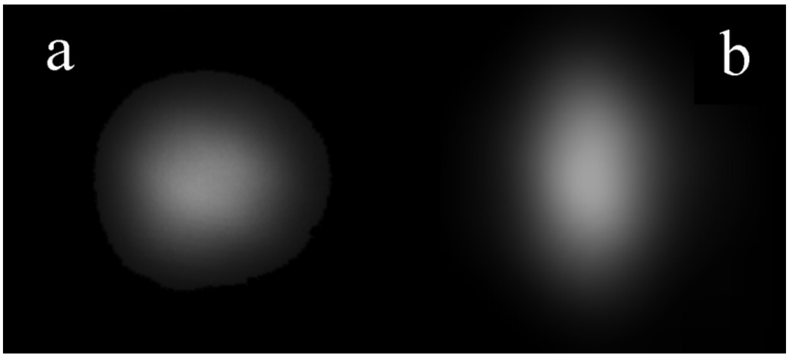

Fig. 5.8 Laser output beam profile at different values of laser output power when laser pump power is (a) 77W and (b) 86 W.

5.3 End bulging of active element under thermal load

Heat deposition in end-pumped lasers is very inhomogeneous. Much localized heat deposition leads to highly non-uniform and complex temperature and stress profiles. Besides the temperature and stress dependent variations of the refractive index, the contribution of active element end surface bulging to the formation of a thermal lens can be substantial in end-pumped lasers and was reported as high as ~35% for Nd:YAG [105] and up to ~50% for Nd:YLF [106] and Nd:YVO_4 [107]. Whereas, in Yb:KGW crystals end bulging measurements, to our knowledge, hasn’t been reported.

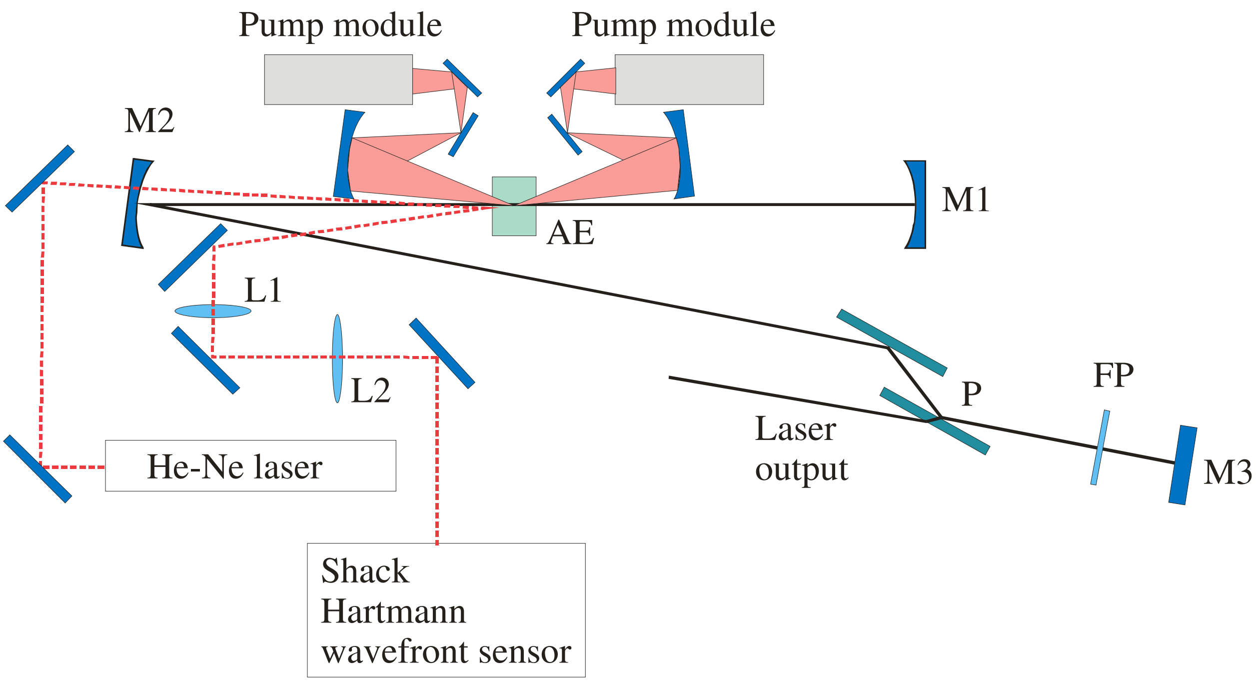

Fig. 5.9 Experimental setup for end-bulging measurements.

Experimental setup was modified measurements of end bulging (see Fig. 5.9). Probe beam was directed at active elements facet at small angle of incidence. Thermal lens was calculated from reflected probe beam wavefront distortions. In our case active element is pumped from both sides, therefore we consider that end bulging in both ends of crystal is equal. Measurements were performed with crystal cut for beam propagation along the N_g axis. Contribution of end bulging expressed as fraction of thermal lens is presented in Fig. 5.10. End bulging has more influence to thermal lens in horizontal than vertical direction. This contributes to thermal lens astigmatism (see Fig. 5.5). As seen in Fig. 5.10 in vertical direction end bulging contributes to total thermal lens by ~10% in wide range of pump powers (in both lasing and non-lasing conditions). In horizontal direction, end bulging contributes up to 50% of total thermal lens in non-lasing conditions and ~20% at high pump powers (in lasing conditions).

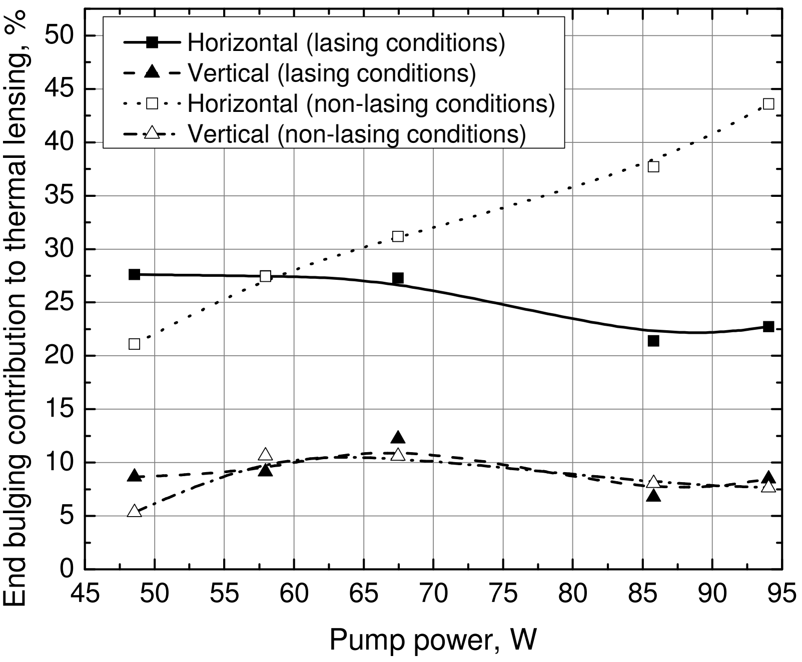

Fig. 5.10 Contribution of end bulging expressed as fraction of total thermal lens for vertical and horizontal directions in lasing and non-lasing conditions at different pump powers.

Crystal facet thermal deformations highly depend on pump setup. In our case, laser active element is pumped from by two pump modules, from opposite ends. Pump is slightly non-collinear in order to protect pump modules from damaging each other. This causes non-symmetrical (in lasing beams perspective) thermal distribution, which on its turn results in non-symmetrical thermal lens. Such thermal lens behavior can be explained assuming Yb:KGW thermal properties: in non-lasing conditions, most heating occurs in pump channel (where pump is absorbed), while in lasing conditions, heating occurs in cavity mode in active element volume (higher output power results in more pump absorbed in cavity mode volume, therefore more heating). Thermal lens component dependent on stress and dn/dT is stronger in vertical direction, meanwhile end bulging component is stronger in horizontal direction, due to pump geometry. By changing pump intersection angle it is possible to control astigmatism of total thermal lens. The impact of pump shaping to thermal lensing has been reported by F. Hoos et. Al. [11].

5.4 Thermal lensing in athermal Yb:KGW active element

Next step of experiments was examination of thermal lens in active element and laser operation when using Yb:KGW crystal cut along athermal direction. Crystal orientation and orientation of thermal expansion axes in relation to laser beam propagation is shown in Fig. 5.2 b. Thermal lens measurements were carried out at various pump powers for lasing and non-lasing conditions. Typical probe beam wavefront distortion after passing thermal lens in athermal cut active element at highest pump power (lasing conditions) is presented in Fig. 5.11.

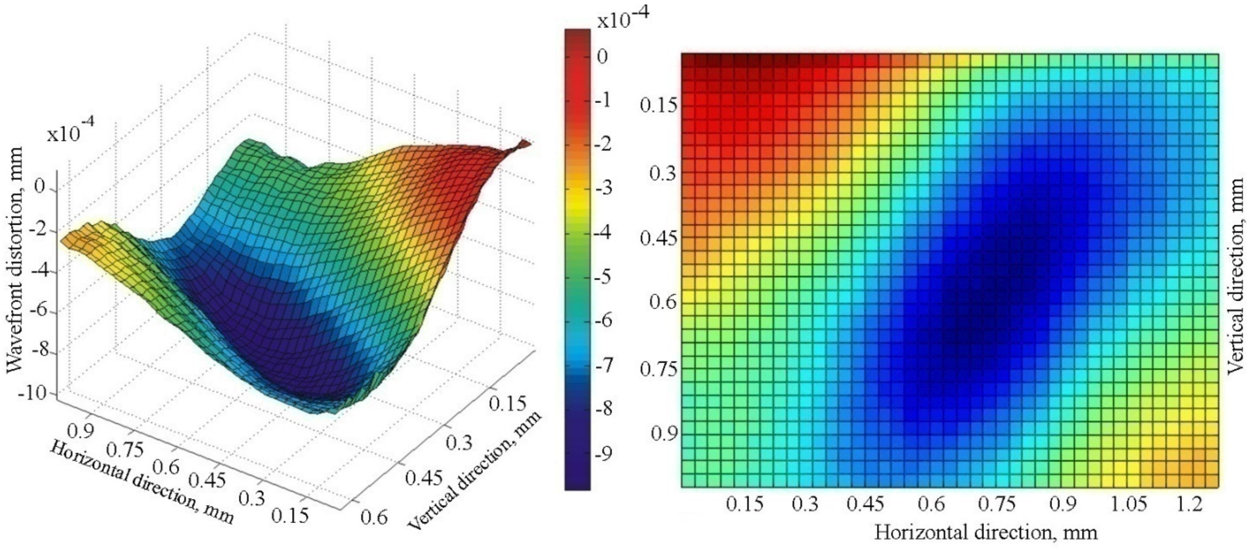

Fig. 5.11 Measured probe beam wavefront distortion after passing thermal lens in athermal orientation active element at 96W pump power (lasing conditions).

In contrast to the case of N_g-cut Yb:KGW wavefront distortions forms pattern which has elliptical shape and is tilted with reference of vertical direction by ~40º. , thermal lens in athermal active element is highly astigmatic. Major axis of ellipse is called slow axis, and minor axis – fast axes. We believe that such behavior is determined by highly anisotropic Yb:KGW properties. In case of uniform heating, this crystal might exhibit athermal behavior in particular directions, however, in our case active element is heated locally in comparatively small volume. Due to thermal gradients, thermal expansion of active element results in stress induced thermal lens. We found that fast axis of thermal lens is orientated closely to thermal expansion axis X_3'. Active element was flipped (along horizontal axis) in order to find out if such thermal lens behavior is resulted by active element physical properties or misalignment of pump. When active element was flipped over, the tilt of elliptical wavefront distortion pattern flipped as well forming mirror image of pattern shown in Fig. 5.11. This confirmed that non-symmetrical nature of thermal lens is caused by physical properties of active element. Similar thermal lens was observed for 3 different concentrations, same orientation active elements, with qualitative results. Variation of thermally induced lens maximum focusing power was calculated from data of wavefront distortion measurements and is presented in Fig. 5.12.

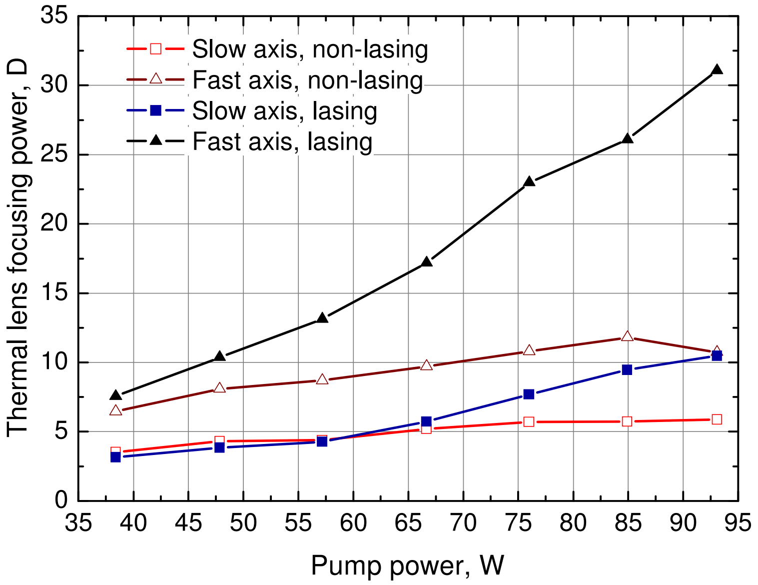

Fig. 5.12 Thermal lens focusing power in lasing and non-lasing conditions at different pump powers.

As shown in Fig.10. under lasing conditions thermal lens focusing power differs up to 3 times for fast and slow axis of thermal lens. Compared to N_g-cut active element performance (see Fig.5.) at highest available pump thermal lens in athermal cut active element is smaller by 30% for fast axis and 80% for slow axis.

Laser output beam profiles at different values of pump power are shown in Fig. 5.13. For pump powers above ~ 40 W laser output beam profile becomes elliptical, with major axis offset anticlockwise from vertical by nearly 40º. Such thermal lens behavior is resulted by orientation of thermal expansion axes (projection of X_3' thermal expansion axis is shown in Fig. 5.2 b).

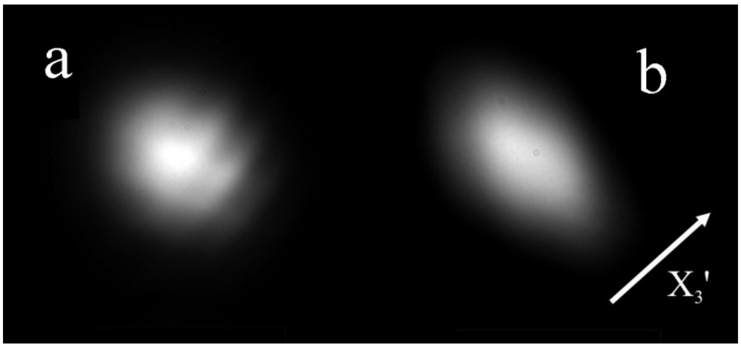

Fig. 5.13 Laser output beam profile at different values of laser output power when laser pump power is (a) 39W and (b) 86 W (with projection of X_3' thermal expansion axis).

Measured laser output power dependence on pump power in CW mode operation is shown in Fig. 5.14. Notably laser output power is 2 times smaller when using athermal cut Yb:KGW crystal compared to N_g cut active element.

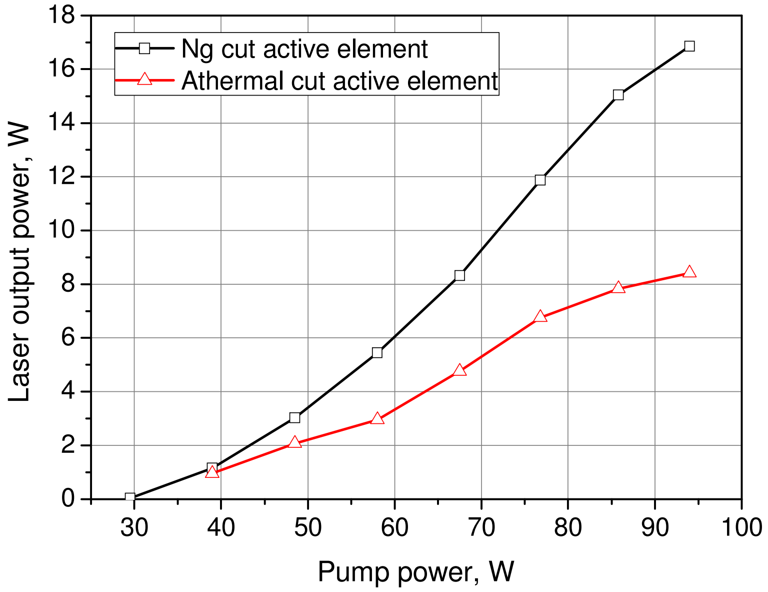

Fig. 5.14 Measured laser output power dependence on pump power in CW mode operation (for N_g cut and athermal cut active elements).

Thermal lens study by J. H. Hellstrom at el. [30] has shown that thermal lens is lower in athermal orientation active element than in crystal cut for propagation along N_p axis. Their study has shown, that laser with the athermal cut Yb:KGW (shown in Fig. 5.1a) always exhibited better beam quality for the same absorbed pump powers. As well, the beam for this crystal was to a large degree stigmatic, that is the M^2 values along orthogonal directions were very similar, in contrast to the N_p cut crystal, where higher-order modes were preferentially generated perpendicular to the strong thermal expansion axis (axis X_3') [30]. However, due to lower absorption and emission cross-sections of the athermal active element, laser output power was nearly two times lower for same pump power than in case of N_p cut crystal. Looking from perspective of thermal expansion axes, N_p cut active element looks similar to our investigated athermal orientation: thermal expansion axis X_3' projection to crystal face is orientated at angle to horizontal direction. This in both cases results in strongly astigmatic thermal lens and elliptical output beam profile, with mean axis orientated perpendicular to X_3'. Meanwhile in athermal orientation investigated by J. H. Hellstrom at el. [30] light propagates along strong thermal expansion axis X_3' similarly to N_g cut crystal case. Despite higher thermal lens focusing power, compared to athermal cut crystals, N_g

orientation offers higher absorption and emission cross-sections, allowing to achieve good spatial laser output characteristics at high average powers.

5.5 Summary

Experimental values of the focal length of thermal lenses in end-pumped N_g-cut Yb:KGW active element have been presented. The contribution of active element end bulging to total thermal lens focusing power has been examined as well. Athermal propagation direction of Yb:KGW proposed by Biswal et al. [102] following thermooptic studies has been tested under both lasing and non-lasing conditions.

A maximum output power of 8.5W for 94W of pump power was achieved with the athermal direction cut crystal. For comparison, the N_g-cut crystal generated almost 17W of output power for the same incident pump power. The thermal lens in both the N_g-cut and the athermal direction cut crystals is determined primarily by the anisotropic thermal expansion of the Yb:KGW. Thermal gradients due to pump beam geometry cause a thermal lens even in the athermal direction cut configuration. The tests confirmed that the thermal lens is lower than in conventional N_g-cut Yb:KGW. However, the laser beam for the investigated athermal cut is characterized by much higher astigmatism than for N_g-cut active element. Moreover, fast axis of thermal lens is offset by 40º from vertical, further complicating the use of such crystals. Considering higher efficiency and more symmetric thermal lens N_g-cut Yb:KGW is better suited for applications in high average power femtosecond laser systems than investigated athermal direction of propagation.

6 40 W dual active element Yb:KGW laser

In previous chapter we have discussed thermal lensing properties of different orientation Yb:KGW active elements. Further power scaling of such systems is limited by thermal lens in lasers active element. It is possible to reduce thermal loading, by increasing crystal volume associated with lasing. Increasing crystal length would be only partially beneficial due to non-collinear pump setup, while increasing its diameter, would require increasing thickness of active element, that is disadvantageous due to poor thermal conductivity of Yb:KGW active element. The promising method for average power scaling is the implementation of symmetric laser cavity with two active elements [108; 109; 109]. Such an approach allows decreasing thermal load for laser active medium and stabilizes the laser operation over broad range of pump power. In this chapter the results on development of high average power Yb:KGW regenerative amplifier based on dual active element architecture for femtosecond pulse amplification are presented.

6.1 Experimental set-up

The schematic diagram of regenerative amplifier that employs two slab shaped Yb:KGW active elements is presented in . The Yb:KGW crystals were cut for amplified pulse propagation along the *c* crystallographic direction. We have used slightly different active elements (AE1 length 5 mm, aperture 6x1,4 mm, doping rate 2% and AE2 length 6mm, aperture 6x1mm, doping rate 1,6%) each pumped by two 50W pump modules produced by Light Conversion ,Ltd., and ensuring pump intensity on the crystal up to 70 kW/cm^2. Resonator consists of flat mirrors V2, V5, V6 (reflectivity R=100%), V1 (R=98%) and spherical mirrors V3, V4 (radius r= -300 mm, R= 100%). Other components are f=150 mm lens (L), λ/4 phase plate FP1, λ/2 phase plate FP2, BBO Pockels cell PC and pair of the thin-film polarizers P. The polarization plane of pump radiation in all the cases was parallel to *a* crystallographic direction, while the plane of polarization of radiation oscillating in cavity was set by changing the angular orientation of phase plate FP2. Output coupling of cavity we varied by rotation of the phase plate FP1.

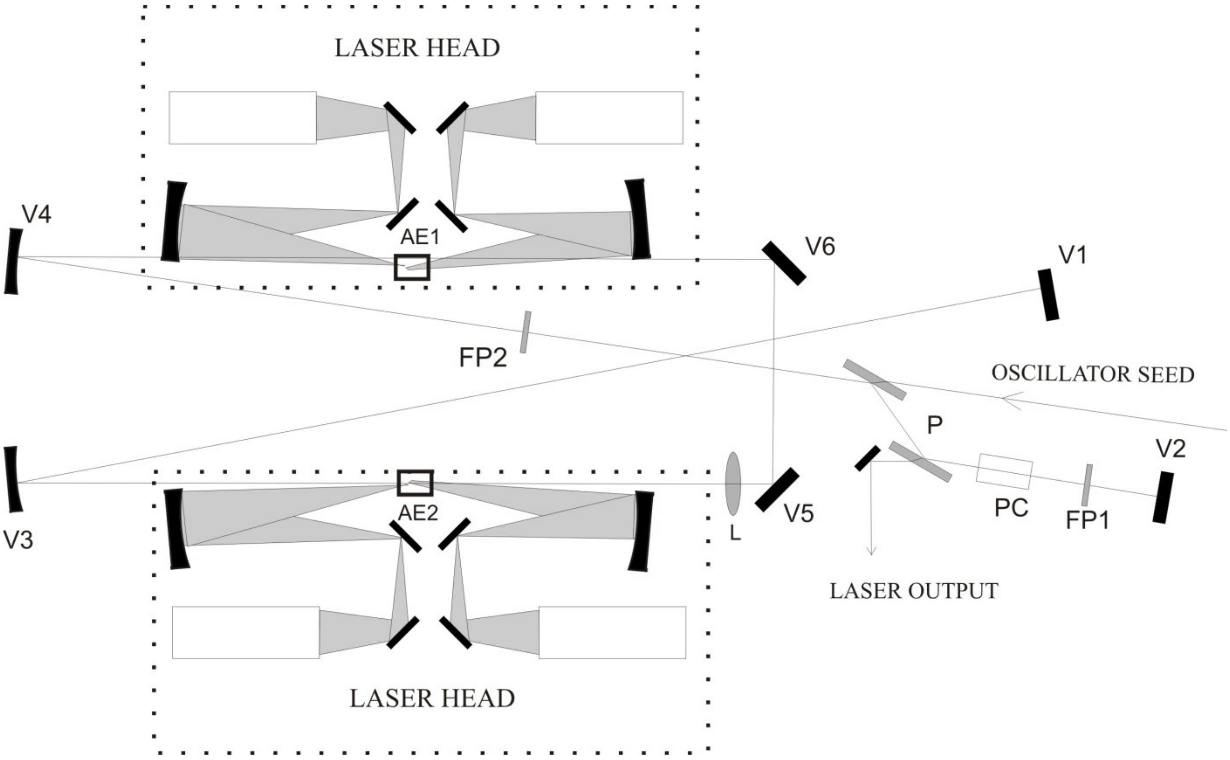

Fig. 6.1 Experimental setup.

6.2 CW operation

At the first stage of experiments we examined the simplified experimental scheme using single laser head with active element AE1. In this case the lens L was replaced by HR spherical mirror with r= 300 mm. Laser output characteristics for different polarizations were measured. When polarization of radiation oscillating in the cavity is set to be parallel to *b* crystallographic axis of Yb:KGW crystal , the ~26 W output power was reached. For perpendicular polarization (cavity supported polarization is parallel to *a* crystallographic axis) approximately 25 % lower output power was observed. The laser output power measurements were performed optimizing the transmission of the effective output coupling at the every value of pump power. The value of optimum transmission of the output coupler is rising along with increase of pump power and at maximum output power was evaluated as 22%. This value was calculated by comparing laser output power with reference to the power of radiation that was leaking through the mirror V1 (R=98%).

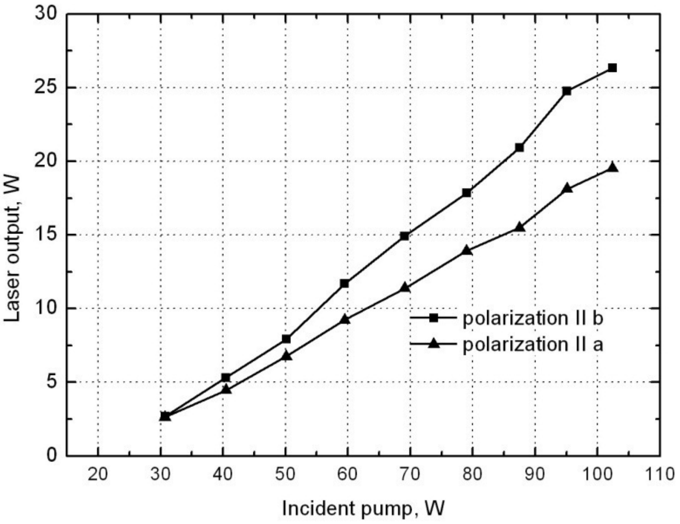

Fig. 6.2 Single active element laser output power versus incident pump power in CW mode.

While examining laser operation during startup both laser beam profile and output power experience dramatic changes. Laser output power changes in time were observed with oscilloscope instantly opening blocked laser cavity. Output power peek was observed, which gradually settles down. Ratio between settled down and peek values rise with increase of pump power. After startup, laser output power decrease exponentially to steady value.

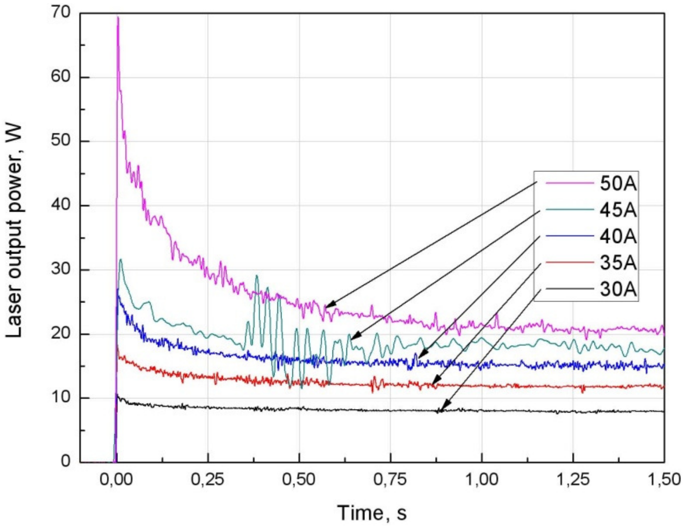

Fig. 6.3 Laser output power during startup. Zero in time scale corresponds to moment when cavity is unblocked.

Such laser behavior indicates considerable thermal lens influence. Initial thermal lens strength in active element is conditioned only by absorbed pump. In Yb:KGW case, pump absorption saturation is reached in several kW/cm^2 intensity range, thus most of pump passes crystal unabsorbed. As cavity is unblocked, and laser starts, population inversion decreases at a same time increases pump absorption. As well, the mean fluorescence wavelength (993 nm) is much lower than the laser wavelength (1030 nm). That means that a stimulated photon generates more heat than a spontaneous photon. This leads to larger thermal lens strength in lasing conditions. In current experimental setup, laser cavity is optimized for lower thermal lens strength, thus output power peek is observed at startup. Such thermal lens influence on laser performance corresponds well to published data of Yb:KGW thermal lens measurements [28]. As well at some certain pump powers rapid output power fluctuations were observed. We believe those fluctuations are associated with transient processes of laser mode shaping

We also have examined the dynamics of the output beam profile formation. The beam profiles registered with CCD camera at different time moments after laser startup that are shown in clearly show a significant beam profile alteration due to transitional thermal lens forming processes.

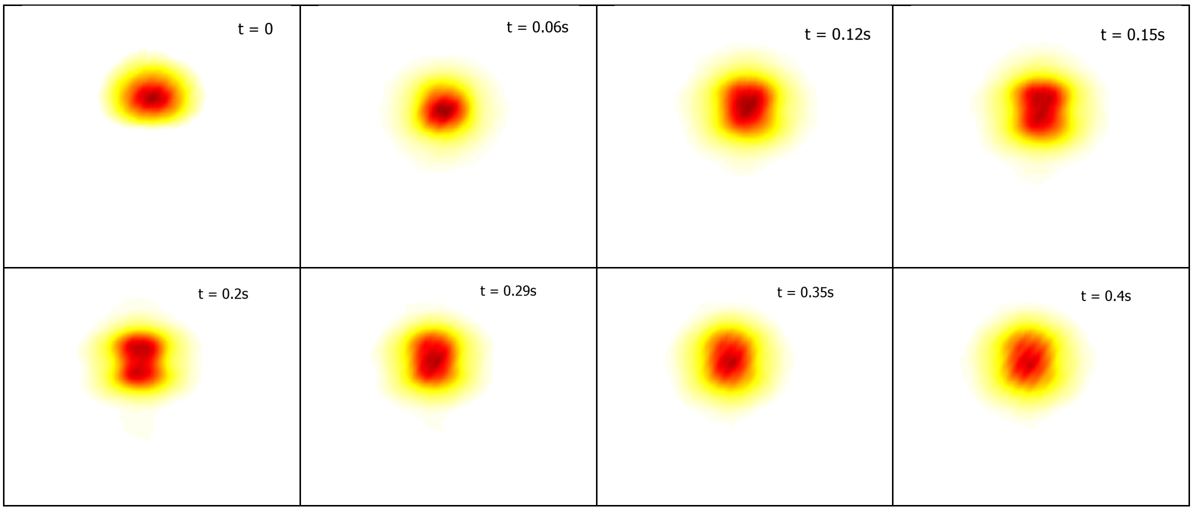

Fig. 6.4 Lazer output beam profile at different moments after laser startup. Zero corresponds to moment when cavity is unblocked.

Next step in our experiments was the examining of laser CW operation using full experimental set up, i.e. with both laser heads. As in previous experiments, laser output power versus pump was measured for different polarizations of radiation oscillating inside laser cavity and it was found out that output power was approximately 20-30% larger when polarization is set to be parallel to active elements *b* crystallographic axis (see). Maximum output power reached in CW mode was 44 W. Once again, optimum output mirror for each pump power value was measured, by optimizing output power with phase plate FP1. Optimum mirror dependency on laser output power is shown in . Comparison of these results and the ones obtained in single active element case it’s shows that due to increased gain the optimum mirror transmission value is approximately twice bigger, and reaches 50-60% at highest pump level.

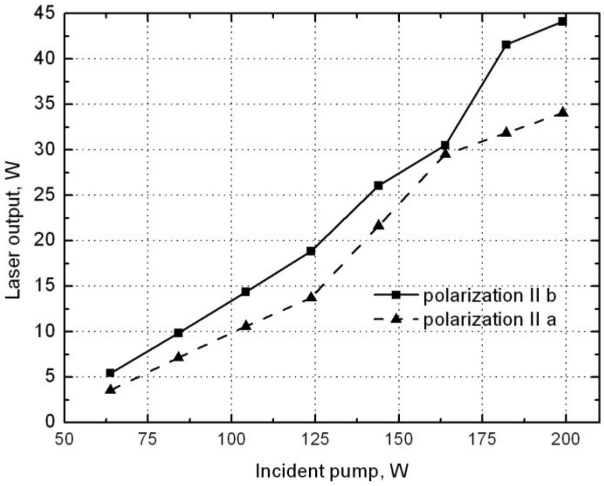

Fig. 6.5 Dual active element laser output power versus incident pump power.

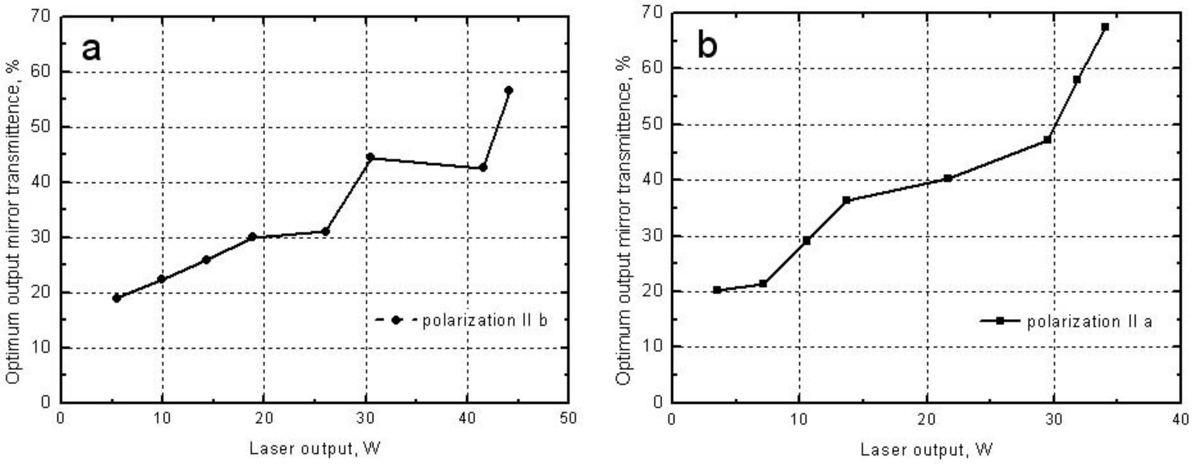

Fig. 6.6 a) Optimum output coupler transmittance versus output power: a) cavity supported polarization is parallel to *b* crystallographic axis, b)) cavity supported polarization is parallel to *a* crystallographic axis.

Laser output beam profiles at different values of laser output power that was measured using CCD camera at the distance of 2 m from laser output mirror are presented in . It was found that when increasing laser output up to ~15 W the laser output beams profile is symmetric and nearly Gaussian. We note that slight modulation of registered beam profiles is not a real beam characteristic and is caused by Fabry-Pero cavity effects in the camera. Increasing of the output power above 15 W results in gradually raising distortions of beams profile and the beam cross-section transforms into the slightly elliptical one. However, as seen in figure, distribution remains nearly

Gaussian in traverse directions. The far field laser output beam profiles measured in focus of f=100 mm lens are presented in Fig. 6.8. At low power far field intensity distribution is very close to Gaussian one. At high powers some background radiation around the central spot appears, however the energy content of this background is of order of only several percents. The measurements of beam quality parameter M^2 indicated that even at highest laser output powers the M^2 values are below 1.5.

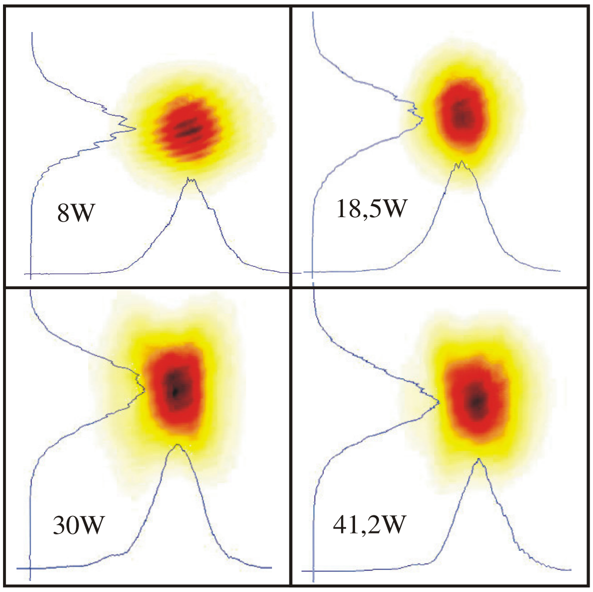

Fig. 6.7. Laser output beam profile at different values of laser output power.

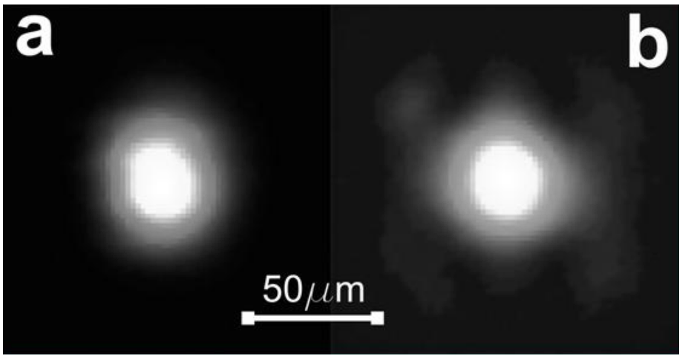

Fig. 6.8 Beam profile at focus of f=100mm lens when laser output power is (a) 9W and (b) 40 W.

The dual active element Yb:KGW laser was tested in operation regime of regenerative amplification mode, seeding it by femtosecond pulses from commercial diode pumped Yb:KGW oscillator of PHAROS laser system (Light Conversion, Ltd.). Output power of order of 30 W was reached at 200 W of incident pump. The ~5.4 nm FWHM spectrum of amplified pulses registered at maximum pump power. It is planed that this work will be continued optimizing spectral bandwidth of femtosecond pulse regenerative amplification and performing recompression of amplified pulses down to sub-300 fs pulses durations.

The spatial characteristics of amplified radiation were essentially the same as in the case of CW mode operation. We believe that 100 W of pump power is limit for current experimental conditions crystal mount and cooling setup.

6.3 Summary

In this chapter the potential of power scaling of Yb:KGW laser by implementation of dual active element cavity configuration was demonstrated. Maximum output power reached in CW mode was 44 W, witch to our knowledge is highest output power reported in Yb:KGW bulk lasers up to date. As output power increases, nearly symmetrical Gaussian profile beam becomes slightly elliptical, although remains Gaussian in traverse directions. The measured beam quality parameter M^2 is below 1,5 even at maximum output power.

Conclusions

1. Shack Hartmann wavefront sensor adapted for measurement of thermal lens in end pumped lasers has been constructed.
2. The static aberration compensator approach is well suited for high-power diode pumped lasers. This method has the advantages of greater simplicity and a wide applicability to laser designs. A diode-pumped Nd:YVO_4 laser with a 1.2 diffraction-limited output of 9.5 W using a thin film deposition technology made aberration compensator to correct the thermally induced phase distortion of the lasing medium has been demonstrated. Employment of proper thermal lens aberration compensator allows for laser threshold reducing and ensures improved output beam quality parameter M^2 in wide pump power range.
3. Prospects of output pulse energy scaling in diode end-pumped Yb:YAG laser with elliptical mode geometry was investigated. In Q-switch mode laser produced 8 ns pulses with average output power up to 5,5 W at pump power of 52 W, while in CW operation mode the 8 W output power was achieved. We have measured the focusing power of astigmatic thermal lens in laser active element and examined the quality of output beam at different output power. In spite of strongly astigmatic thermal lens due to optimized cavity design the output beam exhibit high spatial quality: beam quality parameter M^2 in both vertical and horizontal plane was close to unity. Such laser design offers good prospects for power scaling of diode pumped lasers.
4. Experimental values of the focal length of thermal lenses in end-pumped N_g-cut Yb:KGW active element have been presented. The contribution of active element end bulging to total thermal lens focusing power has been examined as well. Athermal propagation direction of Yb:KGW proposed by Biswal et al. [102] following

thermooptic studies has been tested under both lasing and non-lasing conditions. Considering higher efficiency and more symmetric thermal lens N_g-cut Yb:KGW is better suited for applications in high average power femtosecond laser systems than investigated athermal direction of propagation.

5. Thermal lens influence on laser dynamics has been investigated. Output power scaling of femtosecond Yb:KGW laser by implementation of dual active element cavity configuration were demonstrated. Moreover, highest output power reached in bulk Yb:KGW laser has been demonstrated, reaching 44W in CW mode.

Summary

In this thesis, analysis of thermal effects and various approaches for their mitigation in diode end pumped ultrafast lasers is presented. Experimental investigations were performed by employing Shack-Hartmann wavefront sensor which was adapted for measurements of thermal lens in diode end pumped lasers. During research, operation of high average power, diode-pumped, Nd:YVO_4 laser with aspheric aberration corrector was investigated. Actual thermal lens measurements were conducted in order to design properly shaped aberration corrector that was manufactured using a thin film deposition technology. This allows us to conclude that employment of proper thermal lens aberration compensator allowed for laser threshold reducing and ensured improved output beam quality parameter M^2 in wide pump power range. Prospects of output pulse energy scaling in diode end-pumped Yb:YAG laser by employing elliptical mode geometry was investigated. During our experiments, maximum average power in of ~ 5.5 W was obtained at repetition rates of 30-100 kHz, while in CW operation mode the 8 W output power was achieved. In spite of strongly astigmatic thermal lens due to optimized cavity design the output beam exhibits high spatial quality: beam quality parameter M^2 in both vertical and horizontal plane was close to unity. Detailed comparative study of thermal effects in Yb doped KGW crystals with different orientation was performed. Measurements confirm, that anisotropic optical and thermal properties of Yb:KGW along with asymmetric cooling and pumping conditions for longitudinally pumped thin slab shaped active elements leads to formations highly asymmetric thermal lens. By varying parameters, such as crystal orientation, cooling geometry and pump channel shaping we can significantly reduce negative impact of thermal effects on laser characteristics. We have also shown, that end bulging contributes up to 50% to thermal lensing in end pumped Yb:KGW lasers. Moreover, we have

investigated potential of laser output power scaling by implementation of symmetric cavity with two Yb:KGW active elements.

Refferences

[1] Byer, R. L., "Diode laser-pumped solid-state lasers." Science, 1988, Vol. 239, p. 742.

[2] Hanna, D. C. and Clarcson, W. A., "A review of diode-pumped lasers." New York : s.n., 1999. Advances in Lasers and Applications. pp. 1-18.

[3] Jeong, Y., et al., "“Power scaling of single-frequency ytterbium-doped fiber master oscillator power amplifier sources up to 500W." IEEE Journal of Selected Topics in Quantum Electronics , 2007, Issue 3, Vol. 13, pp. 546-551.

[4] Shah, L., et al., "High energy femtosecond Yb cubicon fiber amplifier." Optics Express, 2005, Vol. 13, pp. 4717-4722.

[5] Giesen, A. and Speiser, J., "Fifteen Years of Work on Thin-Disk Lasers: Results and Scaling Laws." IEEE J. Select Topics Quantum Electronics, 2007, Vol. 13, pp. 598 – 609.

[6] Stewen, C., et al., "A 1-kW CW thin disc laser." IEEE Journal of Selected Topics in Quantum Electronics, 2000, Issue 4, Vol. 6, pp. 650- 657.

[7] Innerhofer, E., et al., "60-W average power in 810-fs pulses from a thin-disk Yb:YAG laser." Optics Letters, 2003, Issue 5, Vol. 28, pp. 367-369 .

[8] Brunner, F., et al., "Powerful red-green-blue laser source pumped with a mode-locked thin disk laser." Optics Letters, 2004, Issue 16, Vol. 29, pp. 1921-1923.

[9] Neuhaus, J., et al., "Subpicosecond thin-disk laser oscillator with pulse energies of up to 25.9 microjoules by use of an active multipass geometry." Opt. Express, 2008, Vol. 16, pp. 20530-20539.

[10] Hellstrom, J.H., et al., "Efficient Yb;KGW laser end-pumped by high power diode bars." Applied Physics B, 2006, Vol. 83, pp. 235-239.

[11] Hoos, F., et al., "Thermal lensing in an end-pumped Yb:KGW slab laser with high power single emitter diodes." Optics Express, 2008, Issue 9, Vol. 16, pp. 6041-6049.

[12] Koechner, W., *Solid-state laser engineering.* [ed.] 5th. Heidelberg :

Springer-Verlag, 1999.

[13] Rockwell, D. A., "A review of phase-conjugate solid-state lasers." IEEE J. Quantum Electronics, 1988, Vol. 24, pp. 1124–1140.

[14] Ojima, Y., Nawata, K. and Omatsu, T., "Over 10-watt pico-second diffraction-limited output from a Nd:YVO4 slab amplifier with a phase conjugate mirror." Optics Express, 2005, Vol. 13, pp. 8993-8998.

[15] Wyss, E., et al., "Thermooptical Compensation Methods for High-Power Lasers." IEEE journal of Quantum Electronics, 2002, Issue 12, Vol. 38, pp. 1620-1628.

[16] Reinert, F. and Lüthy, W., "13. , "Thermo-optically driven adaptive mirror based on thermal expansion: preparation and resolution." Optics Express, 2005, Vol. 13, pp. 10749-10753.

[17] Reinert, F., et al., "Laser Resonator with a Thermo-Optically Driven Adaptive Mirror." 2005. Advanced Solid-State Photonics.

[18] Kasinski, J. J. and Burnham, R. L., "Near-diffraction-limited, high-energy, high-power, diode-pumped laser using thermal aberration correction with aspheric diamond-turned optics." Applied Optics, 1996, Vol. 35, pp. 5949-5954.

[19] Chen, B., et al., "Thermal Lensing of Edge-pumped Slab Lasers-I ." Applied Physics B: Lasers and Optics, 2006, Issue 3, Vol. 82, pp. 413-418.

[20] Yan, X., et al., "Numerical modeling of the thermal lensing effect in a grazing-incidence laser." Optics Communications, 2009, Issue 1, Vol. 9, pp. 1851-1857 .

[21] Lausten, R. and Balling, P., "Thermal lensing in pulsed laser amplifiers: an analytical model." J. Opt. Soc. Am. B, 2003, Issue 7, Vol. 20, pp. 1479-1485.

[22] Yu, J., Meng, H. and Jin, T., "Modeling of thermal lensing in cw end-pumped solid state lasers." 1996. Proceedings of SPIE. Vol. 2889, pp. 171-177.

[23] Lucca, A., et al., "High power diode-pumped CW laser operation of Yb:CaF2." 2004. CPD-A1 CLEO.

[24] Eichler, H. J., et al., "Thermal lensing and depolarization in a highly

pumped Nd:YAG laser amplifier." J. Phys. D: Appl. Phys., 1993, Vol. 26, pp. 1884-1891.

[25] Shao-yun, Hu, et al., "Experimental study of thermal lensing of Nd: YAG laser." Optoelectronics Letters, 2006, Issue 4, Vol. 2, pp. 278-281.

[26] Khizhnyak, A., Galich, G. and Lopiitchouk, M., "Characteristics of thermal lens induced in active rod of cw Nd:YAG laser." Semiconductor Physics, Quantum Electronics & Optoelectronics, 1999, Issue 1, Vol. 2, pp. 147-152.

[27] Koechner, W., "Thermal lensing in a Nd:YAG laser rod." Applied Optics, 1970, Vol. 9, pp. 2548-2553.

[28] Chenais, S., et al., "Thermal lensing measurments in diode-pumped Yb-doped GdCOB, YCOB, YSO, YAG and KGW." Optical materials, 2003, Vol. 22, pp. 129-137.

[29] Chenais, S., et al., "Thermal Lensing in Diode-Pumped Ytterbium Lasers—Part II: Evaluation of Quantum Efficiencies and Thermo-Optic Coefficients." IEEE Journal of Quantum Electronics, 2004, Issue 9, Vol. 40, pp. 1235-1242.

[30] Hellstrom, J.H., Bjurshagen, S. and Pasiskevicius, V., "Laser performance and thermal lensing in high-power diode-pumped Yb;KGW with athermal orientation." Applied Physics B, 2006, Vol. 83, pp. 55-59.

[31] Koechner, W., "Absorbed pump power, thermal profile and stresses in a cw pumped Nd: YAG Crystal." Applied Optics, 1970, Issue 6, Vol. 9, pp. 1429–1434.

[32] Timoshenko, S. and Goodier, J.N., *Theory of Elasticity.* 3rd. Singapore : McGraw-Hill, 1982.

[33] Born, M. and Wolf, E., *Principles of Optics.* 7. New York : s.n., 2002.

[34] Nye, J.F., *Physical Properties of Crystals.* Oxford : Clarendon Press, 1985.

[35] Auge, F., et al., "Theoretical and experimental investigations of a diode-pumped quasi-three-level laser: the Yb3+-doped Ca4GdO(BO3)3 (Yb:GdCOB) laser." IEEE Journal of Quantum Electronics, 2000, Issue 5, Vol. 36, pp. 598–606.

[36] Aron, A., et al., "Spectroscopic properties and laser performances of Yb:YCOB and potential of the Yb:LaCOB material." Optical Materials, 2001,

Vol. 16, pp. 181–188.

[37] Gaume, R., et al., "Spectroscopic properties and laser performance of Yb3+: Y2SiO5, a new infrared laser material." OSA TOPS Advanced Solid-State Lasers 34 (2000) 469, 2000, Vol. 34, p. 469.

[38] Nye, F. J., *Physical Properties of Crystals: Their Representation by Tensors and Matrices.* New York : Oxford University Press, 2000.

[39] Foster, J. D. and Osterink, L. M., "Thermal Effects in a Nd:YAG Laser." Applied Physics, 1970, Vol. 41, p. 3656.

[40] Koechner, W. and Rice, D., "Effect of birefringence on the performance of linearly polarized YAG:Nd lasers." IEEE Journal of Quantum Electronics, 1970, Issue 9, Vol. 6, pp. 557 - 566 .

[41] Frauchiger, J., Albers, P. and Weber, H.P., "Modeling of thermal lensing and higher order ring mode oscillationin end-pumped C-W Nd:YAG lasers." IEEE Journal of Quantum Electronics, 1992, Issue 4, Vol. 28, pp. 1046-1056.

[42] Brignon, A., et al., "Spatial beam cleanup of a Nd: YAG laser operating at 1064 nm with two-wave mixing in Rh:BaTiO3." Applied Optics, Vol. 36, pp. 7788–7793.

[43] Xie, W., et al., "Diffraction losses of high power solid state lasers." Optics Communications, 2001, Vol. 189, pp. 337–343.

[44] Frauchiger, J., Albers, P. and Weber, H., "Modeling of thermal lensing and higher order ring mode oscillation in end-pumped CW Nd: YAG lasers." IEEE Journal of Quantum Electronics, 1992, Issue 4, Vol. 28, pp. 1046–1056.

[45] Druon, F., et al., "Wave-front correction of femtosecond terawatt lasers using deformable mirrors." Optics Letters, 1998, Issue 1, Vol. 23, pp. 1043–1045.

[46] Clarkson, W.A., "Thermal effects and their mitigation in end-pumped solid-state lasers." Journal of Physics D: Applied Physics, 2001, Vol. 34, pp. 2381–2395.

[47] Chenais, S., et al., "On thermal effects in solid state lasers: the case of ytterbium-doped materials." Progress in quantum electronics , 2006, Vol. 30, pp. 89-153.

[48] Gordon, J., et al., "Long-transient effects in lasers with inserted liquid samples." Journal of Applied Physics, 1965, Issue 1, Vol. 36, pp. 3–8.

[49] Fournier, D., et al., "Sensitive in situ trace-gas detection by photothermal deflection." Applied Physics Letters, 1980, Issue 6, Vol. 37, pp. 519–521.

[50] Burnham, D., "Simple measurement of thermal lensing effects in laser rods." Applied Optics, 1970, Issue 7, Vol. 9, pp. 1727–1728.

[51] Paugstadt, R. and Bas, M., "Method for temporally and spatially resolved thermal-lensing measurements." Applied Optics, 1994, Issue 6, Vol. 33, pp. 954–959.

[52] Misra, R. and Banerjee, P., "Theoretical and experimental studies of pump-induced probe deflection in a thermal medium." Applied Optics, 1995, Issue 18, Vol. 34, pp. 3358–3365.

[53] Neuenschwander, B., Weber, R. and Weber, H., "Determination of the thermal lens in solid-state lasers with stable cavities." IEEE Journal of Quantum Electronics, 1995, Issue 6, Vol. 31, pp. 1082–1087.

[54] Kogelnik, H. and Li, T., "Laser beams and resonators." Applied Optics, 1966, Vol. 5, p. 1550.

[55] Cabezas, A., Komai, L. and Treat, R., "Dynamic measurements of phase shifts in laser amplifiers." Applied Optics, 1966, Issue 4, Vol. 5, pp. 647–651.

[56] Welling, H. and Bickart, C., "Spatial and temporal variation of the optical path length in flash-pumped laser rods." Journal of the Optical Society of America, 1966, Issue 5, Vol. 56, pp. 611–618.

[57] Pfistner, C., et al., "Thermal beam distortions in end-pumped Nd: YAG, Nd: GSGG, and Nd: YLF Rods." IEEE Journal of Quantum Electronics, 1994, Issue 7, Vol. 30, pp. 1605–1615.

[58] Khizhnyak, A., Galich, G. and Lopiitchouk, M., "Characteristics of thermal lens induced in active rod of cw Nd: YAG laser." Semiconductor Physics, Quantum Electronics and Optoelectronics, 1999, Issue 1, Vol. 2, pp. 147–152.

[59] Blows, J., Dawes, J. and Omatsu, T., "Thermal lensing measurements in line-focus end-pumped neodymium yttrium aluminium garnet using holographic lateral shearing interferometry." Journal of Applied Physics,

1998, Issue 6, Vol. 83, pp. 2901–2906.

[60] Blows, J.L., et al., "Thermal lensing measurements and thermal conductivity of Yb: YAB." Applied Physics B, 2003, Vol. 76, pp. 289–292.

[61] Primot, J., "Three-wave lateral shearing interferometer." Applied Optics, 1993, Issue 31, Vol. 32, pp. 6242–6249.

[62] Chanteloup, J.C., "Multiple-wave lateral shearing interferometry for wave-front sensing." Optics Letters, 1998, Vol. 23, pp. 621–623.

[63] Chanteloup, J.C., et al., "Single-shot wave-front measurements of high-intensity ultrashort laser pulses with a three-wave interferometer." Applied Optics, 2005, Issue 9, Vol. 44, pp. 1559–1571.

[64] Blows, J.L., et al., "Thermal lensing measurements and thermal conductivity of Yb: YAB." Applied Physics B, 2003, Vol. 76, pp. 289–292.

[65] Hartmann, J., "Bemerkungen uber den Bau und die Justirung von Spectrographen." Zeitung Instrumentenkd, 1900, Vol. 20, p. 47.

[66] Grossard, L., et al., "Iterative reconstruction of thermally induced phase distortion in a Nd:YVO laser." Journal of Optics A: Pure and Applied Optics, 2002, Vol. 4, pp. 1-7.

[67] Southwell, W.H., "Wavefront estimation from wavefront slope measurements." OSA, 1980, Vol. 70, pp. 998-1005.

[68] Karnakis, D.M., et al., "Surface integrity optimisation in ps-laser milling of advanced engineering materials ." Munich : s.n., 2007. Proc. 4th International WLT Conference on Lasers in Manufacturing.

[69] Moorhouse, C., "Industrial applications of a fiber-based high-average-power picosecond laser." 2009. Proc. SPIE. Vol. 72010F.

[70] , *http://www.ekspla.com/repository/catalogue/infofiles/IL/application_notes/M1104%20short%20pulse%20lasers%20for%20microfabrication.pdf.*

[71] Kraus, M., et al., "Microdrilling in steel with frequency-doubled ultrashort pulsed laser radiation." Viena : s.n., 2007. Proc. the 8th Int. Symp. on Laser Precision Microfabrication.

[72] Haas, S., Gordijn, A. and Stiebig, H., "High speed laser processing for monolithical series connection of silicon thin-film modules." Progress in Photovoltaics: Research and Applications, 2008, Vol. 16, pp. 195-203.

[73] Tucker, A. W., et al., "Stimulated-emission cross section at 1064 and 1342 nm in Nd:YVO4." Applied Physics, 1977, Vol. 48, pp. 4907-4911.

[74] Shen, D., et al., "Efficient Operation of an Intracavity-Doubled Nd:YVO4 KTP Laser End Pumped by a High-Brightness Laser Diode." Applied Optics, 1998, Vol. 37, pp. 7785-7788.

[75] Liua, C., et al., "Influence of spherical aberrations on the performance of dynamically stable resonators." Optics Communications, 2008, Vol. 281, pp. 5222–5228.

[76] Lubeigt, W., Valentine, G. and Burns, D., "Enhancement of laser performance using an intracavity deformable membrane mirror." Optics Express, 2008, Vol. 16, pp. 10943-10955.

[77] , *EKSPLA, www.ekspla.com.*

[78] Cuche, E., Marquet, P. and Depeursinge, C., "Simultaneous amplitude-contrast and quantitative phase-contrast microscopy by numerical reconstruction of Fresnel off-axis holograms." Applied Optics, 1999, Issue 34, Vol. 38, pp. 6994–7001.

[79] Cuche, E., Marquet, P. and Depeursinge, C., "Spatial Filtering for Zero-Order and Twin-Image Elimination in Digital Off-Axis Holography." Applied Optics, 2000, Issue 23, Vol. 39, pp. 4070–4075.

[80] Cuche, E., Bevilacqua, F. and Depeursinge, C., "Digital holography for quantitative phase-contrast imaging." Optics Letters, 1999, Issue 5, Vol. 24, pp. 291–293.

[81] Li, Chen, et al., "Q-switched operation of end-pumped Yb:YAG lasers with non-uniform temperature distribution." Optics Communications, 2003, Vol. 231, pp. 331-341.

[82] Ripin, D. J., et al., "300-W Cryogenically Cooled Yb:YAG Laser." IEEE J. Quantum Electronics, 2005, Vol. 41, pp. 1274-1277.

[83] Brown, D.C., "Nonlinear thermal and stress effects and scaling behavior

of YAG slab amplifiers." IEEE J. Quantum Electronics, 1998, Vol. 34, pp. 2393 – 2402.

[84] Eggleston, J. M., et al., "The Slab Geometry Laser – Part I: Theory." IEEE J. Quantum Electronics, 1984, Vol. 20, pp. 289-301.

[85] Aus de Au, J., et al., "High-power diode-pumped passively mode-locked Yb:YAG lasers." Optics Letters, 1999, Vol. 24, pp. 1281-1283.

[86] Paschotta, R., et al., "Diode-pumped passively mode-locked lasers with high average power." Applied Physics B, 2000, Vol. 70, pp. S25-S31.

[87] Paschotta, R., Aus der Au, J. and Keller, U., "Thermal Effects in High-Power End-Pumped Lasers with Elliptical-Mode Geometry." IEEE J. Select Topics Quantum Electronics, 2000, Vol. 6, pp. 636-642.

[88] Siegman, A. E., *Lasers.* s.l. : University science books, 1986.

[89] Doring, J., et al., "Period doubling and deterministic chaos in continuously pumped regenerative amplifiers." Optics Express, 2004, Vol. 12, pp. 1759-1768.

[90] Krupke, W.F., "Ytterbium solid-state lasers—the first decade." IEEE J. Sel. Top. Quantum Electronics, 2000, Issue 6, Vol. 6, pp. 1287–1296.

[91] Holtom, G.R., "Mode-locked Yb:KGW laser longitudinally pumped by poliarization-couples diode bars." Optic Letters, 2006, Vol. 31, pp. 2719-2721.

[92] Viana, B., et al., "Yb3+ doped laser materials for high power or ultrafast applications." 2004. Solid State Lasers and Amplifiers, Proc. of SPIE. Vol. 5460, pp. 146-155.

[93] Balembois, F., et al., "Yb-doped solid-state laser materials for high power and femtoseconds lasers." 2004. EPS-QEOD Europhoton Conference, Solit-state and Fiber Coherent Light Sources.

[94] Röser, F., et al., "131 W 220 fs fiber laser system." Optic Letters, 2005, Vol. 30, pp. 2754-2756.

[95] Buckley, J. R., et al., "Femtosecond fiber lasers with pulse energies above 10 nJ." Optic Letters, 2005, Issue 14, Vol. 30, pp. 1888-1890.

[96] , *http://www.cmxr.com/scientific/impulse.htm.*

[97] *http://www.amplitude-systemes.com/produitv.php?mode=performances&id_rub=179&id_prod_selec=1.*

[98] Buenting, U., et al., "Regenerative thin disk amplifier with combined gain spectra producing 500 µJ sub 200 fs pulses." Opt. Express, 2009, Vol. 17, pp. 8046-8050.

[99] Brunner, F., et al., "240-fs pulses with 22-W average power from a mode-locked thin-disk Yb:KY(WO4)2 laser." Optic Letters, 2002, Vol. 27, pp. 1162-1164.

[100] , *http://www.lightcon.com/index.php?id=29,0,0,1,0,0.*

[101] *http://www.highqlaser.at/en/products/regenerative-amplifiers/femtoregen-series.*

[102] Biswal, S., O'Connor, S. P. and Bowman, S. R., "Thermo-optical parameters measured in ytterbium-doped potassium gadolinium tungstate." Applied Optics, 2005, Vol. 44, pp. 3093-3097.

[103] Filippov, V., Kuleshov, N. V. and Bodnar, L. T., "Negative thermo-optical coefficients and athermal directions in monoclinic KGd(WO4)2 and KY(WO4)2 laser host crystals in the visible region." Applied Physics B, 2007, Issue 4, Vol. 87, pp. 611-614.

[104] Pujol, M. C., et al., "Structure, crystal growth and physical anisotropy of KYb(WO4)2, a new laser matrix." J. Appl. Cryst., 2002, Vol. 35, pp. 108-112.

[105] Weber, R., et al., "Cooling schemes for longitudinally diode-laser pumped Nd:YAG rods." IEEE Journal of Quantum Electronics, 1998, Vol. 34, pp. 1046–1053.

[106] Baer, T., Nighan, W. and Keierstead, M., "Modeling of end-pumped, solid-state lasers." 1993. Conference on Lasers and Electro-optics: OSA Technical Digest Series. Vol. 11, p. 638.

[107] Kleine, K., et al., "High brightness Nd: YVO4 laser for nonlinear optics." 1999. Advanced Solid State Lasers, OSA Trends in Optics and Photonics Series. Vol. 26, pp. 157–158.

[108] Yang, J.Z.H. and Walker, B.C., "0.09-terawatt pulses with a 31%

efficient, kilohertz repetition-rate Ti:sapphire regenerative amplifier." Optic Letters, 2001, Vol. 26, pp. 453-455.

[109] Honea, E.C., et al., "High-power dual-rod Yb:YAG laser." Optic Letters, 2000, Vol. 25, pp. 805-807.

[110] , *Red Optronics.* [Online] http://www.redoptronics.com/Nd-YVO4-crystal.html.

[111] *CryLight.* [Online] http://www.crylight.com/Laser_Crystals/Nd-YVO4-Crystal_1.html.